Many-Body Decoherence with Cold Atoms in Optical Lattices

Saubhik Sarkar

Department of Physics and SUPA
UNIVERSITY OF STRATHCLYDE

A thesis submitted in partial fulfilment
of the requirements for the degree of
Doctor of Philosophy

2017

This thesis is the result of the author's original research. It has been composed by the author and has not been previously submitted for examination which has led to the award of a degree.

Signed:

Date:

Abstract

Ultracold atoms in optical lattices have proven to be an ideal testbed for simulating strongly correlated condensed matter physics. The microscopic understanding of the underlying Hamiltonian and precise control over the Hamiltonian parameters via external fields allow faithful realisation of interesting many-body systems that are otherwise hard to study theoretically or experimentally.

This thesis addresses the issue of many-body decoherence, using analytical and numerical techniques, in these optical lattice experiments that arises due to coupling to the environment. We specifically study fermionic systems to investigate the effects of incoherent light scattering on the dynamics. Starting from the atomic structure of fermionic species that are experimentally relevant we provide a framework to derive a microscopic master equation and look at the regimes of strong interactions. The interplay between the atomic physics and many-body physics is found to give rise to interesting observations like suppression of the decoherence effect for magnetically ordered insulators that occur for strong repulsive interactions and an enhancement of the decoherence effect for the case of superfluid pairs that occur for strong attractive interactions. The master equation framework is then applied to a recent experiment looking at the effect of controlled decoherence on a many-body localised system of ultracold fermions in an optical lattice. We determine the dissipative processes in the system looking at the atomic structure of the fermionic species.

Lastly we study a system of two species bosons to investigate the effect of interspecies interaction in terms of bipartite entanglement between the species, and how this impacts upon the visibility of the momentum distribution. This study proposes a solution to a recent experimental observation of effects on the momentum distribution of impurity atoms in a Bose-Einstein condensate that would not be explained by polaronic behaviour alone.

Acknowledgements

I would like to thank my family and my friends across the three continents who have made my journey through the PhD lifecycle memorable and sometimes, bearable. I would especially like to thank my colleagues in Strathclyde, including Anton, Guanglei, Aracelli and Jorge for all their helps and friendship. Then there are two people who have been absolutely invaluable to me. I cannot thank enough my supervisor, Andrew Daley, for his patience and empathy and for frequently going out of his way to make sure that I stay on course. He has been a guide to me in the truest sense of the word. Lastly I would like to express my gratitude towards my wife, Suparna. I don't know how to thank her for the understanding, support and love she has showered me with and the unimaginable sacrifices she has made for me. I dedicate this thesis to you.

Contents

Chapter 1

Introduction

1.1 Background and overview

For many of the quantum systems we are interested in, it is often possible to deduce a microscopic model and write down the Schrödinger equation that would describe the system. Unfortunately that ability alone usually does not allow us to extract most of the interesting properties about these systems as only a minute fraction of them are analytically solvable. Therefore, in most of the cases, one has to look for numerical solutions. Even there, exact numerical solutions usually exist only for very small system sizes as the size of the Hilbert space generally grows very quickly with the system size. To have a clearer idea about this, one can think of a spin-chain of length M with spin-half particles. The size of the Hilbert space here is 2^M and to store a general quantum state on a classical computer with double precision numbers the memory needed is 2^{M+4} bytes. For a modest-sized chain of 100 spins this number is already huge, approximately 10^{16} PB, and beyond the capacity of any classical hardware in the foreseeable future. Therefore, it is not possible to carry out simulations of such systems on classical computers as we run out of space very quickly, to store the states and perform operations on them, as the system size grows beyond a few particles.

To study the most interesting many-body systems in the strongly interacting regime, often it is sufficient to replace the exact Hamiltonian with a simpler effective Hamiltonian that takes into account the necessary physical properties to capture the essential features. A relevant example of this, in the context of this thesis, can be found in the (Fermi) Hubbard model. This model was devised to understand the system of strongly correlated electrons moving in a periodic lattice [1]. The essential physics is described by only two parameters, the tunnelling rate J and the interaction energy U. Along with a successful explanation of the Mott insulator-metal transitions in these systems the Hubbard model is considered to be a widely accepted model for various strongly interacting systems, including being a strong candidate to capture the basic physics of the high-T_c superconductors in cuprates [2, 3]. Despite the simplicity of the model, the exact solution in more than one dimension is still intractable [4]. Numerical techniques also fail to exactly simulate the model for reasons stated earlier. In this case a modest 40 site lattice with 20 spin-up and 20 spin-down fermions has a very large Hilbert space dimension of approximately 2×10^{22}.

An alternative method is to work with well-controlled quantum systems that simulate the Hamiltonian in question. This is the idea of the *quantum simulator*, first discussed by Feynman [5]. We specifically refer here to so-called analogue quantum simulators which are systems that obey the same Hamiltonian as our original systems of interest but are a lot easier to be controlled, manipulated and probed [6]. This is where the experimental toolbox with ultracold atoms in optical lattices becomes very important as a simulator of strongly correlated condensed matter physics [7–10].

The modern history of the field of ultracold atoms started in 1995 with Bose Einstein condensation [11] being realised in experiments, independently, by groups in Colorado [12], at MIT [13] and at Rice University [14], using Rb, Na and Li respectively. The cooling schemes that had been developed prior to these experiments include, among others, laser cooling [15], which was heavily contributed to by Chu, Cohen-Tannoudji, and Phillips (Nobel prize 1997), and evaporative cooling methods [16]. Combinations of these cooling techniques made it possible to reach temperatures in the sub-microKelvin range, needed for realising BEC in these dilute systems with a density of the order of $10^{13} - 10^{15}$ cc^{-1}. In these temperature and density ranges the system is weakly interacting. With further developments in the areas of precision control and measurements, realising strongly interacting systems was also possible [17, 18]. In 1998 Jaksch *et al.* showed that it is possible to realise the Bose-Hubbard model with ultracold atoms by loading them into optical lattices [19], and to study not only ground state but also far-from-equilibrium dynamics. An optical lattice, formed by counter-propagating lasers that produce a standing wave where a sinusoidal potential is created for the atoms via an AC-Stark shift [20], can be regarded as an especially clean lattice system. This is due to the absence of any impurity and defects that are mostly unavoidable in a solid state system. Also unlike naturally occurring crystals the lattice sites are very stable, and as the lattice itself is not formed by an assembly of particles, atom-phonon interactions are absent. Another big advantage of optical lattices is the precise control over the Hamiltonian parameters that is achieved by controlling external fields. The laser intensity determines the relative values of the tunnelling rate and interaction energy. Using Feshbach resonances [21] it is further possible to tune the interaction energy independently over a wide range of strengths and also to modify its sign, resulting in attractive or repulsive interactions. The typical values of these Hamiltonian parameters are low enough (around hundreds of Hertz) to produce slow dynamics and therefore it is possible to track non-equilibrium dynamics. The coherent evolution is possible to observe for a long time in these setups as the interactions with the environment are very weak. These favourable qualities in optical lattices make them a viable candidate for realising and studying condensed matter systems [22].

The first experimental demonstration of such effectiveness of optical lattice setups came in 2001 by Greiner *et al.* [23] who observed the superfluid to Mott insulator phase transition [24] by implementing a Bose-Hubbard Hamiltonian in a 3D optical lattice. Since then, optical lattices have been used in an extensive range of experiments including the realisation of Fermi-Hubbard models [25, 26], investigation of the properties of Bose-Fermi mixtures [27], studies of quantum quenches [28, 29], formation of repulsively bound pairs [30], and site-resolved manipulation of atomic states [31–34]. Atoms in optical lattices can also be coupled to a large BEC system to perform experiments on local non-destructive probing [35], qubit cooling [36], and the creation of bath-mediated long-range interaction [37]. The small number of particles in the optical lattices can behave like impurities. These impurities along with the Bogoliubov excitations created in the BEC demonstrate polaronic behaviour [30, 38–48]. Due to the BEC-mediated effective interaction [37, 49–51] and an increase in effective mass [52–54] induced by the interaction with BEC, there is a resulting decrease in mobility of the impurities.

In experiments with optical lattices the versatile lattice setups allow changing the relative directions of propagation of the lattice beams and their polarisations, resulting in the realisation of various lattice geometries [22]. Different dimensionalities can be achieved by making the lattice deeper in certain directions [55, 56]. It is also possible to create energy offsets at chosen sites in an optical lattice by using a commensurate superlattice as well as produce pseudo-random disorder by applying an incommensurate superlattice. The latter technique has been used to observe many-body localisation (MBL) recently using two-species fermions which has opened up a novel direction to explore [57].

Another area of extreme importance is the aforementioned prediction of realising a d-wave superfluid state with the Fermi-Hubbard model which can lead to a much better understanding of high-T_c superconductors in cuprates [2, 3]. The temperature scale required to access the strongly correlated phases of a two species Fermi-Hubbard model has to be well below the so-called Néel temperature [58]. In the strongly interacting regime this temperature is set by the spin exchange energy [59], which is the second order correction to the ground state of the Fermi-Hubbard Hamiltonian where the tunnelling term is treated perturbatively, and is of the order of J^2/U. This energy scale, being much smaller than the system parameters, corresponds to a temperature which is near to what is achieved in modern experiments [60, 61]. It is therefore extremely important to explore in detail the heating mechanisms in these experimental situations.

Noise sources that generate heating in optical lattices can be of a classical nature, e.g., the case where the intensity of the coherent laser field fluctuates inherently due to noisy electrical circuits of the device [62, 63]. The noise can also be of purely quantum nature, e.g., due to incoherent scattering of light [64–66]. In the lattice, coupling to external radiation modes gives rise to quantum noise that introduces decoherence in the system. The associated characteristic decoherence rates can be made relatively small but they will often remain comparable to the above mentioned exchange energy scale. Theoretically, these so-called open quantum systems can be studied by writing down a master equation that describes the microscopic dynamics induced by dissipation.

Solving the master equation by exact numerical simulation is possible only for very small systems, due to exponential scaling of the Hilbert space dimension. A state-of-the-art numerical method that has been extremely successful for simulations in 1D systems is the Density Matrix Renormalisation Group (DMRG) method. Originally introduced in 1992 by S. White [67, 68], the DMRG algorithm works on systems with low bipartite entanglement and calculates the ground state by truncating the Hilbert space and retaining the relevant fraction of it. Vidal's Time Evolved Block Decimation (TEBD) algorithm [69, 70], proposed in 2003, generalises this concept to enable as optimal truncation procedure to dynamically track the time evolution of the quantum state. These algorithms can be combined with techniques like quantum trajectory methods [71–73] to take care of the dissipative channels and to evolve the master equation. Apart from carrying out theoretical investigations these numerical methods are powerful tools to benchmark the optical lattice experiments.

1.2 Objective of thesis

With ultracold atoms in optical lattices providing an ideal testbed for a wide range of strongly correlated condensed matter physics problems, it is very important to address issues like dissipation resulting from interactions with the environment that set a fundamental limit on the coherent evolution of the system. The objective of this thesis is to explore the dynamical properties of quantum many-body systems affected by dissipative mechanisms that emerge in ongoing experiments with ultracold atoms in optical lattices. We particularly focus on the decoherence caused by incoherent scattering of laser light in these setups. We especially study fermionic atoms, deriving the equations of motion starting from first principles. We use both analytical methods and numerical techniques such as TEBD algorithms and quantum trajectory methods to investigate the effects of dissipation on the dynamical properties. Along with providing the framework for a master equation derivation of a multi-species fermionic system, the role of the atomic physics in determining the decoherence effects is quite interesting from an experimental point of view. We extend this work to analyse and explain the details of the decoherence mechanisms, again by starting with the atomic structure, in a recent experiment that investigates the effect of controlled decoherence on the MBL realised in a system of fermions in optical lattices. We further study a two species bosonic system to quantify the effect of inter-species entanglement on the smaller system, that can be thought of as coupled with a bath, in the context of recent experiments that look at polaronic behaviour in such systems.

1.3 Outline of thesis

With the objectives mentioned above the remainder of this thesis is organised as follows. We start in Chapter 2 with a brief introduction on the technical background necessary to understand optical lattice setups and the Hubbard models that can be realised in these experiments. The coupling to the radiation bath and the decoherence caused by spontaneous emission events are addressed in Chapter 3 where we give an overview on the master equation formalism that describes the system dynamics. The calculations to find the ground state in such systems and to evolve the system in the presence of decoherence require sophisticated numerical methods. In Chapter 4 we discuss the TEBD algorithm under the DMRG framework in this regard. We also briefly review the quantum trajectory method that deals with the evolution of the master equation under decohering effects.

After this we move to the main results of the research work carried out in this thesis. In Chapter 5 we present a detailed study of dissipative dynamics of fermions in a far-detuned optical lattice due to incoherent light scattering. We derive a many-body master equation of such a system taking into consideration the details of the atomic structure of the experimentally relevant group-I and group-II species and then present our results obtained using analytical and numerical techniques. While the derivation of the master equation for the multi-species fermions is of theoretical interest, the connection between the atomic physics and the many-body physics in these systems of strongly interacting multi-species mixtures offer new directions in experiments. The dissipative model developed here is used in our discussion in Chapter 6 where we report the findings from the analysis of experimental work carried out by our collaborators to investigate the effects of controlled dissipation on MBL realised with ultracold fermions in an optical lattice experiment. This work presents a detailed framework of studying the dissipative channels starting from the basic atomic structure in an experiment that establishes a novel scheme of studying MBL in an open quantum system. We then move to Chapter 7 to present a slightly different approach towards open quantum systems where we study two species bosons in optical lattices where one of the species acts as an impurity system while the other behaves like a bath. We report the connection between the bipartite entanglement and the visibility of the momentum distribution in such systems. We conclude in Chapter 8 and mention possible directions for future work .

1.4 Outputs from the thesis

Publications

- *Light scattering and dissipative dynamics of many fermionic atoms in an optical lattice*,
  Saubhik Sarkar, Stephan Langer, Johannes Schachenmayer, and Andrew J. Daley
  Phys. Rev. A, **90**, 023618, (2014).
- *Signatures of many-body localization in a controlled open quantum system*,
  Henrik P. Lüschen, Pranjal Bordia, Sean S. Hodgman, Michael Schreiber,

Saubhik Sarkar, Andrew J. Daley, Mark H. Fischer, Ehud Altman, Immanuel Bloch, and Ulrich Schneider
Phys. Rev. X, **7**, 011034, (2017).

- *Effect of entanglement in two species bosonic systems*,
  Saubhik Sarkar, Suzanne McEndoo and Andrew J. Daley
  (in preparation)

Talk presentations by the author of the thesis

- APS March meeting, March 18-22, 2013, Baltimore, USA
- DAMOP meeting, June 2-6, 2014, Madison, USA

Poster presentations by the author of the thesis

- DARPA OLE Review meeting, 2012 (Miami, USA), 2013 (San Francisco, USA), 2014 (Arlington, USA)
- International Conference on Atomic Physics, August 3-8, 2014, Washington D.C. USA
- DOQS workshop, October 20-22, 2014, Glasgow, UK
- CCPQ Workshop, August 3-6, 2015, Windsor, UK

Chapter 2

Optical lattices: closed quantum systems

The goal in this chapter is to give an outline of the underlying physics that eventually leads to the derivation of the many-body Hamiltonians for neutral atoms in an optical lattice, especially the Hubbard Hamiltonian. In Sec. 2.1 we start from a single atom interacting with electromagnetic field and then focus on the case of a laser-driven atom. This is followed by the derivation of the optical lattice potential generated by the laser light. In Sec. 2.2 the inter-atomic interaction is added to the treatment. We summarise the essential elastic scattering properties and discuss the two-body contact potential that describes the interactions under typical experimental conditions. In Sec. 2.3 we show the band structure created by the periodic potential of the optical lattice, which helps us to arrive at the Hubbard Hamiltonian [19]. The standard approximations with respect to the full many-body Hamiltonian are indicated, resulting in simplification of the model. We conclude this chapter with brief discussions on the Fermi-Hubbard and Bose-Hubbard Hamiltonians. We consider quantum noise, especially from light scattering, and the detailed discussion of this is presented in the next chapter.

2.1 Atom-light interaction

In this section we start with an overview of the Hamiltonian describing a single atom coupled to an electromagnetic field. In the relevant limit the atom-field interaction is then shown to be governed by a dipole coupling. We then focus on experimentally relevant situation where the atomic system is driven by a standing laser wave with an optical frequency detuned from an atomic transition. The atom can be considered as a two-level system when the laser predominantly couples two particular atomic states. We give an overview of the exact solution of the resulting *Rabi problem*. We then outline the basic properties of an optical lattice formed by the laser light in terms of AC Stark shift.

2.1.1 Single atom Hamiltonian

To derive the Hamiltonian for a single neutral atom interacting with the electromagnetic field (see, for example, [74]) one can start with classical electrodynamics where the field dynamics obey Maxwell's equations and the atomic dynamics is governed by the Newton-Lorentz equations. The field variables are the vector potential $\mathbf{A}$ and its time derivative. As we will deal only with non-relativistic situations, we choose to work in the Coulomb gauge, i.e. $\nabla \cdot \mathbf{A} = 0$. The field variables are further expressed in terms of *normal variables* which upon canonical quantisation become the photon mode annihilation and creation operators $b_{\boldsymbol{k},\lambda}$ and $b^{\dagger}_{\boldsymbol{k},\lambda}$ respectively where, $\boldsymbol{k}$ is the wavevector and λ is the polarisation of the photon mode. With $\hbar\omega_k$ as the excitation energy in each mode, the field hamiltonian is then written as $H_{\text{Field}} = \sum_{\boldsymbol{k},\lambda} \hbar\omega_k b^{\dagger}_{\boldsymbol{k},\lambda} b_{\boldsymbol{k},\lambda}$, where the zero-point energy has been omitted. This is a free field Hamiltonian as the atom is globally neutral.

Now for the atom a canonical quantisation is carried out on the conjugated position and momentum variables. For an atom with atomic number Z, comprised of a composite nucleus (mass m_n, charge q_n) and electrons (mass m_e, charge q_e), coupled to electromagnetic field, the Hamiltonian for the full system can then be written as

$$H = \frac{(\mathbf{p}_n - q_n \mathbf{A}(\mathbf{r}_n))^2}{2m_n} + \sum_{i=1}^{Z} \frac{(\mathbf{p}_i - q_e \mathbf{A}(\mathbf{r}_i))^2}{2m_e} + V_{\text{Coulomb}} + H_{\text{Field}}\,, \tag{2.1}$$

where the first term describes the kinetic energy of the nucleus which can be taken to be the centre of mass of the atom as it is much heavier than the electrons. The second term is the kinetic energy of the electrons. The Coulomb potential V_{Coulomb} is the third term. We now make use of the following observation: the relevant radiation wavelengths for the atomic system fall in the optical region and therefore are typically three orders of magnitude larger than the atomic size which is around a few Bohr radii. Therefore, for an atom located at $\mathbf{r}_0$ we can neglect the spatial variation of the field and approximate $\mathbf{A}(\mathbf{r})$ by $\mathbf{A}(\mathbf{r}_0)$. This is known as the long wavelength approximation. Using this we can now carry out the unitary transformation $U = e^{-i/\hbar \sum_j q_j \mathbf{r}_j \cdot \mathbf{A}(\mathbf{r}_0)}$ on the Hamiltonian H, resulting in

$$\begin{aligned} H \to H' &= UHU^{\dagger} \\ &= \frac{\mathbf{p}_n^2}{2m_n} + \sum_{i=1}^{Z} \frac{\mathbf{p}_i^2}{2m_e} + V_{\text{Coulomb}} - \sum_j q_j \mathbf{r}_j \cdot \mathbf{E}(\mathbf{r}_0) + H_{\text{Field}}\,, \end{aligned} \tag{2.2}$$

where a dipolar self-energy term (arising from the unitary transformation) has been omitted as it only adds a constant to the Hamiltonian. Now, for reasons stated above, the first term can be approximated as the kinetic energy of the centre of mass $\mathbf{P}_{CM}^2/2M_{CM}$, with total momentum $\mathbf{P}_{CM} = \mathbf{p}_n + \sum_{i=1}^{Z} \mathbf{p}_i$ and total mass $M_{CM} = m_n + Zm_e$. The first term in Eq. 2.2 therefore can be taken to be $\mathbf{P}_{CM}^2/2M_{CM}$, giving the kinetic energy of the atom.

The kinetic energy of the electrons and Coulomb potential in Eq. 2.2 together form the internal Hamiltonian of the atom, H_{atom}. The atomic Hamiltonian is in principle diagonalisable and we can write $H_{\text{atom}} = \hbar\omega_a |a\rangle\langle a|$, with internal energy levels $|a\rangle$ and respective energy eigenvalues $\hbar\omega_a$. This enables us to write,

$$H_{\text{atom}} = \sum_{i=1}^{Z} \frac{\mathbf{p}_i^2}{2m_e} + V_{\text{Coulomb}} \equiv \hbar\omega_a|a\rangle\langle a|\,. \tag{2.3}$$

Noting that the total dipole moment operator for the atom is $\mathbf{d} = \sum_j q_j\mathbf{r_j}$, the interaction Hamiltonian can be written as

$$H_{\text{int}} = -\sum_j q_j\mathbf{r}_j \cdot \mathbf{E}(\mathbf{r}_0) = -\mathbf{d}\cdot\mathbf{E}(\mathbf{r}_0)\,. \tag{2.4}$$

Combining all these terms, the Hamiltonian in Eq. 2.2 can be rewritten to give the complete picture,

$$\begin{aligned} H' &= \frac{\mathbf{P}_{CM}^2}{2M_{CM}} + H_{\text{atom}} + H_{\text{int}} + H_{\text{Field}} \\ &= \frac{\mathbf{P}_{CM}^2}{2M_{CM}} + \hbar\omega_a|a\rangle\langle a| - \mathbf{d}\cdot\mathbf{E}(\mathbf{r}_0) + H_{\text{Field}}\,. \end{aligned} \tag{2.5}$$

The interaction Hamiltonian H_{int} contains the most interesting physics in this expression and tells us that the atom and the field interact through dipole coupling. This arises from the long wavelength approximation, which is also known as the dipole approximation. Neglecting the spatial dependance of the field results in this lowest-order consideration of the extent of the atom. The next order terms are the magnetic dipole and electric quadrupole couplings, strengths of which are smaller by of the order of α^2 compared to the dipole term, where α is the fine structure constant, ($\approx 1/137$).

2.1.2 Mollow transformation

We now look at a case where, for the sake of simplicity, the atom is taken to be fixed in its position $\mathbf{r}_0$. This means we can neglect the first term in Eq. (2.5). The atom is now driven by a laser at frequency w_L which is detuned from the transition frequency $\omega_{e,g}$ between the ground state of the atom $|g\rangle$ and an excited state $|e\rangle$. We also assume that the laser frequency is very far away from any other atomic transition and that the laser intensity also low enough so that we can neglect any other internal atomic level in a perturbation theory approach. The laser polarisation can also be set to select a particular dipole transition element to couple two particular states of choice. The atom is therefore a two-level system for our purposes. We wish to treat the electric field generated by the laser in a classical way, which is often referred to as the semi-classical approach. This can be done as the mean occupation number of photons in the laser mode for typical laser intensities is so large that the non-commutativity of the photon creation and annihilation operators can be ignored. Therefore it is possible to treat the laser field as a complex function instead of an operator in the interaction Hamiltonian for the purposes of coherent dynamics. To see this we first consider the atom as being prepared in the ground state and subject to a multi-mode coherent wave packet which is a model of the laser field [75]. The combined system of the atom and the radiation field obeys the following Schrödinger equation,

$$\begin{aligned} i\hbar\frac{d}{dt}|\psi(t)\rangle &= H|\psi(t)\rangle \\ &= \left(\sum_a \hbar\omega_a|a\rangle\langle a| - \mathbf{d}\cdot\mathbf{E}(\mathbf{r}_0) + \sum_{\boldsymbol{k},\lambda}\hbar\omega_k b^\dagger_{\boldsymbol{k},\lambda}b_{\boldsymbol{k},\lambda}\right)|\psi(t)\rangle\,, \end{aligned} \tag{2.6}$$

where the quantum mechanical electric field operator is defined in terms of a discrete mode expansion with unit polarisation vector $\boldsymbol{\epsilon}_\lambda$ and frequency ω_k in a quantisation volume V and assuming periodic boundary condition,

$$\mathbf{E}(\mathbf{r}_0) = \sum_{\boldsymbol{k},\lambda} i\sqrt{\frac{\hbar\omega_k}{2\epsilon_0 V}}b_{\boldsymbol{k},\lambda}e^{i\mathbf{k}\cdot\mathbf{r}_0}\boldsymbol{\epsilon}_\lambda + \text{h.c.}\,. \tag{2.7}$$

The initial condition is given by

$$|\psi(t)\rangle \xrightarrow{t\to-\infty} |g\rangle\otimes D\left(\left\{\alpha_{\boldsymbol{k},\lambda}e^{-i\omega_k t}\right\}\right)|\text{vac}\rangle\,. \tag{2.8}$$

Here the multimode coherent state $|\mathrm{coh}\rangle$ is produced by the action of the unitary displacement operator on the vacuum state $|\mathrm{vac}\rangle$ i.e.

$$\begin{aligned}|\mathrm{coh}\rangle &= D\left(\left\{\alpha_{\boldsymbol{k},\lambda}e^{-i\omega_k t}\right\}\right)|\mathrm{vac}\rangle \\ &= \exp\left[\sum_{\boldsymbol{k},\lambda} b^\dagger_{\boldsymbol{k},\lambda}\alpha_{\boldsymbol{k},\lambda}e^{-i\omega_k t} - b_{\boldsymbol{k},\lambda}\alpha^*_{\boldsymbol{k},\lambda}e^{i\omega_k t}\right]|\mathrm{vac}\rangle\,. \qquad (2.9)\end{aligned}$$

This state corresponds to a classical field $\mathbf{E}_{\mathrm{cl}}(\mathbf{r}_0, t)$ in the sense that

$$\begin{aligned}&\left\langle\left\{\alpha_{\boldsymbol{k},\lambda}e^{-i\omega_k t}\right\}|\mathbf{E}(\mathbf{r}_0)|\left\{\alpha_{\boldsymbol{k},\lambda}e^{-i\omega_k t}\right\}\right\rangle \\ &= \sum_{\boldsymbol{k},\lambda} i\sqrt{\frac{\hbar\omega_k}{2\epsilon_0 V}}\alpha_{\boldsymbol{k},\lambda}e^{i(\mathbf{k}\cdot\mathbf{r}_0-\omega_k t)}\boldsymbol{\epsilon}_\lambda + \mathrm{h.c.} \\ &= \mathbf{E}_{\mathrm{cl}}(\mathbf{r}_0, t)\,. \qquad (2.10)\end{aligned}$$

The Mollow transformation [76] is a unitary transformation which allows for the atomic system to be perceived as being coupled to this classical field representing the laser with an additional coupling to the radiation field which can be taken in the vacuum state initially. In the transformed picture, the new wavefunction $|\tilde{\psi}(t)\rangle = D^\dagger\left(\{\alpha_{\boldsymbol{k},\lambda}e^{-i\omega_k t}\}\right)|\psi(t)\rangle$. This leads to the desired new initial condition,

$$\lim_{t\to-\infty}|\tilde{\psi}(t)\rangle = |g\rangle\otimes|\mathrm{vac}\rangle\,. \qquad (2.11)$$

The transformed time-dependent Hamiltonian is

$$\begin{aligned}\tilde{H} &= D^\dagger H D + i\hbar\dot{D}^\dagger D \\ &= \sum_a \hbar\omega_a|a\rangle\langle a| - \mathbf{d}\cdot\left(\mathbf{E}(\mathbf{r}_0) + \mathbf{E}_{\mathrm{cl}}(\mathbf{r}_0, t)\right) + \sum_{\boldsymbol{k},\lambda}\hbar\omega_k b^\dagger_{\boldsymbol{k},\lambda}b_{\boldsymbol{k},\lambda}\,, \qquad (2.12)\end{aligned}$$

which retains the form of the Schrödinger equation, $i\hbar|\dot{\tilde{\psi}}(t)\rangle = \tilde{H}|\tilde{\psi}(t)\rangle$. For the rest of this chapter we will not take the radiation field into account and only focus on the coupling with a classical field. This is a semi-classical treatment and gives quite a faithful description of the system at timescales short enough so that the coherent dynamics can be considered not to be disturbed by the decohering effects introduced by the radiation field. The full quantum mechanical picture will be covered in the next chapter.

2.1.3 Semi-classical approach

With the objective to focus on the coherent dynamics we now look at the Rabi problem where a localised two level atom is driven by a single mode laser field [20]. To describe the system we use the the Hamiltonian in Eq. 2.12 after omitting the coupling to the quantised radiation field and the field Hamiltonian. The laser produces a scalar electric field, $\mathbf{E}_{\text{cl}}(t) = \boldsymbol{\epsilon} E_0(t) e^{-i\omega_L t} +$ c.c., where position dependence is absent as the atom is taken to be fixed at the origin. The mode of the laser is given by its frequency ω_L and polarisation $\boldsymbol{\epsilon}$. The laser frequency differs from the atomic transition frequency by the detuning, $\Delta = \omega_L - \omega_{e,g}$. We also define the following transition operators, $\sigma_+ = |e\rangle\langle g|, \sigma_- = |g\rangle\langle e|$. The Hamiltonian for this two level atomic system driven by the laser therefore becomes

$$H_{\text{semi-cl}} = \hbar\omega_{e,g}|e\rangle\langle e| - d_{e,g}\left(\sigma_+ + \sigma_-\right)\left(E_0(t)e^{-i\omega_L t} + c.c.\right) , \tag{2.13}$$

where $d_{e,g} = \langle e|\mathbf{d}\cdot\boldsymbol{\epsilon}|g\rangle$ is the dipole transition matrix element and can be chosen to be real. In the following let us consider a square pulse for which $E_0(t) = E_0$ between time 0 and T and zero otherwise. Defining Rabi frequency $\Omega = 2d_{e,g}E_0/\hbar$ and using the unitary transformation $U = e^{i\omega_L t|e\rangle\langle e|}$, we rewrite the Hamiltonian in this rotating frame,

$$\begin{aligned} H_{\text{semi-cl}} \to H'_{\text{semi-cl}} &= UHU^\dagger + i\hbar\dot{U}U^\dagger \\ &= -\hbar\Delta|e\rangle\langle e| - \frac{\hbar\Omega}{2}\sigma_+\left(1 + e^{i2\omega_L t}\right) - \frac{\hbar\Omega}{2}\sigma_-\left(1 + e^{-i2\omega_L t}\right) . \end{aligned} \tag{2.14}$$

The rapidly rotating terms in this Hamiltonian can be neglected if the timescales we are interested are much longer than the optical time-scale set by the laser frequency. The typical relevant time-scale t in the experiments is such that in the time-evolution operator, obtained by integrating the Hamiltonian, the contribution from the rotating terms averages out to zero. Quantitatively, for $t \gg 1/\omega_L, 1/\omega_{e,g}$, we can write a simplified version of the Hamiltonian under the *rotating wave approximation* (RWA),

$$H_{\text{RWA}} = -\hbar\Delta|e\rangle\langle e| - \frac{\hbar\Omega}{2}\sigma_+ - \frac{\hbar\Omega}{2}\sigma_- \,. \tag{2.15}$$

The eigenstates of this Hamiltonian, which are known as the dressed states, are $|\phi_1\rangle = \cos\theta|g\rangle - \sin\theta|e\rangle$ and $|\phi_2\rangle = \sin\theta|g\rangle + \cos\theta|e\rangle$ with respective energies $-\hbar\Delta/2 \pm \hbar\Omega_{\text{eff}}/2$. Here θ is given by $\cos(2\theta) = -\Delta/\Omega_{\text{eff}}$ and the effective Rabi frequency $\Omega_{\text{eff}} = \sqrt{\Omega^2 + \Delta^2}$. If the atom starts in one of two levels, the population in each level oscillates with Ω_{eff}, which in the resonant case ($\Delta = 0$) is simply the normal Rabi frequency Ω.

When the detuning is small, with the use of the RWA and a two level atom, the Hamiltonian can be exactly diagonalised. However we sometimes work in regimes of large detuning where the RWA and the two-level approximation break down. In the following section we first show how a spatially-varying optical potential is formed by the laser field by using perturbation theory (as coupling to the laser field is small compared to optical frequencies) for the two level atoms. We then also mention the behaviour when the treatment is expanded beyond the two-level approximation.

2.1.4 Optical lattice potential

In this section we give an overview of how an optical lattice potential is formed. To do so we again consider the two level atom described by the wavefunction $|\psi(t)\rangle = c_g(t) + c_e(t)e^{-i\omega_{eg}t}|e\rangle$. In the presence of a classical electric field varying in both time and space, $\mathbf{E}_{\text{cl}}(\mathbf{r}, t) = \boldsymbol{\epsilon} E_0(\mathbf{r})e^{-i\omega_L t}+$ c.c., we use time-dependent perturbation theory to write down the coupled equations for the amplitudes,

$$\begin{aligned} \dot{c_g} &= -ic_e e^{i\omega_{e,g}t}\left(\frac{\Omega(\mathbf{r})}{2}e^{-i\omega_L t} + \frac{\Omega^*(\mathbf{r})}{2}e^{i\omega_L t}\right) \\ \dot{c_e} &= -ic_g e^{-i\omega_{e,g}t}\left(\frac{\Omega^*(\mathbf{r})}{2}e^{-i\omega_L t} + \frac{\Omega(\mathbf{r})}{2}e^{i\omega_L t}\right) \,. \end{aligned} \tag{2.16}$$

Initially the atom is taken to be in the ground state $|g\rangle$, i.e. $c_g(0) = 1$, and $c_e(0) = 0$. Now to first order in perturbation we can write the wavefunction as,

$$|\psi(t)\rangle^{(1)} = |g\rangle + \left[\frac{\Omega(\mathbf{r})}{2}\frac{e^{-i\omega_L t}-1}{\omega_{e,g}-\omega_L} + \frac{\Omega^*(\mathbf{r})}{2}\frac{e^{i\omega_L t}-1}{\omega_{e,g}+\omega_L}\right]|e\rangle \,. \tag{2.17}$$

We can now write down the second-order equation for the amplitude associated with the ground state,

$$\begin{aligned}&\dot{c_g}^{(2)}(t)\\ =&ie^{-i\omega_{e,g}t}\left(\frac{\Omega(\mathbf{r})}{2}e^{i\omega_L t} + \frac{\Omega^*}{2}e^{-i\omega_L t}\right)\left[\frac{\Omega\mathbf{r})}{2}\frac{e^{-i\omega_L t}-1}{\omega_{e,g}-\omega_L} + \frac{\Omega^*(\mathbf{r})}{2}\frac{e^{i\omega_L t}-1}{\omega_{e,g}+\omega_L}\right] \,.\end{aligned} \tag{2.18}$$

We can write the solution to be of the form $c_g(t) = e^{i\phi(t)}$, with a complex phase ϕ in general. Averaging over one cycle of oscillation of the electric field and neglecting the fast rotating terms we obtain,

$$\langle\dot{\phi}\rangle_{T=\frac{2\pi}{\omega_L}} = \frac{|\Omega(\mathbf{r})|^2}{4}\left[\frac{1}{\omega_{e,g}+\omega_L} + \frac{1}{\omega_{e,g}-\omega_L}\right] \,, \tag{2.19}$$

where on the right hand side c_g is replaced by unity as we are working to the second-order in perturbation. Eq. (2.19) corresponds to an energy shift in the ground state due to an oscillating electric field, $\Delta E_g = -\hbar\langle\dot{\phi}\rangle_{T=2\pi/\omega_L}$ which is known as the AC Stark shift [20]. The perturbative approach is valid as long as ω_L is far-detuned from any of the transition frequencies and all the excited state amplitudes remain small. The ground state energy shift is then given by

$$\Delta E_g = -\frac{|\Omega(\mathbf{r})|^2}{4}\frac{2\hbar\omega_{e,g}}{\omega_{e,g}^2-\omega_L^2} \,. \tag{2.20}$$

A simple optical lattice in 1D can be formed by retro-reflecting a laser beam to construct a standing wave, which gives rise to a sinusoidal Rabi frequency, $\Omega(x) = 2\langle e|\mathbf{d}\cdot\boldsymbol{\epsilon}|g\rangle E_0 \sin(k_L x)/\hbar \equiv \Omega_0 \sin(k_L x)$, where k_L is the laser wave number. The resulting potential seen by atoms loaded in the ground state is the 1D optical lattice potential, $V_{\text{opt}}(x) = (\Omega_0^2/4\Delta)\sin^2(k_L x) \equiv V_0 \sin^2(k_L x)$. This is also the basic potential for dipole traps. For blue detuning $(\Delta > 0)$ the the atoms prepared in the ground state are trapped at the intensity minimum and for red detuning ($\Delta < 0$) the the atoms are trapped at the intensity maximum. In higher dimensions, periodic optical potentials can be formed by increasing the number of laser beams. For example, in 2D a simple square lattice is formed by superimposing two orthogonal standing waves with orthogonal polarisations. Similarly a simple cubic lattice in 3D can be formed by standing waves which are orthogonal both in spatial directions and in polarisations.

Now in the case where the classical electric field is chosen in such a way that not a single transition frequency can be picked out to be significantly less detuned than the others, we have to take other exited levels into account. This multi-level treatment is a straight-forward generalisation of the two level case where the shift in the ground state energy is given by,

$$\begin{aligned}\Delta E_g = -\sum_{n\neq g} \frac{|\Omega_{n,g}(\mathbf{r})|^2}{4} \frac{2\hbar\omega_{n,g}}{\omega_{n,g}^2 - \omega_L^2} &= -\sum_{n\neq g} \frac{|\langle n|\mathbf{d}\cdot\boldsymbol{\epsilon}|g\rangle E_0(\mathbf{r})|^2}{\hbar} \frac{2\omega_{n,g}}{\omega_{n,g}^2 - \omega_L^2} \\ &\equiv -\frac{1}{2}\alpha(\omega_L)|E_0(\mathbf{r})|^2 \,, \end{aligned} \tag{2.21}$$

where $\omega_{n,g}$ is the energy of the excited level n and the position dependent Rabi frequency between levels n and g is defined as $\Omega_{n,g}(\mathbf{r}) = 2\langle n|\mathbf{d}\cdot\boldsymbol{\epsilon}|g\rangle E_0(\mathbf{r})/\hbar$. This expression gives an intuitive picture of the energy shift in terms of a product of the classical light intensity and a *polarisability*.

2.2 Inter-atomic interactions

To go from a single atom picture to the many-body picture inter-atomic interactions must be taken into account. For a very dilute gas of atoms at ultracold temperatures the interaction can be described by two-body elastic collision at low energies. Therefore we first summarise the main results for the elastic scattering of two particles [77] separated by $\mathbf{r}$ under the action of the spherically symmetric potential $V(r = |\mathbf{r}|)$. In relative coordinates the motion is governed by the Hamiltonian, $H_{\mathrm{rel}} = \mathbf{p}^2/2\mu + V(r)$ where the relative momentum $\mathbf{p} = \mathbf{p}_1 - \mathbf{p}_2$, and the reduced mass $\mu = m_1 m_2/(m_1 + m_2) = m/2$ (for similar particles). The incoming plane wave and the scattering state are then incorporated in the asymptotic relative wavefunction which can be written as an integral solution,

$$\begin{aligned}\psi(\mathbf{r}) \xrightarrow{\text{large } r} & e^{i\mathbf{k}\cdot\mathbf{r}} - \frac{\mu}{2\pi\hbar^2}\frac{e^{ikr}}{r}\int d^3r' e^{-ik\hat{\mathbf{r}}\cdot\mathbf{r}'} V(r')\psi(\mathbf{r}') \\ \equiv & e^{i\mathbf{k}\cdot\mathbf{r}} + f(\mathbf{k},\mathbf{r})\frac{e^{ikr}}{r}\,, \end{aligned} \tag{2.22}$$

where the scattering amplitude $f(\mathbf{k},\mathbf{r})$ only depends on k and the scattering angle θ, between $\mathbf{k}$ and $\mathbf{r}$. Taking advantage of the spherical symmetry of the problem one can write the wavefunction in a basis of spherical waves. When the incoming wave direction is taken along the z-direction, this partial wave expansion enables one to rewrite the scattering amplitude as

$$f(k,\theta) = \sum_{l=0}^{\infty} \frac{2l+1}{k\cot\delta_l - ik} P_l(\cos\theta)\ , \tag{2.23}$$

where δ_l are the scattering phase shifts associated the l-th partial wave and P_l are the Legendre polynomials. The total scattering cross-section is then given by

$$\sigma = \frac{4\pi}{k^2}\sum_{l=0}^{\infty}(2l+1)\sin^2\delta_l\,. \tag{2.24}$$

In the next step an approximation based on the low energy limit ($kr_0 \ll 1$) is used. In this limit it can be shown that $\delta_l \sim k^{2l+1}$, for small l values and for short range potentials. Therefore only $l = 0$ i.e. s-wave scattering is important in terms of contribution to the total scattering rate at low energies. This allows us to write the expansion, $k\cot\delta_0 \approx -1/a_s + r_0k^2/2$. Here, a_s is the scattering length which determines the strength and the nature of the interaction and r_0 is the effective range of the scattering potential. Using this we then get for the scattering amplitude in the far field

$$f(k) \approx \frac{1}{-\frac{1}{a_s} - ik + \frac{1}{2}r_0k^2} \to -a_s \quad (\text{as } k \to 0)\,. \tag{2.25}$$

Therefore the scattering length a_s is the only parameter to which the description of a low energy scattering process reduces to. The total scattering cross-section then essentially analogous to a low-energy hard-sphere potential problem, $\sigma \sim 4\pi a_s^2$. It is important to note that so far we have considered the case of distinguishable particles. For identical bosons and indistinguishable fermions with different spin states only the even l terms enter in the sum (2.24) , with twice the strength. The total s-wave scattering cross-section is therefore $8\pi a_s^2$. For identical fermions, where only odd l terms matter in the sum (2.24), the total s-wave scattering cross-section is zero.

For a dilute cold gas loaded into optical lattices the diluteness is characterised by two parameters: the inter-particle distance $\rho^{1/3}$ (ρ is the density) and the scattering length a_s. When the condition $\rho^{1/3} a_s \ll 1$ is met, elastic two-body scattering theory gives a good description of the interaction. In typical experimental situations we are also interested in very low-energy particles, which means it is sufficient to consider only s-wave scattering. This condition is satisfied when $kr_0 \ll 1$ where k is the incoming wavenumber. In cold atom experiments the interaction potential at long distances, where the electronic wavefunctions of the atom barely overlap, can be modelled as a van der Waals potential. In this case, the effective range is given by the van der Waals length [11]. At short distances the overlap between the electronic wavefunctions gives rise to quantum mechanical exchange interactions. The exact inter-atomic potential is difficult to determine and to perform calculations with. However, detailed knowledge of the exact potential is not necessary to describe the cold atom experiments as the diluteness and the low temperatures ensure that the average separation and the thermal de Broglie wavelength are much larger than the effective range of inter-atomic potential. Therefore, a model potential that is convenient to work with can be used as long as it produces the same scattering results in these parameter regimes. As we have shown, the only relevant scattering parameter under these experimental conditions is the scattering length, which therefore characterises the effect of the scattering potential. In experimental situations the scattering length can be widely tuned e.g. using Feshbach resonances [21], and varied from negative values (attractive interactions) to positive values (repulsive interactions).

Now, to model the real inter-atomic potential with a *pseudo-potential* that produces exact same scattering properties and is treatable in Born approximation, we use a two-body contact potential along with a regularising operator, introduced by Fermi [77, 78]. For identical particles of mass m this pseudo-potential acts on the relative wavefunction in the following way,

$$V_p(\mathbf{r})\psi(\mathbf{r}) \equiv \frac{4\pi\hbar^2 a_s}{m}\delta(\mathbf{r})\left[\frac{\partial[r\psi(\mathbf{r})]}{\partial r}\right]_{r=0} . \tag{2.26}$$

Using this pseudo-potential for the two-body interaction we can write the second quantised many-body Hamiltonian, with an external potential $V_{\text{ext}}(|\mathbf{r}|)$, as

$$H = \int d^3r\psi^\dagger(\mathbf{r})\left[-\frac{\nabla^2}{2m} + V_{\text{ext}}(\mathbf{r})\right]\psi(\mathbf{r}) + \frac{1}{2}\int d^3rd^3r'\psi^\dagger(\mathbf{r})\psi^\dagger(\mathbf{r}')V_p(\mathbf{r}-\mathbf{r}')\psi(\mathbf{r}')\psi(\mathbf{r}) , \tag{2.27}$$

with field operators $\psi(\mathbf{r})$. In the weak interaction limit ($k|a_s| \ll 1$), when Born approximation is valid this Hamiltonian can be rewritten with a coupling constant $g = 4\pi\hbar^2 a_s/m$ as [77]

$$H = \int d^3r\psi^\dagger(\mathbf{r})\left[-\frac{\nabla^2}{2m} + V_{\text{ext}}(\mathbf{r})\right]\psi(\mathbf{r}) + \frac{g}{2}\int d^3r\psi^\dagger(\mathbf{r})\psi^\dagger(\mathbf{r})\psi(\mathbf{r})\psi(\mathbf{r}) . \tag{2.28}$$

2.3 Lattice Hamiltonian

In order to derive a convenient many-body Hamiltonian for cold atoms loaded in an optical lattice we first investigate the band structure for a single atom which is the characteristic of a periodic potential. This will help in the construction of a convenient basis in terms of the eigenfunctions of the single-particle Hamiltonian.

2.3.1 Bloch functions

Based on our discussions in Sec. 2.1, we can write down the Hamiltonian for a cold atom with mass m in a far-detuned 1D optical lattice, $H = p^2/2m + V_{\text{opt}}(x)$

where $V_{\text{opt}}(x) = V_0 \sin^2(k_L x)$, and the periodicity is given by the lattice constant $a = \pi/k_L$. For such a periodic potential the eigenfunctions of the Hamiltonian can be obtained by applying Bloch's theorem [79] and can be written as

$$\phi_q^{[n]}(x) = e^{iqx} u_q^{[n]}(x)\,, \tag{2.29}$$

where n is the band index and q is the quasi-momentum which resides in the first Brilloiun zone $(-\pi/a, \pi/a]$. $u_q^{[n]}(x)$ are the Bloch functions and have the same periodicity as the lattice potential. They are the eigenfunctions of the Hamiltonian, $H_q = (p + \hbar q)^2/2m + V_{\text{opt}}(x)$ and are normalised as follows:

$$\int_0^a |u_q^{[n]}(x)|^2 dx = \frac{a}{2\pi}\,, \tag{2.30}$$

which is applicable to $\phi_q^{[n]}(x)$ as well. The eigenvalues of H or H_q are the band energies $E_q^{[n]}$ and they give rise to the band structure.

For a simple sinusoidal lattice potential the Bloch functions can be determined analytically by rewriting the eigenvalue equation in a Mathieu equation form, the solution to which is known, but is quite a complicated function. For this reason and for non-sinusoidal lattice potentials it is often more convenient to calculate them numerically. To do so we first write them as a Fourier expansion,

$$u_q^{[n]}(x) = \sum_l c_l^{[n,q]} e^{i2k_L x l}\,, \tag{2.31}$$

where the complex coefficients $c_l^{[n,q]}$ obey the linear eigenvalue equation,

$$\sum_{l'=-N}^{N} H_{l,l'} c_{l'}^{[n,q]} = E_q^{[n]} c_l^{[n,q]}\,. \tag{2.32}$$

The matrix elements are defined as,

$$H_{l,l'} = \begin{cases} (2l + q/k_L)^2 E_R + \frac{V_0}{2} & l = l' \\ -\frac{V_0}{4} & |l - l'| = 1 \\ 0 & |l - l'| \geq 1 \end{cases}\,, \tag{2.33}$$

where $E_R = \hbar^2 k_L^2/2m$ and is called the recoil energy which is a natural energy scale in the lattice problem. The name comes from the kinetic energy that is imparted on the particle if it emits a photon with the lattice frequency. Strictly speaking for exact results, the value of N should be infinity but in practice very small values like $N \sim 10$ produce quite accurate results for the lowest few bands. We show the band structure in Fig. 2.1 where $E_q^{[n]}$ is plotted against q for two different values of the potential depth $V_0 = E_R$ and $V_0 = E_R$. One of the important and useful features of the band structure is that the band gap between the lowest two bands increases with the depth of the potential. This gap is almost uniform for lattices that are deep enough and is approximately given by the *trapping frequency*, $\omega_T = 2\sqrt{V_0 E_R}/\hbar$. In experiments with cold atoms all the other energy scales are usually made at least two orders magnitude smaller than ω_T. The essential physics therefore generally takes place in the lowest Bloch band.

2.3.2 Wannier functions

For the lattice model it is quite convenient to introduce a second set of complete orthonormal functions for the single particle Hilbert space, called Wannier functions [80], as they are localised around each lattice site. They are defined by a transformation of the Bloch function basis,

$$w^{[n]}(x - x_j) = \sqrt{\frac{a}{2\pi}} \int_{-\pi/a}^{\pi/a} e^{-iqx_j} \phi_q^{[n]}(x) dq \,, \tag{2.34}$$

where x_j is the primitive translational vector of the lattice, denoting the position of the j-th lattice site, given by the energy minima of the lattice potential. This definition suffers from an ambiguity arising from the arbitrariness of the global phase factor of the Bloch functions. We choose to work with a prescribed method as shown in Ref. [81]. This proper choice of phase ensures the existence of a unique real and exponentially localised Wannier function that is either symmetric or antisymmetric at the position of a particular site. These are known as *maximally localised* Wannier functions and will

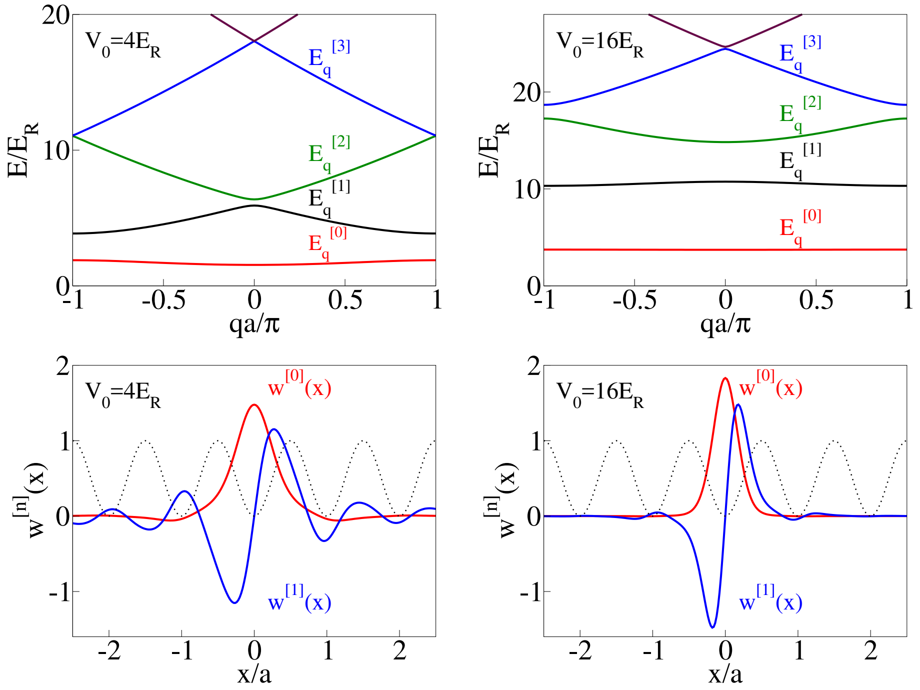

FIGURE 2.1: Band Structure and maximally localised Wannier functions, computed numerically. As the optical lattice potential becomes deeper, from $V_0 = 4E_R$ (left panels) to $V_0 = 16E_R$ (right panels), the band gap between the lowest two bands become larger and the bands get flatter (top panels) and the Wannier functions get more localised around the lattice sites (bottom panels). The Wannier functions are symmetric (antisymmetric) for even (odd) band index.

be used for all our calculations here onwards. We plot such Wannier functions in Fig. 2.1, again for two different values of the potential depth. The Wannier functions are more localised in the deep lattice limit i.e. $V_0 \gg E_R$, and they can be approximated by simple harmonic oscillator (SHO) wavefunctions. For a deep lattice the potential near the minima can be approximated by $V_{\text{opt}}(x) = V_0 \sin^2(k_L x) \approx V_0 (k_L x)^2 = (1/2) m\omega_T^2 x^2$, with $\omega_T = 2\sqrt{V_0 E_R}/\hbar$. The ground state for this SHO potential is $\psi^{[0]}_{\text{SHO}} = (1/(\pi a_0^2)^{1/4}) e^{-x^2/2a_0^2}$. The oscillator length $a_0 = \sqrt{\hbar/m\omega_T}$ denotes the extension of the wavefunction. This is a good approximation of the Wannier function in the lowest band if the *Lamb Dicke parameter* $\eta = k_L a_0 \ll 1$.

Any single particle state can be written in the basis of Wannier states defined as,

$$|w_j^{[n]}\rangle = \int w^{[n]}(x - x_j)|x\rangle dx \,. \tag{2.35}$$

In 3D this is easily generalisable to $|w_{\mathbf{j}}^{[n]}\rangle = |w_{j_x}^{[n]}\rangle \otimes |w_{j_y}^{[n]}\rangle \otimes |w_{j_z}^{[n]}\rangle$. The vector of indices $\mathbf{j}$ can accommodate different lattice constants in general. We will use this Wannier basis expansion in the following subsection to arrive at the Hubbard Hamiltonian for many cold atoms in optical lattices.

2.3.3 Hubbard Hamiltonian

To derive the many-body Hamiltonian for a 3D optical lattice system [19, 22] we consider a general bosonic or fermionic species of cold atoms experiencing the lattice potential $V_{\text{opt}}(\mathbf{r})$ and an external potential $V_{\text{ext}}(\mathbf{r})$ which, for example, can be a trap potential in an experiment. The microscopic description of such a system with two-body contact interaction modelled by a pseudo-potential as discussed in Sec. 2.2 is given by the following second quantised Hamiltonian,

$$\begin{aligned} H =& \sum_\sigma \int d^3r \psi_\sigma^\dagger(\mathbf{r}) \left[-\frac{\hbar^2}{2m}\nabla^2 + V_{\text{opt}}(\mathbf{r}) + V_{\text{ext}}(\mathbf{r}) \right] \psi_\sigma(\mathbf{r}) \\ &+ \frac{g}{2} \sum_{\sigma,\sigma'} \int d^3r \psi_\sigma^\dagger(\mathbf{r}) \psi_{\sigma'}^\dagger(\mathbf{r}) \psi_{\sigma'}(\mathbf{r}) \psi_\sigma(\mathbf{r}) \,, \end{aligned} \tag{2.36}$$

where the field operators $\psi_\sigma(\mathbf{r})$ carry a spin index σ and obey the standard canonical commutation or anti-commutation relations for bosonic and fermionic systems respectively. The field operator at position $\mathbf{r} \equiv (x, y, z)$ and spin σ is then written in the Wannier function basis,

$$\psi_\sigma(\mathbf{r}) = \sum_{n,\mathbf{i},\sigma} w^{[n]}(x - x_{i_x}) w^{[n]}(y - y_{i_y}) w^{[n]}(z - z_{i_z}) a_{\mathbf{i},\sigma}^{[n]} \,, \tag{2.37}$$

with the particle annihilation (creation) operators $a_{\mathbf{i},\sigma}^{[n]}$ $\left(a_{\mathbf{i},\sigma}^{[n]\dagger}\right)$ at site $\mathbf{i} \equiv (i_x, i_y, i_z)$ for the n-th Bloch band obeying commutation or anti-commutation relations for bosons and fermions respectively.

With the Wannier expansion the multi-band Hamiltonian can be written as

$$H = -\sum_{\substack{m,n\\ \mathbf{i},\mathbf{j},\sigma}} J^{m,n}_{\mathbf{i},\mathbf{j}} a^{[m]\dagger}_{\mathbf{i},\sigma} a^{[n]}_{\mathbf{j},\sigma} + \sum_{\substack{k,l,m,n\\ \mathbf{i},\mathbf{j},\mathbf{p},\mathbf{q},\sigma,\sigma'}} \frac{U^{k,l,m,n}_{\mathbf{i},\mathbf{j},\mathbf{p},\mathbf{q}}}{2} a^{[k]\dagger}_{\mathbf{i},\sigma} a^{[l]\dagger}_{\mathbf{j},\sigma'} a^{[m]}_{\mathbf{p},\sigma'} a^{[n]}_{\mathbf{j},\sigma} + \sum_{\substack{m,n\\ \mathbf{i},\mathbf{j},\sigma}} a^{[m]\dagger}_{\mathbf{i},\sigma} a^{[n]}_{\mathbf{j},\sigma} \,, \tag{2.38}$$

where the generic tunnelling term, interaction term and energy-offset term are respectively given by,

$$J^{n}_{\mathbf{i},\mathbf{j}} = -\int d^3 r w^{[n]*}(\mathbf{r}-\mathbf{r}_{\mathbf{i}}) \left[-\frac{\hbar^2}{2m}\nabla^2 + V_{\text{opt}}(\mathbf{r})\right] w^{[n]}(\mathbf{r}-\mathbf{r}_{\mathbf{j}}) \,, \tag{2.39}$$

$$U^{k,l,m,n}_{\mathbf{i},\mathbf{j},\mathbf{p},\mathbf{q}} = g\int d^3 r w^{[k]*}(\mathbf{r}-\mathbf{r}_{\mathbf{i}}) w^{[l]*}(\mathbf{r}-\mathbf{r}_{\mathbf{j}}) w^{[m]}(\mathbf{r}-\mathbf{r}_{\mathbf{p}}) w^{[n]}(\mathbf{r}-\mathbf{r}_{\mathbf{q}}) \,, \tag{2.40}$$

$$\epsilon^{m,n}_{\mathbf{i},\mathbf{j}} = \int d^3 r w^{[m]*}(\mathbf{r}-\mathbf{r}_{\mathbf{i}}) V_{\text{ext}}(\mathbf{r}) w^{[n]}(\mathbf{r}-\mathbf{r}_{\mathbf{j}}) \,. \tag{2.41}$$

We now focus on the 1D case which we primarily deal with analytically and numerically for the research projects in this thesis. Experimentally quasi-1D regimes are created by confining the optical lattice along the two transverse directions, for example along y and z for the lattice along x direction. This can be done by making the optical lattice potential very deep along the y and z directions. So for the potential, $V_{\text{opt}}(\mathbf{r}) = V_{0x}\sin^2(k_{L_x}x) + V_{0y}\sin^2\left(k_{L_y}y\right) + V_{0z}\sin^2(k_{L_z}z)$ one takes $V_{0y}, V_{0z} \gg V_{0x}$. Taking $V_{0y} = V_{0z} = V_{0\perp}$ and $k_{L_y} = k_{L_z} = k_{L\perp}$ we can approximate the deep transverse part of the lattice for a single 1D tube as,

$$V_{\perp}(y,z) = V_{0\perp}\left(\sin^2(k_\perp y) + \sin^2(k_\perp z)\right) \approx \frac{1}{2}m\omega_\perp^2\left(y^2+z^2\right) \,, \tag{2.42}$$

with the definition $\omega_\perp = \sqrt{2V_{0\perp}k_\perp^2/m}$. From this we can define the quasi 1D version of the two-body coupling constant g as $g^{[1]} = 2\hbar\omega_\perp a_s$. We now go on to make the first simplification on the Hamiltonian where we restrict the system to the lowest Bloch band. Contributions from all the other higher bands can be neglected if all the other energy terms such as the temperature, tunnelling term and the interaction energy are much smaller the band separation energy $\hbar\omega_T$. This condition is readily met when the potential depth V_0 is greater than several E_R. Also, in this deep lattice limit, the Wannier functions are better localised which results in another simplification given by the *tight binding approximation*. Here we take the effects coming from nearest-neighbour interaction terms and next-nearest-neighbour tunnelling terms to be negligible. Now we can write the single band Hamiltonian, with the band index omitted,

$$H = -J \sum_{\langle i,j \rangle,\sigma} a^{\dagger}_{i,\sigma} a_{j,\sigma} + \frac{U}{2} \sum_{i,\sigma} a^{\dagger}_{i,\sigma} a^{\dagger}_{i,\sigma'} a_{i,\sigma'} a_{i,\sigma} + \sum_{i,\sigma} \epsilon_i a^{\dagger}_{i,\sigma} a_{i,\sigma} \,, \tag{2.43}$$

with the following definitions for the nearest-neighbour tunnelling term J, onsite interaction term U and onsite energy offset ϵ_i, respectively,

$$J = -\int dx w^*(x) \left[-\frac{\hbar^2}{2m} \frac{d}{dx^2} + V_{\text{opt}}(x) \right] w(x-a) \,, \tag{2.44}$$

$$U = g^{[1]} \int dx |w(x)|^4 \,, \tag{2.45}$$

$$\epsilon_i = \int dx V_{\text{ext}}(x) |w(x - x_i)|^2 \,. \tag{2.46}$$

The derivation of the Hubbard model is the major objective of this chapter where we have shown that if a dilute ultracold gas where we can model the interaction by two-body contact potential, is trapped in a sufficiently deep optical lattice setup, then the essential physics can be explained by this single band Hamiltonian. So far we have not elaborated on the particle statistics which give rise to very interesting phenomena even in the ground states of these systems. In the following subsections we give a brief overview of fermionic and bosonic systems.

2.3.4 Fermi-Hubbard Hamiltonian

The Hubbard Hamiltonian was historically developed for fermions first, particularly in the context of strongly correlated electrons moving in a lattice [1]. A simple single band homogeneous ($\epsilon_i = 0$) Fermi-Hubbard Hamiltonian in the backdrop of experiments with optical lattices with two spin degrees of freedom

$\sigma \in \{\uparrow, \downarrow\}$ is given by

$$H_{\mathrm{FH}} = -J \sum_{\langle i,j \rangle, \sigma} c_{i,\sigma}^{\dagger} c_{j,\sigma} + U \sum_{i} n_{i,\uparrow} n_{i,\downarrow} \,, \tag{2.47}$$

where the fermionic annihilation and creation operators $c_{i,\sigma}$, and $c_{i,\sigma}^{\dagger}$ obey the anti-commutation relation $\left\{c_{i,\sigma}, c_{j,\sigma'}^{\dagger}\right\} = \delta_{i,j}\delta_{\sigma,\sigma'}$. The number operator at the i-th site, $n_{i,\sigma} = c_{i,\sigma}^{\dagger} c_{i,\sigma}$ can have eigenvalues 0 and 1 due to the Pauli exclusion principle. In the non-interacting case ($U = 0$) and for unity filling the system therefore is a band insulator. For average filling factor less than 1, the behaviour of the system is metallic. The Fermi-Hubbard model is exactly solvable in 1D, using Bethe ansatz [82]. The lack of general analytical and exact numerical solutions in higher dimensions prevents us from having the definite phase diagram, especially in 2D. A more theoretically well understood regime is the case of half filling. A schematic version of the phase diagram is presented in the Fig. 2.2, adapted from Ref. [59], for a three dimensional homogeneous Fermi-Hubbard model at half filling. In this case, when the interactions are attractive, then for sufficiently low temperature the system is in a superfluid regime which shows a BEC-BCS crossover [83]. For weak attractive interactions loosely bound pairs are formed analogous to BCS pairing in superconductors. For large values of attractive interaction (beyond a critical value of ($|U|/J$)) tightly bound pairs of fermions appear which behave as composite bosons, with repulsive hard-core interactions. Their tunnelling rate can be calculated in second-order perturbation theory and is proportional to J^2/U [84]. Below a critical temperature set by their tunnelling rate, these composite bosons undergo Bose-Einstein condensation. Above this temperature a phase of uncondensed and preformed pairs is predicted [85].

Now on the repulsive side of the interaction at higher temperature and weak repulsion the system is in a delocalised metallic Fermi liquid phase. As the repulsion is increased a transition into a paramagnetic Mott insulator phase appears which does not display any spin order. As the temperature is decreased, below a critical *Néel temperature* an antiferromagnetic phase with spin order sets in [58]. The value of Néel temperature decreases exponentially with J/U for weak repulsions

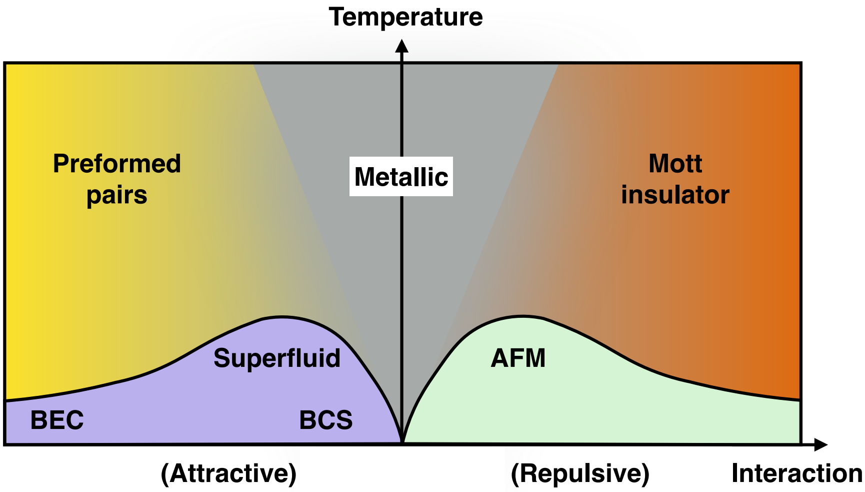

FIGURE 2.2: Schematic phase diagram for the ground state of the homogeneous Fermi-Hubbard Hamiltonian at half filling in three dimension (adapted from [59]). The abbreviations used are the following: BEC for Bose Einstein Condensation, BCS for Bardeen-Cooper-Schrieffer, AFM for anti-ferromagnetic phase.

and is proportional to J^2/U for strong repulsions [86], making the order detection harder in experiments [33, 34, 60, 61].

2.3.5 Bose-Hubbard Hamiltonian

For a homogenous system of single-species bosons in an optical lattice we can write down the Bose-Hubbard Hamiltonian. This Hamiltonian predicts a quantum phase transition from a superfluid phase to a Mott insulator phase [24]. Experimental observation of this transition set a benchmark for quantum simulation with cold atoms [23]. As a guide to the essential behaviour the zero temperature phase boundaries can be computed in a grand canonical formalism. In order to ensure that the particle number is fixed we have to add a chemical potential term to the Hamiltonian, i.e.,

$$H_{\mathrm{BH}} = -J \sum_{\langle i,j \rangle} b_i^\dagger b_j + \frac{U}{2} \sum_i n_i \left(n_i - 1\right) - \mu \sum_i n_i \,, \tag{2.48}$$

where the bosonic annihilation and creation operators b_i, and $b_i^\dagger$ obey the commutation relation $\left[b_i, b_j^\dagger\right] = \delta_{i,j}$, and $n_i = b_i^\dagger b_i$ is the number operator at the i-th site. The two quantum phases are the ground states of the system depending on the interplay of the strength of U and J values. When the tunnelling term dominates i.e. $(U/J) \to 0$ then the particles are in a superfluid state, delocalised over the lattice. This state shows an off-diagonal long range order, where the off-diagonal single particle density matrix elements fall off polynomially (in 1D) with the distance between the sites. For a lattice of M sites with N bosons on it, the superfluid ground state would be

$$|\psi_{\mathrm{SF}}\rangle \xrightarrow{U/J\to 0} \left(\frac{1}{M}\sum_{i=1}^{M} b_i^\dagger\right)^N |0\rangle\,. \tag{2.49}$$

In the thermodynamic limit $(M, N \to \infty, N/M$ finite) this state approaches a product of local coherent states

$$|\psi_{\mathrm{SF}}\rangle \xrightarrow{U/J\to 0} \prod_{i=1}^{M}\left[\exp\left(\sqrt{\frac{N}{M}} b_i^\dagger\right)|0\rangle_i\right], \tag{2.50}$$

showing Poisson number statistics. In the other limit i.e. $(J/U) \to 0$ the interaction term dominates, and to avoid the energy penalty to have more than the mean number of particles at each site for a commensurate lattice, at all sites particles are exponentially localised. In this Mott insulator state the off-diagonal single particle density matrix elements decay exponentially with the distance between the sites. With the average filling factor $n = N/M$ being an integer, this state is

$$|\psi_{\mathrm{MI}}\rangle \xrightarrow{J/U\to 0} \prod_{i=1}^{M}\left(b_i^\dagger\right)^n |0\rangle\,. \tag{2.51}$$

Mean-field calculations [87] show that for the critical value of phase transition $(U/J)_c = 5.8z$ for $\bar{n} = 1$ and $(U/J)_c = 4\bar{n}z$ for $\bar{n} > 1$, z being the coordination number. The mean field estimations suffer from large deviations in 1D where the numerical results [88] show that $(U/J)_c = 3.37$ for $\bar{n} = 1$ and $(U/J)_c = 2\bar{n}$ for $\bar{n} > 1$. In Ref. [89] a second order perturbation theory approach within the

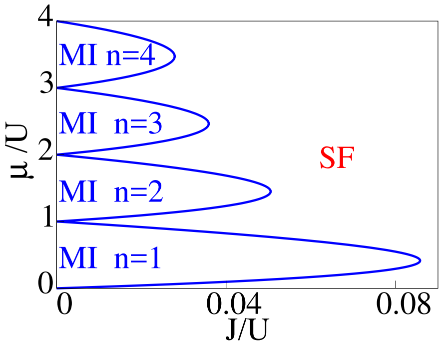

Figure 2.3: Zero-temperature mean-field phase transition in Bose-Hubbard model between the superfluid (SF) and Mott insulator (MI) state. For each integer filling factor n the MI phase resides inside the Mott lobes denoted by the blue phase boundaries.

mean field treatment gives the critical $(J/U)_c$ value that forms the boundary of the phase transition (shown in Fig. 2.3),

$$\left(\frac{J}{U}\right)_c = \frac{(n - \mu/U)\,(1 - n + \mu/U)}{z\,(1 + \mu/U)}\,, \tag{2.52}$$

where the filling factor n follows $n - 1 < \mu/U < n$.

We now conclude this chapter where an overview of the derivation of the Hubbard Hamiltonian that can be realised with cold atoms in optical lattices is presented. The steps to achieve this include discussions on atom-light interaction, inter-atomic interactions and the band structure in the optical lattices. In the next chapter we will discuss the coupling of the optical lattice systems to the quantised radiation fields.

Chapter 3

Optical lattices: open quantum systems

We have so far described neutral atoms in optical lattices as an isolated system, setting aside the coupling to the radiation bath given by the field Hamiltonian. In this chapter we are going to discuss the effects of including the field operators that are taken to be the sources of decoherence in this thesis. In Sec. 3.1 we take the simpler case of an atom that is static and interacts with both the driving laser field and the radiation field. After deriving the master equation that describes the dynamics of the atomic density operator, we move to a many-atom picture where the atoms are static at their positions in Sec. 3.2. A discussion of the many-body master equation where the atomic motion is also taken into account is presented in Sec. 3.3.

3.1 Single atom master equation

We consider a single atom, static at the origin, subject to a classical driving laser field and also interacting with the external quantised radiation field. As derived in the last chapter the Hamiltonian of this system is given by Eq. (2.12). Before we attempt to solve this full Hamiltonian let us first look at the effect of the radiation field that acts as a bath in this open quantum system. Coupling to the bath modes gives rise to spontaneous emission, which disrupts the coherent dynamics of the atomic system. We discuss the issue of spontaneous emission in the following using the Wigner-Weisskopf treatment [90].

3.1.1 Spontaneous decay rate

Here we consider a static atom at the origin. The atom is taken as a two level system where the ground state $|g\rangle$ and one particular excited state $|e\rangle$ are considered. Populations in all the other excited states is neglected. With the energy difference between the two states ω_{eg}, the Hamiltonian is

$$H = \hbar\omega_{eg}|e\rangle\langle e| - \sum_{\boldsymbol{k},\lambda}\left(\xi_{\boldsymbol{k},\lambda}|e\rangle\langle g|b_{\boldsymbol{k},\lambda} + \xi^*_{\boldsymbol{k},\lambda}|g\rangle\langle e|b^\dagger_{\boldsymbol{k},\lambda}\right) + \sum_{\boldsymbol{k},\lambda}\hbar\omega_k b^\dagger_{\boldsymbol{k},\lambda}b_{\boldsymbol{k},\lambda}\,, \tag{3.1}$$

where, as in the last chapter, the quantum mechanical electric field operator is defined in terms of a discrete mode expansion with unit polarisation vector $\boldsymbol{\epsilon}_\lambda$ and angular frequency ω_k in a quantisation volume V, giving rise to the dipole coupling strength,

$$\xi_{\boldsymbol{k},\lambda} = i\sqrt{\frac{\hbar\omega_k}{2\epsilon_0 V}}\langle e|\mathbf{d}\cdot\boldsymbol{\epsilon}_\lambda|g\rangle\,. \tag{3.2}$$

We also have not kept the interaction terms that give rise to rapidly oscillating terms and therefore can be neglected under the rotating wave approximation. Initially we take the atom to be in the excited state and the field to be in the vacuum state, without any photons present. The wavefunction at $t = 0$ therefore is $|\psi(t = 0)\rangle = |e\rangle \otimes |\text{vac}\rangle$. At a later time the atom has finite probability of descending to the ground state by spontaneous decay, which generates a photon mode. This means,

$$|\psi(t)\rangle = c_e(t)e^{-i\omega_{eg}t}|e\rangle \otimes |\text{vac}\rangle + \sum_{\boldsymbol{k},\lambda} c_{\boldsymbol{k},\lambda}(t)e^{-i\omega_k t}|g\rangle \otimes b^\dagger_{\boldsymbol{k},\lambda}|\text{vac}\rangle\,, \tag{3.3}$$

where c_e and $c_{\boldsymbol{k},\lambda}$ are the respective probability amplitudes of no photon emission and one photon emission in $(\boldsymbol{k},\lambda)$ mode in time between 0 and t. Using the Schrödinger equation we can write the coupled equations for the probability amplitudes,

$$\dot{c}_e(t) = -\sum_{\boldsymbol{k},\lambda} \left|\frac{\xi_{\boldsymbol{k},\lambda}}{\hbar}\right|^2 \int_0^t dt' e^{-i(\omega_k-\omega_{eg})(t-t')} c_e(t') \,. \tag{3.4}$$

Now going to the continuum limit where we take $V \to \infty$ and using spherical coordinates in $\boldsymbol{k}$-space with the axis along the dipole vector $\boldsymbol{d}_{e,g} = \langle e|\mathbf{d}|g\rangle$ we arrive at

$$\dot{c}_e(t) = -\frac{|\boldsymbol{d}_{e,g}|^2}{6\pi^2\epsilon_0\hbar c^3} \int_0^\infty d\omega_k \omega_k^3 \int_0^t dt' e^{-i(\omega_k-\omega_{eg})(t-t')} c_e(t') \,. \tag{3.5}$$

The treatment so far has been exact. Now we apply the Wigner-Weisskopf approximation where the coefficient $c_e(t)$ is taken to be slowly varying in time. Due to the presence of the rapidly oscillating term in the time integral, the dominant contribution only comes from the region $t' \approx t$. We can therefore evaluate $c_e(t')$ only at time t and take it out of the integral. This is essentially treating the atomic decay as a Markov process where the dynamics of $c_e(t)$ only depends on the current time and not on the past. As $t' \approx t$ is the only relevant region the upper limit in the time integral can be taken to be infinity. Analytical integration can now be carried out resulting in,

$$\dot{c}_e(t) = -\left(-i\Delta\omega_L + \frac{\Gamma}{2}\right) c_e(t) \,. \tag{3.6}$$

Here the frequency shift, which is defined through Cauchy principal value,

$$\Delta\omega_L = \frac{1}{4\pi\epsilon_0}\frac{|\boldsymbol{d}_{e,g}|^2}{3\pi\hbar c^3} \mathcal{P}\left(\int_0^\infty d\omega_k \frac{\omega_k^3}{\omega_k - \omega_{eg}}\right) \,, \tag{3.7}$$

is a contribution to the Lamb shift [91]. Due to the diverging nature of the integral a cutoff frequency is usually introduced which enables one to carry out the integration and renormalise the atomic transition frequency by absorbing this relatively small shift. The spontaneous decay rate, on the other hand, is defined as,

$$\Gamma = \frac{|\boldsymbol{d}_{e,g}|^2 \omega_{eg}^3}{3\pi\hbar\epsilon_0 c^3}\,, \tag{3.8}$$

which is also known as the Einstein A coefficient. Note that this decay rate can also be deduced for short times in time-dependent perturbation theory which leads to Fermi's golden rule [92]. In the presence of a driving laser field the atom can be re-excited following a spontaneous decay. We will now look at this problem with multiple photon emission events in the master equation formalism where the dynamics of system density operator are governed by optical Bloch equations.

3.1.2 Optical Bloch equations

The Hamiltonian for a laser-driven atom static at the origin and interacting with external radiation field, as discussed in the last chapter, consists of three terms, $H = H_{\text{sys}} + H_{\text{int}} + H_{\text{Field}}$. Here, H_{sys} describes the combined system of the atom driven by the classical laser field, and therefore,

$$H_{\text{sys}} = \hbar\omega_{eg}|e\rangle\langle e| - \sigma_+ \boldsymbol{d}_{e,g} \cdot \boldsymbol{E}^+_{\text{cl}}(0,t) - \boldsymbol{d}_{e,g} \cdot \boldsymbol{E}^-_{\text{cl}}(0,t)\sigma_-\,, \tag{3.9}$$

where the classical driving field $\boldsymbol{E}^+_{\text{cl}}(0,t) = \boldsymbol{\epsilon} E_0(t) e^{-i\omega_L t}$. The Hamiltonian for external radiation field is described by,

$$H_{\text{Field}} = \sum_{\boldsymbol{k},\lambda} \hbar\omega_k b^\dagger_{\boldsymbol{k},\lambda} b_{\boldsymbol{k},\lambda}\,. \tag{3.10}$$

The interaction between the atom and the radiation field is described by,

$$H_{\text{int}} = -\sigma_+ \boldsymbol{d}_{e,g} \cdot \boldsymbol{E}^+(0) - \boldsymbol{d}_{e,g} \cdot \boldsymbol{E}^-(0)\sigma_-\,, \tag{3.11}$$

where the electric field operator, in the continuum limit where we would integrate in $\boldsymbol{k}$-space, is,

$$\boldsymbol{E}^{+}(\boldsymbol{r}) = i\sum_{\lambda}\int d^3k\sqrt{\frac{\hbar\omega_k}{2\epsilon_0(2\pi)^3}}b_{\boldsymbol{k},\lambda}e^{i\boldsymbol{k}\cdot\boldsymbol{r}}\boldsymbol{\epsilon}_{\boldsymbol{k},\lambda}\,. \tag{3.12}$$

In this Hamiltonian we have again used the rotating wave approximation and therefore the energetically non-conserving terms are absent.

Now in the Heisenberg picture the field mode operators obey,

$$\dot{b}_{\boldsymbol{k},\lambda}(t) = -i\omega_k b_{\boldsymbol{k},\lambda}(t) + \boldsymbol{d}_{e,g}\cdot\boldsymbol{\epsilon}_{\boldsymbol{k},\lambda}\sqrt{\frac{\omega_k}{2\hbar\epsilon_0(2\pi)^3}}\sigma_-(t)\,, \tag{3.13}$$

which leads to

$$b_{\boldsymbol{k},\lambda}(t) = b_{\boldsymbol{k},\lambda}(0)e^{-i\omega_k t} + \boldsymbol{d}_{e,g}\cdot\boldsymbol{\epsilon}_{\boldsymbol{k},\lambda}\sqrt{\frac{\omega_k}{2\hbar\epsilon_0(2\pi)^3}}\int_0^t dt' e^{-i\omega_k(t-t')}\sigma_-(t')\,. \tag{3.14}$$

Here in the second term the atomic operator $\sigma_-(t)$ works as a source term. Without this source term, the free *input field* is generated by the first term, which is,

$$\boldsymbol{E}^{+}_{\text{in}}(0,t) = i\sum_{\lambda}\int d^3k\sqrt{\hbar\omega_k/2\epsilon_0(2\pi)^3}b_{\boldsymbol{k},\lambda}(0)e^{-i\omega_k t}\boldsymbol{\epsilon}_{\boldsymbol{k},\lambda}\,. \tag{3.15}$$

Now for the terms in H_{int} the following expression can be used,

$$\begin{aligned}-\boldsymbol{d}_{e,g}\cdot\boldsymbol{E}^{+}(0,t) &= -\boldsymbol{d}_{e,g}\cdot\boldsymbol{E}^{+}_{\text{in}}(0,t)\\ &\quad -\frac{i}{\hbar}\sum_{\lambda}\int d^3k\frac{\hbar\omega_k}{2\epsilon_0(2\pi)^3}|\boldsymbol{d}_{e,g}\cdot\boldsymbol{\epsilon}_{\boldsymbol{k},\lambda}|^2\int_0^t dt' e^{-i\omega_k(t-t')}\sigma_-(t')\,.\end{aligned} \tag{3.16}$$

In order to simplify this expression, a standard set of approximations needs to be applied here. The first one is the Born approximation [93] where the interaction coupling strength is taken to be much weaker than the energy scales of both the system and the environment, which in this case is given by the optical frequencies. This enables us to neglect the deviation from an uncorrelated state of the system and bath, where the total density operator can always be written as a product of their respective density operator when the initial state was also factorable. In our case the initial state is taken to be $|g\rangle \otimes |\text{vac}\rangle$. Moreover, the bath being much larger, we can also assume it to be practically unaffected by the weak coupling and therefore the bath density operator to remain unchanged. The next major approximation is the Markov approximation [93], where the statistical bath parameters are assumed to rapidly return to their equilibrium value following any possible changes due to interaction with the system. The bath correlation times, set by the optical time scales, are much shorter than the relevant time steps needed to integrate for the system dynamics, depending on the Rabi frequency, detuning and spontaneous decay rate, all of which are much shorter than the optical frequencies. Therefore the current knowledge of the system density operator is sufficient to determine the future behaviour. In the Born-Markov approximation we can take $\sigma_-(t') \to \sigma_-(t)e^{i\omega_{eg}(t-t')}$ which, along with the similar treatment that was carried out in the last subsection lead to the following simplification, with an expected introduction of a Lamb shift,

$$-\boldsymbol{d}_{e,g}\cdot\boldsymbol{E}^+(0,t) = -\boldsymbol{d}_{e,g}\cdot\boldsymbol{E}^+_{\text{in}}(0,t) - i\hbar\left(-i\Delta\omega_L + \frac{\Gamma}{2}\right)\sigma_-(t)\,. \tag{3.17}$$

We can now write down the quantum Langevin equation which is the Heisenberg equation for the atomic operator,

$$\begin{aligned}\dot{a}(t) = \frac{i}{\hbar}\left[H_{\text{sys}}, a(t)\right] + \frac{i}{\hbar}\left[\sigma_+(t), a(t)\right]\left(-\boldsymbol{d}_{e,g}\cdot\boldsymbol{E}^+_{\text{in}}(0,t) - \hbar\Delta\omega_L\sigma_-(t) - i\hbar\frac{\Gamma}{2}\sigma_-(t)\right)\\ + \frac{i}{\hbar}\left(-\boldsymbol{d}_{e,g}\cdot\boldsymbol{E}^-_{\text{in}}(0,t) - \hbar\Delta\omega_L\sigma_+(t) + i\hbar\frac{\Gamma}{2}\sigma_+(t)\right)\left[\sigma_-(t), a(t)\right]\\ = \frac{i}{\hbar}\left[H_{\text{sys}}, a(t)\right] + \Gamma\left(\sigma_+(t)a(t)\sigma_-(t) - \frac{1}{2}a(t)\sigma_+(t)\sigma_-(t) - \frac{1}{2}\sigma_+(t)\sigma_-(t)a(t)\right)\\ - \frac{i}{\hbar}\left[\sigma_+(t), a(t)\right]\big(\boldsymbol{d}_{e,g}\cdot\boldsymbol{E}^+_{\text{in}}(0,t)\big) - \frac{i}{\hbar}\big(\boldsymbol{d}_{e,g}\cdot\boldsymbol{E}^-_{\text{in}}(0,t)\big)\left[\sigma_-(t), a(t)\right]\,,\end{aligned} \tag{3.18}$$

where in the second line the Lamb shift has been absorbed in the redefinition of the atomic transition frequency. Now to write down the equivalent master equation we move from the Heisenberg picture to the optical Bloch equations for the atomic density operator $\rho(t)$ (obtained from the total density operator ρ_{tot}

by tracing over the field) in the Schrödinger picture,

$$\begin{aligned}
&\mathrm{Tr}_{\mathrm{sys}}\left(a\dot{\rho}(t)\right)\\
=&\langle \dot{a}(t)\rangle\\
=&\mathrm{Tr}_{\mathrm{sys}\oplus\mathrm{Field}}\Bigg\{\Bigg(\frac{i}{\hbar}\left[H_{\mathrm{sys}}, a(t)\right]\\
&+\Gamma\left(\sigma_+(t)a(t)\sigma_-(t)-\frac{1}{2}a(t)\sigma_+(t)\sigma_-(t)-\frac{1}{2}\sigma_+(t)\sigma_-(t)a(t)\right)\\
&-\frac{i}{\hbar}\left[\sigma_+(t), a(t)\right]\left(\boldsymbol{d}_{e,g}\cdot\boldsymbol{E}^{+}_{\mathrm{in}}(0,t)\right)-\frac{i}{\hbar}\left(\boldsymbol{d}_{e,g}\cdot\boldsymbol{E}^{-}_{\mathrm{in}}(0,t)\right)\left[\sigma_-(t), a(t)\right]\Bigg)\rho_{\mathrm{tot}}(0)\Bigg\}\\
=&\mathrm{Tr}_{\mathrm{sys}}\Bigg\{a\Bigg(-\frac{i}{\hbar}\left[H_{\mathrm{sys}}+\beta^*(t)\sigma_- - \beta(t)\sigma_+, \rho(t)\right]\\
&+\Gamma\left(\sigma_-\rho(t)\sigma_+ -\frac{1}{2}\rho(t)\sigma_+\sigma_- -\frac{1}{2}\sigma_+\sigma_-\rho(t)\right)\Bigg)\Bigg\},
\end{aligned} \tag{3.19}$$

where $\beta(t)\rho(0)=\boldsymbol{d}_{e,g}\cdot\boldsymbol{E}^{+}_{\mathrm{in}}(0,t)\rho(0)$. Unitarity of the time evolution operator and invariance of trace under cyclic permutations have been used to arrive at the last line. As mentioned before, we take the initial state as $|g\rangle\otimes|\mathrm{vac}\rangle$, which means $\beta=0$, and we get the following master equation,

$$\dot{\rho}(t)=-\frac{i}{\hbar}\left[H_{\mathrm{sys}}, \rho(t)\right]+\Gamma\left(\sigma_-\rho(t)\sigma_+ -\frac{1}{2}\rho(t)\sigma_+\sigma_- -\frac{1}{2}\sigma_+\sigma_-\rho(t)\right). \tag{3.20}$$

The first part in the master equation corresponds to the coherent dynamics and the dissipative dynamics due to the spontaneous emission is described by the second part. After a transformation to the rotating frame with $\tilde{\rho}=e^{i\omega_L t}\rho e^{-i\omega_L t}$, this master equation can be alternatively written as

$$\dot{\tilde{\rho}}(t)=-\frac{i}{\hbar}\left(H_{\mathrm{eff}}\tilde{\rho(t)}-\tilde{\rho(t)}H^{\dagger}_{\mathrm{eff}}\right)+\Gamma\sigma_-\tilde{\rho(t)}\sigma_+\,. \tag{3.21}$$

The non-Hermitian effective Hamiltonian is defined as

$$H_{\mathrm{eff}}=\hbar\left(-\Delta-i\frac{\Gamma}{2}\right)|e\rangle\langle e|-\frac{\hbar\Omega(t)}{2}\sigma_+-\frac{\hbar\Omega^*(t)}{2}\sigma_-\,, \tag{3.22}$$

with detuning Δ and Rabi frequency Ω as discussed in the previous chapter. We now go on to the subject of deriving the master equation for a many-atom system.

3.2 Many-body master equation without motion

The generalisation to the derivation of the master equation for many atoms with fixed positions is quite straightforward and the result displays different aspects of many-body physics [94]. In this case for identical two level atoms, the components of the total Hamiltonian are,

$$\begin{aligned} H_{\text{sys}} &= \sum_i \left(\hbar\omega_{eg} |e\rangle_i \langle e| - \sigma_i^+ \boldsymbol{d}_{e,g} \cdot \boldsymbol{E}_{\text{cl}}^+(\boldsymbol{r}_i, t) - \boldsymbol{d}_{e,g} \cdot \boldsymbol{E}_{\text{cl}}^-(\boldsymbol{r}_i, t)\sigma_i^- \right) \qquad (3.23) \\ H_{\text{int}} &= \sum_i \left(-\sigma_i^+ \boldsymbol{d}_{e,g} \cdot \boldsymbol{E}^+(\boldsymbol{r}_i) - \boldsymbol{d}_{e,g} \cdot \boldsymbol{E}^-(\boldsymbol{r}_i)\sigma_i^- \right) \qquad (3.24) \\ H_{\text{Field}} &= \sum_\lambda \int d^3k \hbar\omega_k b_{\boldsymbol{k},\lambda}^\dagger b_{\boldsymbol{k},\lambda} \,. \qquad (3.25) \end{aligned}$$

For the coupling terms in the interaction Hamiltonian for the many-body case we write the expression as,

$$\begin{aligned} -\boldsymbol{d}_{e,g} \cdot \boldsymbol{E}^+(\boldsymbol{r}, t) &= -\boldsymbol{d}_{e,g} \cdot \boldsymbol{E}_{\text{in}}^+(\boldsymbol{r}, t) \\ &\quad - \frac{i}{\hbar} \sum_\lambda \int d^3k \frac{\hbar\omega_k}{2\epsilon_0 (2\pi)^3} |\boldsymbol{d}_{e,g} \cdot \boldsymbol{\epsilon}_{\boldsymbol{k},\lambda}|^2 \int_0^t dt' e^{-i\omega_k (t-t')} \sum_i e^{i\boldsymbol{k}\cdot(\boldsymbol{r}-\boldsymbol{r}_i)} \sigma_i^-(t') \,. \end{aligned} \qquad (3.26)$$

The quantum Langevin equation in this case also takes a form that is similar to the previous single atom case. The effect of the many-body physics is explicitly displayed by the presence of photon mediated dipole-dipole interaction terms and spontaneous emission events that can connect two separate atoms. After absorbing the Lamb shifts in the redefinition of the atomic transition frequencies we obtain,

$$\begin{aligned}\dot{a}(t) = \frac{i}{\hbar}&\left[H_{\text{sys}} + \hbar\Gamma\sum_{i\neq j} G_{ij}\sigma_i^+(t)\sigma_j^-(t), a(t)\right]\\ &+\Gamma\sum_{i,j}F_{ij}\left(\sigma_i^+(t)a(t)\sigma_j^-(t) - \frac{1}{2}a(t)\sigma_i^+(t)\sigma_j^-(t) - \frac{1}{2}\sigma_i^+(t)\sigma_j^-(t)a(t)\right)\\ &-\frac{i}{\hbar}\sum_i\left[\sigma_i^+(t), a(t)\right]\left(\boldsymbol{d}_{e,g}\cdot\boldsymbol{E}_{\text{in}}^+(\boldsymbol{r}_i,t)\right) - \frac{i}{\hbar}\sum_i\left(\boldsymbol{d}_{e,g}\cdot\boldsymbol{E}_{\text{in}}^-(\boldsymbol{r}_i,t)\right)\left[\sigma_i^-(t), a(t)\right]\ ,\end{aligned} \tag{3.27}$$

with F and G defined as a function of the scaled separations $\boldsymbol{\xi}_{ij} = \omega_{eg}(\boldsymbol{r}_i - \boldsymbol{r}_j)/c$,

$$F_{ij} = \frac{3}{2}\left\{[1 - (\hat{\boldsymbol{\xi}}_{ij}\cdot\hat{\boldsymbol{d}}_{eg})^2]\frac{\sin\xi_{ij}}{\xi_{ij}} + [1 - 3(\hat{\boldsymbol{\xi}}_{ij}\cdot\hat{\boldsymbol{d}}_{eg})^2]\left(\frac{\cos\xi_{ij}}{\xi_{ij}^2} - \frac{\sin\xi_{ij}}{\xi_{ij}^3}\right)\right\} \tag{3.28}$$

$$G_{ij} = \frac{3}{4}\left\{-[1 - (\hat{\boldsymbol{\xi}}_{ij}\cdot\hat{\boldsymbol{d}}_{eg})^2]\frac{\cos\xi_{ij}}{\xi_{ij}} + [1 - 3(\hat{\boldsymbol{\xi}}_{ij}\cdot\hat{\boldsymbol{d}}_{eg})^2]\left(\frac{\sin\xi_{ij}}{\xi_{ij}^2} + \frac{\cos\xi_{ij}}{\xi_{ij}^3}\right)\right\}\ . \tag{3.29}$$

The master equation now can be written as,

$$\begin{aligned}\dot{\rho}(t) = -\frac{i}{\hbar}&\left[H_{\text{sys}} + \hbar\Gamma\sum_{i\neq j} G_{ij}\sigma_i^+\sigma_j^-, \rho(t)\right]\\ &+\Gamma\sum_{i,j}F_{ij}\left(\sigma_i^-\rho(t)\sigma_j^+ - \frac{1}{2}\rho(t)\sigma_i^+\sigma_j^- - \frac{1}{2}\sigma_i^+\sigma_j^-\rho(t)\right)\ .\end{aligned} \tag{3.30}$$

The dipole-dipole interaction strength, given by G_{ij}, falls off in an oscillatory way with the distance $|\boldsymbol{r}_i - \boldsymbol{r}_j|$ on a length scale of the wavelength of the emitted photon, and at short distances approaches the static $\sim 1/r^3$ dipole-dipole behaviour. The F function also falls off in a similar fashion and we will discuss in chapter 5 the details of the effects of this term in the dissipative part of the master equation, which is responsible for the very interesting behaviour of collective radiation, giving rise to superradiance and subradiance. For now we move on to the topic of the master equation for many atoms when they are allowed to move.

3.3 Many-body master equation with motion

In this section we will only outline the derivation of the many-body master equation that includes atomic motion for the bosonic case as was done in Ref. [65]. In chapter 5 we will present a detailed derivation of the master equation for fermions, starting from a microscopic picture based on the atomic structure of the experimentally relevant atomic species.

Before we indulge in the discussion of many-body master equation formalism for bosons, a brief overview of the case of a single atom with motion is presented to provide a useful insight. For this we consider the system Hamiltonian again for a laser-driven atom that is allowed to move,

$$H_{\mathrm{sys}} = \frac{\mathbf{p}^2}{2m} + \hbar\omega_{eg}|e\rangle\langle e| - \sigma_+ \boldsymbol{d}_{e,g} \cdot \boldsymbol{E}^{+}_{\mathrm{cl}}(0,t) - \boldsymbol{d}_{e,g} \cdot \boldsymbol{E}^{-}_{\mathrm{cl}}(0,t)\sigma_- \, . \tag{3.31}$$

In this case a spontaneous emission of a photon along the direction $\mathbf{u}$ results in a momentum kick. The jump operator corresponding to the transition and momentum recoil is given by $c_{\mathbf{u}} = e^{-ik_{eg}\mathbf{u}\cdot\mathbf{r}}|g\rangle\langle e|$ with k_{eg} as the wavenumber corresponding to the atomic transition frequency. The master equation for the atomic density operator, under the standard approximations as the previous cases, has the following form (see, for example, [65, 95]),

$$\dot{\rho}(t) = -\frac{i}{\hbar}\left[H_{\mathrm{sys}}, \rho(t)\right] + \Gamma \int d\mathbf{u} N(\mathbf{u}) \left(c_{\mathbf{u}}\rho(t)c^{\dagger}_{\mathbf{u}} - \frac{1}{2}c^{\dagger}_{\mathbf{u}}c_{\mathbf{u}}\rho(t) - \frac{1}{2}\rho(t)c^{\dagger}_{\mathbf{u}}c_{\mathbf{u}} \right) , \tag{3.32}$$

where the distribution function for the spontaneously emitted photons is given by $N(\mathbf{u}) = 3[1-(\hat{\boldsymbol{d}}_{e,g}\cdot\mathbf{u})^2]/8\pi$. In the case of a far-detuned lattice ($\Delta \gg \Omega, \Gamma$, kinetic energy) one can systematically perform *adiabatic elimination* of the population in the excited state and write the effective equation of motion for the ground state only,

$$\dot{\rho}_{gg} = -\frac{i}{\hbar}\left[\frac{\mathbf{p}^2}{2m} + \frac{|\Omega(\boldsymbol{r})|^2}{4\Delta}, \rho_{gg}\right] + \Gamma\left(\int d\mathbf{u} N(\mathbf{u}) \tilde{c}_{\mathbf{u}}\rho_{gg}\tilde{c}^{\dagger}_{\mathbf{u}} - \frac{1}{2}\tilde{c}^{\dagger}_{\mathbf{u}}\tilde{c}_{\mathbf{u}}\rho_{gg} - \frac{1}{2}\rho_{gg}\tilde{c}^{\dagger}_{\mathbf{u}}\tilde{c}_{\mathbf{u}} \right) . \tag{3.33}$$

Here the optical potential ($|\Omega(\boldsymbol{r})|^2/4\Delta$) in the coherent evolution section comes from the AC-Stark shift of the two-level atom. The modified jump operator $\tilde{c}_{\mathbf{u}} = e^{-ik_{eg}\mathbf{u}\cdot\mathbf{r}}\Omega(\boldsymbol{r})/2\Delta$ is now associated with an absorption of a laser photon followed by a spontaneous emission along $\mathbf{u}$, resulting in a momentum recoil. An effective spontaneous emission rate is given by the combined operators in the following way, $\Gamma_{\text{eff}} = \Gamma\tilde{c}^\dagger_{\mathbf{u}}\tilde{c}_{\mathbf{u}} = \Gamma(|\Omega(\boldsymbol{r})|^2/4\Delta^2)$.

A generalisation of the procedure described above for many bosons was carried out in Ref. [65]. In that work a two-level bosonic atom is described in second quantisation by the field operators ψ_g and ψ_e, obeying bosonic commutation relations. At the starting point one can neglect the inter-atomic interaction described by the short-range physics. Now the master equation can be obtained in a similar way as was described in the last section, using the Born-Markov approximation and the rotating wave approximation. As before the master equation contains a coherent part and a dissipative part, given by $\mathcal{L}\rho$ [65],

$$\dot{\rho}(t) = -\frac{i}{\hbar}\left[H_{\text{sys}} + H_{\text{dipole}}, \rho(t)\right] + \mathcal{L}\rho(t)\,. \tag{3.34}$$

The atomic motion and atomic structure is included in the system Hamiltonian H_{sys}. The dipole-dipole interaction part is given by H_{dipole}. In the limit of large detuning (i.e. detuning is much larger than the other atomic energy scales, like Rabi frequency, spontaneous decay rate etc.), one can neglect the population in the excited state as the atom is essentially always in the ground state. In a perturbative approach the atomic structure in H_{sys} therefore can be eliminated and the AC Stark shift for the ground state is included which gives the optical lattice potential. As the strength of the dipole-dipole interaction falls off rapidly for bosons on different lattice sites the off-site interaction can be neglected. The on-site dipole-dipole interaction can be absorbed as a small correction to the short-range collisional interaction, which in experimental situations is parameterised by the s-wave scattering length in the low energy limit.

The dissipative term $\mathcal{L}\rho$ describes the different processes arising from the single-atom photon emission following an absorption, a collective two-atom process of absorption and emission, and also a recycling term that is modulated by the F

function as discussed in the last section. The localising effect of a spontaneous emission event is due to the presence of this term containing the F function, on a length-scale set by the wavelength of the emitted photon. Now in the periodic optical lattice potential it is possible to expand the ground state field operators in terms of Wannier functions which leads to a description of the coherent dynamics of the bosons by a multi-band Bose-Hubbard Hamiltonian. In the experiments it is often relevant to work in lattices deep enough so that it suffices to take only the lowest band into account. In this case the master equation takes a simpler form in terms of a single band Bose-Hubbard Hamiltonian H_{BH} and number operators at each site n_i are the dissipative operators. This Lindblad form of the master equation is:

$$\dot{\rho} = -\frac{i}{\hbar}[H_{BH}, \rho] + \gamma \sum_i \left(n_i \rho n_i - \frac{1}{2} n_i n_i \rho - \frac{1}{2} \rho n_i n_i \right) . \tag{3.35}$$

In an event of spontaneous emission the action of a local particle number operator n_i at a particular site i on a coherent wavefunction $|\psi_0\rangle$ can be thought of a *quantum jump* causing onsite localisation:

$$|\psi_0\rangle \to \frac{n_i|\psi_0\rangle}{||n_i|\psi_0\rangle||} . \tag{3.36}$$

The initial occupations for a single atom at different sites in the coherent state prior to the spontaneous emission determine the probabilities of it being localised at different sites, which results in a mixed state with unchanged occupations.

We now conclude this chapter where an overview of a stepwise derivation of a many-body master equation is presented for cold atoms in optical lattices in the presence of spontaneous emission as the source of decoherence, due to coupling to the quantised vacuum modes of radiation. The numerical techniques to deal with such many-body systems, with and without decoherence, will be discussed in the next chapter.

Chapter 4

Numerical techniques

4.1 Introduction

As a method to simulate quantum many-body systems, exact diagonalisation of the Hamiltonian on the full Hilbert space fails beyond a very small system size. This is due to the exponential growth of the Hilbert space size with the system size and therefore our inability to store the state of the system and operate on the state on a classical computer. For instance, for a two-species Fermi-Hubbard model at half-filling with M sites and $M/2$ number of fermions from each species, the size of the total Hilbert space is $({}^{M}C_{M/2})^2$ (assuming even M). Even for a 50 site lattice this number is around 10^{28}. Storing this state with double precision numbers will therefore require around 10^{14} PB of memory which is far beyond the largest computational storage capacity even in the foreseeable future. Furthermore to compute a single time evolution step on this state would require multiplication by a matrix of which the number of elements is the square of the Hilbert space size. The number of basic floating point operations (FLOPs) for the time step is of the order of 10^{56} which, even with the fastest supercomputers of present time, would take a time much longer than the age of the universe. The only way to numerically simulate these systems is therefore to use justified approximations. In this chapter we present the well established approximate methods used to numerically compute the ground state of systems of ultracold atoms on one dimensional optical lattices and also simulate the time evolution of these systems in the presence of sources that cause decoherence. In Sec. 4.2 we describe the Density Matrix Renormalisation Group (DMRG) methods, focussing on the Time Evolving Block Decimation (TEBD) algorithm that we use to carry out time evolution (Reviews [96, 97]). In Sec.4.3 we review the quantum trajectory algorithm (Review [73]) which is used in combination with TEBD methods to tackle the time evolution of open quantum systems.

4.2 TEBD algorithm

DMRG techniques, introduced in 1992 by Steven White, enable us to calculate the ground state of a wide class of large 1D systems up to a very high precision [67, 68]. This method overcomes the difficulty of dealing with an exponentially large Hilbert space by retaining only a computationally tractable fraction of states that does not change the representation of the state of the system significantly. Extension of this central idea of DMRG for time evolving problems was attempted in 2002 by M. Cazalilla [98]. The major breakthrough however came in 2003 with G. Vidal developing the TEBD algorithm [69, 70]. Unlike the static decimation of the Hilbert space performed by the DMRG algorithm, this method adaptively truncates the Hilbert space during time evolution. The relation between DMRG and TEBD methods was established in 2004 in two articles [99, 100], enabling optimisation of the TEBD method by implementing conservation laws from DMRG language. In this thesis we have primarily worked with the TEBD algorithm for ground state search and time evolution of quantum many-body states of systems where the number of particles were conserved. An overview of various aspects of the TEBD algorithm is presented in this section.

4.2.1 Schmidt decomposition

The goal of the TEBD method is to compute the time evolution of a many-body quantum system that can be written as a product of M local Hilbert spaces, i.e. the state,

$$|\psi\rangle = \sum_{i_1,i_2,...,i_M=1}^{d} c_{i_1,i_2,...,i_M} |i_1, i_2, ..., i_M\rangle \,, \tag{4.1}$$

where i_k are the basis for subsystem k. The dimension of the space, $\dim(H) = d^M$ as we have taken, for simplicity, a uniform local dimension d. The Schmidt decomposition is then needed to represent this state as a series of tensors which is the basis of TEBD algorithm.

A bipartite quantum state comprising of two subsystems A and B, with dimensions d_A and d_B respectively, can be very generally written as

$$|\psi_{AB}\rangle = \sum_{i=1}^{d_A} \sum_{j=1}^{d_B} c_{i,j} |i\rangle_A \otimes |j\rangle_B \,. \tag{4.2}$$

Using the singular value decomposition (SVD) of matrices in linear algebra, the coefficient matrix $c_{i,j}$ matrix can be decomposed into

$$c_{i,j} = \sum_{a=1}^{\chi_{AB}} U_{i,a} S_{a,a} V_{a,j} \,, \tag{4.3}$$

where U and V are unitary matrices of sizes $d_A \times d_A$ and $d_B \times d_B$ respectively, S is a $d_A \times d_B$ diagonal matrix with non-negative entries known as *singular values*, and χ_{AB} is the number of such non-zero entries. Denoting $\lambda_a \equiv S_{a,a}$ we can rewrite the state as a Schmidt decomposition,

$$|\psi_{AB}\rangle = \sum_{a=1}^{\chi_{AB}} \lambda_a |\phi_a^A\rangle \otimes |\phi_a^B\rangle \,, \tag{4.4}$$

where the Schmidt vectors

$$|\phi_a^A\rangle = \sum_i U_{i,a}|i\rangle_A\,, \tag{4.5}$$

$$|\phi_a^B\rangle = \sum_j V_{a,j}|j\rangle_B\,, \tag{4.6}$$

form orthonormal bases in the two subsystems A and B respectively, due to the unitarity of U and V. Here χ_{AB} is known as the *Schmidt rank* of this bipartite system. It is bounded from above by $\min(d_A, d_B)$. Also, λ_a are known as *Schmidt coefficients* and they satisfy the normalisation condition

$$\sum_a \lambda_a^2 = 1\,. \tag{4.7}$$

4.2.2 State representation

At the starting point of the application of TEBD method we write the coefficients in Eq. (4.1) as a product of M tensors and $M-1$ vectors:

$$c_{i_1,i_2,\dots,i_M} = \sum_{a_1}^{\chi_1}\sum_{a_2}^{\chi_2}\dots\sum_{a_{M-1}}^{\chi_{M-1}} \Gamma^{[1]i_1}_{a_1}\lambda^{[1]}_{a_1}\Gamma^{[2]i_2}_{a_1a_2}\dots\Gamma^{[M]i_M}_{a_{M-1}}\,, \tag{4.8}$$

where the Γ tensors and the λ vectors are constructed in such a way that when a Schmidt decomposition is performed at the l-th bond i.e. between the l-th and $(l+1)$-th site, one gets $\lambda^{[l]}_{a_l}$ as the Schmidt coefficients of that bipartite splitting. The orthonormal sets of eigenvectors also turn out to be

$$|\phi^{[1\dots l]}_{a_l}\rangle = \sum_{i_1,i_2,\dots,i_l}^{d}\sum_{a_1}^{\chi_1}\sum_{a_2}^{\chi_2}\dots\sum_{a_{l-1}}^{\chi_{l-1}}\Gamma^{[1]i_1}_{a_1}\lambda^{[1]}_{a_1}\Gamma^{[2]i_2}_{a_1a_2}\dots\Gamma^{[l]i_l}_{a_{l-1}a_l}|i_1,i_2,\dots,i_l\rangle\,, \tag{4.9}$$

and

$$
\begin{aligned}
&|\phi_{a_l}^{[l+1...M]}\rangle \\
&= \sum_{i_{l+1},i_{l+2},...,i_M}^{d} \sum_{a_{l+1}}^{\chi_{l+1}} \sum_{a_{l+2}}^{\chi_{l+2}} ... \sum_{a_{M-1}}^{\chi_{M-1}} \Gamma_{a_l a_{l+1}}^{[l+1]i_{l+1}} \lambda_{a_{l+1}}^{[l+1]} \Gamma_{a_{l+1}a_{l+2}}^{[l+2]i_{l+2}} ... \Gamma_{a_{M-1}}^{[M]i_M} |i_{l+1}, i_{l+2}, ..., i_M\rangle \,,
\end{aligned}
\tag{4.10}
$$

so that one can write the state as:

$$
|\psi\rangle = \sum_{a_l}^{\chi_l} \lambda_{a_l}^{[l]} |\phi_{a_l}^{[1...l]}\rangle \otimes |\phi_{a_l}^{[l+1...M]}\rangle \,. \tag{4.11}
$$

This particular form of state representation is achieved by iterative Schmidt decompositions. We start at bond 1:

$$
|\psi\rangle = \sum_{a_1}^{\chi_1} \lambda_{a_1}^{[1]} |\phi_{a_1}^{[1]}\rangle \otimes |\phi_{a_1}^{[2...M]}\rangle \,. \tag{4.12}
$$

The Schmidt vectors $\left\{|\phi_{a_1}^{[1]}\rangle\right\}$ can be written as a superposition of local basis states $\{|i_1\rangle\}$,

$$
|\phi_{a_1}^{[1]}\rangle = \sum_{i_1}^{d} \Gamma_{a_1}^{[1]i_1} |i_1\rangle \,. \tag{4.13}
$$

For the other set of Schmidt vectors $\left\{|\phi_{a_1}^{[2...M]}\rangle\right\}$, the local basis states $\{|i_2\rangle\}$ can be factored out,

$$
|\phi_{a_1}^{[2...M]}\rangle = \sum_{i_2}^{d} |i_2\rangle \otimes |j_{a_1,i_2}^{[3...M]}\rangle \,, \tag{4.14}
$$

where $\left\{|j_{a_1,i_2}^{[3...M]}\rangle\right\}$ are unnormalised states, in general. They can be expanded as a superposition of the Schmidt vectors on the sites that are to the right of site 2, obtained by a Schmidt decomposition at bond 2, i.e.

$$|j^{[3\dots M]}_{a_1,i_2}\rangle = \sum_{a_2}^{\chi_2} C^{[2]j_2}_{a_1a_2}|\phi^{[3\dots M]}_{a_2}\rangle\,, \tag{4.15}$$

where C is the coefficient tensor. C can be written as a product of a Γ tensor and the Schmidt coefficient vector for bond 2, $\lambda^{[2]}_{a_2}$. This leads to $C^{[2]j_2}_{a_1a_2} = \Gamma^{[2]j_2}_{a_1a_2}\lambda^{[2]}_{a_2}$. Now we can rewrite Eq. (4.12), using Eq. (4.13) and Eq. (4.14),

$$|\psi\rangle = \sum_{i_1,i_2}^{d}\sum_{a_1}^{\chi_1}\sum_{a_2}^{\chi_2} \Gamma^{[1]i_1}_{a_1}\lambda^{[1]}_{a_1}\Gamma^{[2]i_2}_{a_1a_2}\lambda^{[2]}_{a_2}|i_1,i_2\rangle \otimes |\phi^{[3\dots M]}_{a_2}\rangle\,. \tag{4.16}$$

These steps, when iterated for the remaining $M-3$ bonds, lead to the desired representation in Eq. (4.8) which is denoted as a matrix product state (MPS) [101]. It is an exact representation of the state where we have replaced the d^M coefficients by $(d\chi^2+\chi)M$ coefficients. Here $\chi = \max_l(\chi_l)$ is known as the *Schmidt number*. As χ can grow exponentially with system size, for practically working with the MPS a systematic truncation formalism must exist. We discuss the truncation procedure and the reasons why it works in the next subsection.

4.2.3 Truncation and validity

Considering the bipartite system in Eq. (4.4), we can write down the reduced density operators:

$$\rho_A = \sum_{a=1}^{\chi_{AB}} \lambda_a^2|\phi^A_a\rangle\langle\phi^A_a|\,, \tag{4.17}$$

$$\rho_B = \sum_{a=1}^{\chi_{AB}} \lambda_a^2|\phi^B_a\rangle\langle\phi^B_a|\,. \tag{4.18}$$

The eigenspectra of these matrices are thus given by the squares of the Schmidt coefficients. The central idea of the DMRG method is to keep only those Schmidt vectors which correspond to the D largest eigenvalues. D is known as the *bond* *dimension*. A good assessment of this approximation is given by how the eigenvalues decrease, when written in descending order. For certain classes of gapped systems in 1D the eigenvalues have been observed to decay exponentially [102]. Therefore, the true state can be approximated by reducing the Hilbert space to D which is computationally tractable. The truncation error at each bond for a many-body state, which is an indicator of the difference between the actual state and the truncated state, is quantified using the normalisation of Schmidt coefficients (4.7):

$$\epsilon_l = 1 - \sum_{a_l=1}^{D} \left(\lambda_{a_l}^{[l]}\right)^2 . \tag{4.19}$$

The accuracy of this method of keeping only a fixed number of Schmidt vectors is better for systems containing smaller bipartite entanglement, quantified, for example, by the von Neumann entropy,

$$S_{AB} = -\mathrm{Tr}(\rho_A \mathrm{log}_2 \rho_A) = -\sum_{a=1}^{\chi_{AB}} \lambda_a^2 \mathrm{log}_2 \left(\lambda_a^2\right) . \tag{4.20}$$

To have an intuitive insight into the connection between the bipartite entanglement and the bond dimension, one can look at the maximally entangled state of the bipartite system. The number of basis states required to represent this state exactly is $2^{S_{AB}}$. This gives an idea about the value of bond dimension needed for an exact expression of the state. This truncation method therefore works best for systems containing small bipartite entanglement [103]. It has been shown that for gapped 1D systems governed by short-range Hamiltonians and away from criticality, the von Neumann entropy in the ground state saturates as the size of the system grows [104]. At critical points the von Neumann entropy is shown to be diverging logarithmically with the system size in 1D. These results follow from the so-called *area laws* of entanglement entropy which predict that for the ground states of Hamiltonians with short-range interaction and gap to excitations, the bipartite entanglement entropy is proportional to the surface of the boundary [104]. Hence for the 1D Hamiltonians of interest, a finite value of D can represent the states away from criticality. At critical points the bond dimension needed for a faithful representation diverges polynomially. In practice the numerical results are always checked for convergence with increasing D systematically and for small enough system sizes this method works out quite well in general. Along with this the truncation errors are also checked to ensure that they remain small.

4.2.4 Local expectation value

After the truncation the quantum many-body state can be conveniently stored with at most D Schmidt coefficients at each bond. Now it is quite straightforward to calculate physically interesting quantities. In order to evaluate one such quantity, namely a local expectation value, in the first step a local operator of the form $V^{[l]} \equiv \sum_{i_l,j_l} V^{[l]i_l}_{j_l} |i_l\rangle\langle j_l|$ acts on the state (4.8). We can express the state in terms of local Schmidt basis representations at site l, using the definition from (4.9) and (4.10),

$$|\psi\rangle = \sum_{i_l}^{d} \sum_{a_{l-1}}^{\min(\chi_{l-1},D)} \sum_{a_l}^{\min(\chi_l,D)} \lambda^{[l-1]}_{a_{l-1}} \Gamma^{[l]i_l}_{a_{l-1}a_l} \lambda^{[l]}_{a_l} |\phi^{[1\ldots l-1]}_{a_{l-1}}\rangle \otimes |i_l\rangle \otimes |\phi^{[l+1\ldots M]}_{a_l}\rangle \,. \quad (4.21)$$

To obtain the resulting state $|\tilde{\psi}\rangle$ after the action of the local operator, only the Γ tensor need to be updated,

$$\tilde{\Gamma}^{[l]i_l}_{a_{l-1}a_l} = \sum_{j_l} V^{[l]i_l}_{j_l} \Gamma^{[l]j_l}_{a_{l-1}a_l} \,. \quad (4.22)$$

This step requires $\sim D^2 d^2$ basic operations. The orthonormality of the Schmidt basis reduces the task in the second step of calculating the expectation value to this summation,

$$\langle\psi|V^{[l]}|\psi\rangle = \sum_{i_l} \sum_{a_{l-1},a_l} \left(\lambda^{[l-1]}_{a_{l-1}}\right)^2 \Gamma^{*[l]i_l}_{a_{l-1}a_l} \tilde{\Gamma}^{[l]i_l}_{a_{l-1}a_l} \left(\lambda^{[l]}_{a_l}\right)^2 \,. \quad (4.23)$$

This step requires $\sim D^2 d$ basic operations. Any local observable e.g. number of particles at a site can be evaluated in this way.

4.2.5 Off-Site correlation

Other observables of immense importance are off-site correlation functions, e.g. the single particle density matrix. In this case in the first step an operator acting on two different sites, $V^{[l,l']} \equiv V^{[l]}V^{[l']}$ operates on the following representation of the state,

$$|\psi\rangle = \sum_{i_l,i_{l+1},\dots,i_{l'}} \sum_{a_{l-1},a_l,\dots,a_{l'}} \lambda^{[l-1]}_{a_{l-1}} \Gamma^{[l]i_l}_{a_{l-1}a_l} \lambda^{[l]}_{a_l} \Gamma^{[l+1]i_{l+1}}_{a_l a_{l+1}} \dots \lambda^{[l'-1]}_{a_{l'-1}} \Gamma^{[l']i_{l'}}_{a_{l'-1}a'_l} \lambda^{[l']}_{a_{l'}}$$
$$|\phi^{[1\dots l-1]}_{a_{l-1}}\rangle \otimes |i_l, i_{l+1}, \dots, i_{l'}\rangle \otimes |\phi^{[l'+1\dots M]}_{a_{l'}}\rangle\,, \tag{4.24}$$

where $l' > l$. After the Γ tensors are updated as in the previous case the correlation elements then can be calculated:

$$\langle\psi|V^{[l,l']}|\psi\rangle = \sum_{i_l,i_{l+1},\dots,i_{l'}} \sum_{a_{l-1},a_l,\dots,a_{l'}} \sum_{b_{l-1},b_l,\dots,b_{l'-1}} \left(\lambda^{[l-1]}_{a_{l-1}}\right)^2 \Gamma^{*[l]i_l}_{a_{l-1}b_l} \tilde{\Gamma}^{[l]i_l}_{a_{l-1}a_l} \lambda^{[l]}_{b_l} \lambda^{[l]}_{a_l}$$
$$\Gamma^{*[l+1]i_{l+1}}_{b_l b_{l+1}} \tilde{\Gamma}^{[l+1]i_{l+1}}_{a_l a_{l+1}} \lambda^{[l+1]}_{b_{l+1}} \lambda^{[l+1]}_{a_{l+1}} \dots \Gamma^{*[l']i_{l'}}_{b_{l'-1}a_{l'}} \tilde{\Gamma}^{[l']i_{l'}}_{a_{l'-1}a_{l'}} \left(\lambda^{[l']}_{a_{l'}}\right)^2\,, \tag{4.25}$$

requiring $\sim (l'-l)D^3 d$ basic operations.

4.2.6 Two-site gate

The main advantage of using TEBD method is to be able to work with operators acting on adjacent sites. This becomes a necessary step for time evolution as we deal with such Hamiltonians in this thesis. Such an operator can be written as a two-site gate, $V^{[l,l+1]} \equiv V^{i_l i_{l+1}}_{j_l j_{l+1}} |i_l, i_{l+1}\rangle\langle j_l, j_{l+1}|$. We write the state in terms of local basis at sites l and $l+1$ and the Schmidt basis for the left and right of those two sites:

$$|\psi\rangle = \sum_{i_l,i_{l+1}} \sum_{a_{l-1},a_l,a_{l+1}} \lambda^{[l-1]}_{a_{l-1}} \Gamma^{[l]i_l}_{a_{l-1}a_l} \lambda^{[l]}_{a_l} \Gamma^{[l+1]i_{l+1}}_{a_l a_{l+1}} \lambda^{[l+1]}_{a_{l+1}} |\phi^{[1\dots l-1]}_{a_{l-1}}\rangle \otimes |i_l, i_{l+1}\rangle \otimes |\phi^{[l+2\dots M]}_{a_{l+1}}\rangle\,. \tag{4.26}$$

After the action of the two-site gate the resulting state can be written as,

$$|\tilde{\psi}\rangle = \sum_{i_l, i_{l+1}} \sum_{a_{l-1}, a_{l+1}} \Theta^{i_l i_{l+1}}_{a_{l-1} a_{l+1}} |\phi^{[1 \ldots l-1]}_{a_{l-1}}\rangle \otimes |i_l, i_{l+1}\rangle \otimes |\phi^{[l+2 \ldots M]}_{a_{l+1}}\rangle \,, \tag{4.27}$$

with the following definition,

$$\Theta^{i_l i_{l+1}}_{a_{l-1} a_{l+1}} = \sum_{j_l, j_{l+1}} \sum_{a_l} V^{i_l i_{l+1}}_{j_l j_{l+1}} \lambda^{[l-1]}_{a_{l-1}} \Gamma^{[l] j_l}_{a_{l-1} a_l} \lambda^{[l]}_{a_l} \Gamma^{[l+1] j_{l+1}}_{a_l a_{l+1}} \lambda^{[l+1]}_{a_{l+1}} \,. \tag{4.28}$$

Building all the Θ tensors requires $\sim D^3 d^4$ basic operations. The central idea of the TEBD algorithm is to then ensure orthonormality again at the l-th bond by performing a SVD on the Θ tensor and keeping the D largest Schmidt coefficients. To do so the elements of the Θ tensor are regrouped into $(a_{l-1} \times i_l, i_{l+1} \times a_l)$ matrix, which has at most (Dd, Dd) dimension. The number of basic operations to carry out the SVD step on this matrix is $\sim D^3 d^3$. The SVD is followed by a truncation procedure to keep only the D largest Schmidt coefficients. The new Schmidt vectors that are retained form the adapted truncated Hilbert space at the l-th bond. After reshaping the matrices obtained after SVD into tensor we get,

$$\Theta^{i_l i_{l+1}}_{a_{l-1} a_{l+1}} \rightarrow \sum_{a_l} \Gamma'^{[l] i_l}_{a_{l-1} a_l} \tilde{\lambda}^{[l]}_{a_l} \Gamma'^{[l+1] i_{l+1}}_{a_l a_{l+1}} \,. \tag{4.29}$$

The action of the two-site operator is now conveyed through these new tensors and Schmidt values. To recover the Schmidt values at the $(l-1)$-th and $(l+1)$-th bonds the following operations need to be done,

$$\tilde{\Gamma}^{[l] i_l}_{a_{l-1} a_l} = \left[\lambda^{[l-1]}_{a_{l-1}}\right]^{-1} \Gamma'^{[l] i_l}_{a_{l-1} a_l} \,, \tag{4.30}$$

and

$$\tilde{\Gamma}^{[l+1] i_{l+1}}_{a_l a_{l+1}} = \Gamma'^{[l+1] i_l}_{a_l a_{l+1}} \left[\lambda^{[l-1]}_{a_l}\right]^{-1} \,. \tag{4.31}$$

Here precautions must be taken to avoid division by very small Schmidt values. In practice a cutoff is defined so that Schmidt values only greater than that are considered to ensure numerical stability.

4.2.7 Time evolution using Suzuki-Trotter decomposition

The Hamiltonians we are interested in in this thesis only contain local and next-neighbour terms. Such a Hamiltonian with next-neighbour operators $h^{(2)}_{l,l+1}$ and single site operators $h^{(1)}_{l}$ is written as,

$$H = \sum_{l=1}^{M-1} h^{(2)}_{l,l+1} + \sum_{l=1}^{M} h^{(1)}_{l} \,. \tag{4.32}$$

This Hamiltonian can be expressed solely in terms of next-neighbour operators, i.e. $H = \sum_{l=1}^{M-1} h_{l,l+1}$, with the definition,

$$h_{l,l+1} = h^{(2)}_{l,l+1} + \frac{h^{(1)}_{l}}{2} \otimes \mathbb{1}_{l+1} + \mathbb{1}_{l} \otimes \frac{h^{(1)}_{l+1}}{2} + \delta_{l,1}\frac{h^{(1)}_{l}}{2} \otimes \mathbb{1}_{l+1} + \delta_{l,M-1}\mathbb{1}_{l} \otimes \frac{h^{(1)}_{M}}{2} \,. \tag{4.33}$$

Now the time evolution operator for a short time δt, $U = e^{-iH\delta t}$ can be written in terms of two-site gates ($\hbar \equiv 1$). To do so we first write the Hamiltonian in terms of even and odd operators, namely, $H = \sum_{l \text{ odd}} h_{l,l+1} + \sum_{l \text{ even}} h_{l,l+1}$. This allows for the following expression, correct up to second order in time step,

$$U = \prod_{l \text{ odd}} e^{-ih_{l,l+1}\delta t} \prod_{l \text{ even}} e^{-ih_{l,l+1}\delta t} \, e^{-\frac{1}{2}\left[\sum_{l \text{ odd}} h_{l,l+1}, \sum_{l \text{ even}} h_{l,l+1}\right]\delta t^2} \,, \tag{4.34}$$

where we have used the compatibility of each of the even and odd terms with each one of their own kind. To express the time evolution operator as a product of two-site gates we use Suzuki-Trotter decompositions [105] which preserve the unitarity of the time evolution operator. In the first-order expansion where the error introduced is $\mathcal{O}\left(\delta t^2\right)$, we get,

$$U = \prod_{l \text{ even}} e^{-ih_{l,l+1}\delta t} \prod_{l \text{ odd}} e^{-ih_{l,l+1}\delta t} + \mathcal{O}\left(\delta t^2\right) \,. \tag{4.35}$$

These gates acting on neighbouring sites can be sequentially applied on a quantum state as explained in the previous subsection. The Trotter errors can be made smaller by choosing smaller time steps. The other way of reducing the error is to use higher order expansions [106]. For example, the second order Suzuki-Trotter decomposition looks like,

$$U = \prod_{l \text{ odd}} e^{-ih_{l,l+1}\frac{\delta t}{2}} \prod_{l \text{ even}} e^{-ih_{l,l+1}\delta t} \prod_{l \text{ odd}} e^{-ih_{l,l+1}\frac{\delta t}{2}} + \mathcal{O}\left(\delta t^3\right) , \qquad (4.36)$$

which produces $\mathcal{O}\left(\delta t^3\right)$ error. Fourth order Suzuki-Trotter decompositions are also widely used which give $\mathcal{O}\left(\delta t^5\right)$ error. An application of the time evolution operator on the quantum state where all the two-site gates act once on the quantum state is known as a *sweep*. For evolution with imaginary time these gates are non-unitary and therefore result in orthonormality problems. We address this issue in the next subsection.

4.2.8 Imaginary time evolution

The ability to perform time evolution on a quantum state can be used to find the ground state of the system using imaginary time during the simulation so that the evolution operator becomes e^{-Ht}. This operator when acted on the state expanded in the eigenbases of the Hamiltonian H, can be seen to suppress all states other than the ground state exponentially:

$$\begin{aligned} e^{-Ht}|\psi\rangle &= \sum_{n=0} e^{-E_n t} c_n |E_n\rangle \\ &= e^{-E_0 t}\left(c_0|\psi_{\mathrm{GS}}\rangle + \sum_{n=1} e^{-(E_n - E_0)t}|E_n\rangle\right) , \end{aligned} \qquad (4.37)$$

which will have more weight for the ground state if an energy gap exists between the ground and first excited state. It is therefore clear to see that when simulated for large enough time the system will be steered into the ground state provided that the initial state has a non-zero overlap with the ground state. This method of ground state search is quite robust against numerical noise. This is because any faulty intermediate state can potentially be regarded as a new starting state for the search. Moreover the numerical noises help fulfilling the non-zero overlap condition between the starting state and the ground state. In practice usually a product state of the quantum many-body system is chosen to initiate the simulation as it is very straightforward to be turned into an MPS form. The initial product state,

$$|\psi_p\rangle = \prod_{l=1}^{M} \left(\sum_{i_l=1}^{d} c_{i_l} |i_l\rangle \right) \tag{4.38}$$

can be expressed in the form of Eq. (4.8) by choosing to write $\lambda^{[l]}_{a_l} = \delta_{a_l,1}$ and $\Gamma^{[l]i_l}_{a_{l-1}a_l} = c_{i_l}\delta_{a_{l-1},1}\delta_{a_l,1}$. Now provided $\langle\psi_p|\psi_{\mathrm{GS}}\rangle \neq 0$ the ground state can be reached:

$$|\psi_{\mathrm{GS}}\rangle = \lim_{t\to\infty} \frac{e^{-Ht}|\psi_p\rangle}{\parallel e^{-Ht}|\psi_p\rangle \parallel} \, . \tag{4.39}$$

The normalisation in practice is actually done by normalising the Θ tensor after each two-site gate has been applied.

One important problem that arises here due to the non-unitarity of the gate is that this operation at the sites $(l, l+1)$ explicitly orthonormalises the Schmidt vectors $\left\{|\phi^{[1\ldots l]}_{a_l}\rangle\right\}$ and $\left\{|\phi^{[l+1\ldots M]}_{a_l}\rangle\right\}$ but assumes that the Schmidt vectors at all the other bonds stays orthonormal. While this is the case for a unitary operation, a non-unitary operator can affect the orthonormality of the Schmidt vectors that is connected to the part of the system where it acts. Therefore for these two sites in question, on the left part $\left\{|\phi^{[1\ldots l+1]}_{a_{l+1}}\rangle\right\}, \left\{|\phi^{[1\ldots l+2]}_{a_{l+2}}\rangle\right\}, \ldots$ and on the right part $\left\{|\phi^{[l\ldots M]}_{a_{l-1}}\rangle\right\}, \left\{|\phi^{[l-1\ldots M]}_{a_{l-2}}\rangle\right\}, \ldots$ may not remain orthonormal. This is unsuitable for a sequential operation of two-site gates if in the next instance sites $l+2$ and $l+3$ are acted on. A simple work-around this problem for Suzuki-Trotter decomposition where the string of odd operators are followed by a string of even operators is the following: odd operator acts on sites $(1, 2)$, identity operator acts on $(2, 3)$, odd operator acts on $(3, 4)$,..., odd operator acts on $(M-1, M)$, identity operator acts on $(M-1, M)$, even operator acts on $(M-2, M-1)$,..., even operator acts on $(2,3)$, identity operator acts on $(1,2)$. Here we have assumed M to be even. These forward and backward sweeps make sure at each step that the necessary Schmidt vectors are orthonormal. After this another two way sweep is performed with only identity operators to restore a completely orthonormal representation of the quantum state.

4.2.9 Particle number conservation

Optimisation of the TEBD code is possible by importing several tools from the DMRG language. One such instance would be the implementation of conserved quantum numbers such as total particle numbers, total magnetisation etc. In this thesis we deal with Hubbard models with fixed number of particles. In this case if the total number of particles is N then the $\Theta^{i_l i_{l+1}}_{a_{l-1}a_{l+1}}$ obtained after the two-site gate operation is only nonzero when $N\left(a_{l-1}\right)+N\left(i_l\right)+N\left(i_{l+1}\right)+N\left(a_{l+1}\right)=N$. Defining N_R as the number of particles on the right subsystem of site l we can write the resulting state after the two-site gate operation, following Eq. (4.27),

$$|\tilde{\psi}\rangle = \sum_{N_R} \sum_{a_{l-1},i_l|N-N_R} \sum_{i_{l+1},a_{l+1}|N_R} \Theta^{i_l i_{l+1}}_{a_{l-1}a_{l+1}} |\phi^{[1\ldots l-1]}_{a_{l-1}}\rangle \otimes |i_l, i_{l+1}\rangle \otimes |\phi^{[l+2\ldots M]}_{a_{l+1}}\rangle \,, \tag{4.40}$$

where the state indices are such that they obey the particle conservation on both left and right of the site l. Now for a particular value of N_R the elements of the Θ tensor can be regrouped into θ matrices of N_R-dependant dimensions $((a_{l-1}\times i_l)_{N_R},(i_{l+1}\times a_l)_{N_R})$. We can then write,

$$|\tilde{\psi}\rangle = \sum_{N_R} \sum_{(a_{l-1}\times i_l)_{N_R}} \sum_{(i_{l+1}\times a_l)_{N_R}} \theta^{N_R}_{(a_{l-1}\times i_l)_{N_R},(i_{l+1}\times a_l)_{N_R}} |\phi^{[1\ldots l-1]}_{a_{l-1}}\rangle \otimes |i_l, i_{l+1}\rangle \otimes |\phi^{[l+2\ldots M]}_{a_{l+1}}\rangle \,. \tag{4.41}$$

As we work with two-site gates that conserve the total number of particles on those two sites, the matrix corresponding to the full Θ tensor is block-diagonal with the θ^{N_R} matrices making up the blocks for particular values of N_R when the basis states are appropriately ordered. Therefore instead of performing an SVD on the full matrix we can separately work on the blocks and this is what optimises the algorithm by causing a noticeable speedup and also allowing for larger bond dimensions. In practice for each site every particular quantum number is tabulated starting from the initial state during a time evolution. This can be done by storing each of the Γ tensors for all sites and for all possible values of N_R^l, i.e. with an extra index. These $\Gamma^{[l,N_R^l]}$ tensors are then updated when the corresponding θ^{N_R} matrices go through SVD followed by truncation.

In case there is more than one conserved quantum number, we need to fulfil the conservation of all of them simultaneously and correspondingly the single quantum number N_R would be replaced by a vector of quantum numbers.

4.3 Quantum trajectory algorithm

In this thesis we typically work with quantum systems that are not isolated from the environment. Quantum trajectory methods [71–73, 107, 108], which were developed in the early 1990s in the quantum optics context have proved to be robust techniques to study general open quantum systems provided the master equation can be written in Lindblad form. In this method the master equation is essentially rewritten so that the quantum system evolves in time under an effective Hamiltonian until it is affected by a particular type of decoherence at a particular point of time. In the end a properly wighted stochastic average is carried out over all these different types of decoherence and the time instances.

The master equation for the density operator ρ of an open quantum system written in the Lindblad form is

$$\frac{d}{dt}\rho = -\frac{i}{\hbar}[H,\rho] + \sum_m \gamma_m \left(c_m \rho c_m^\dagger - \frac{1}{2} c_m^\dagger c_m \rho - \frac{1}{2} c_m^\dagger c_m \rho \right) , \tag{4.42}$$

where H is the system Hamiltonian, γ_m is the rate of decoherence due to m-th decay channel and c_m is the Lindblad jump operator corresponding to that channel. This master equation can be rewritten as

$$\frac{d}{dt}\rho = -\frac{i}{\hbar}\left(H_{\text{eff}}\rho - \rho H_{\text{eff}}^{\dagger}\right) + \sum_{m} \gamma_m c_m \rho c_m^{\dagger}\,, \tag{4.43}$$

with the effective (non-hermitian) Hamiltonian defined as

$$H_{\text{eff}} = H - \frac{i}{2}\sum_{m} \hbar\gamma_m c_m^{\dagger} c_m\,. \tag{4.44}$$

In the quantum trajectory method the master equation is rewritten so that it can be considered as a stochastic average over individual trajectories which are numerical evolution as pure states. Evolving the full density operator requires keeping track of $D_{\mathcal{H}}^2$ elements, where $D_{\mathcal{H}}$ is the Hilbert space dimension. Propagating the state vector, on the other hand, only requires evolving $D_{\mathcal{H}}$ elements. This however comes with the burden of sampling over N_{traj} number of quantum trajectories. This would be numerically advantageous over the more expensive propagation of the full density operator only when the number of the trajectories sampled is smaller than the Hilbert space dimension.

The description of this method is presented in the following. If at time t, the density operator $\rho(t)$ corresponds to the pure state $\psi(t)$ (this can be easily generalised to mixed states), then at time $t + \Delta t$, we take

$$|\tilde{\psi}(t + \Delta t)\rangle = (1 - \frac{i}{\hbar} H_{\text{eff}}\Delta t)|\psi(t)\rangle\,, \tag{4.45}$$

resulting in loss of norm Δp, that can be attributed to contributions from the different decay channels Δp_m in the following way

$$\begin{aligned}
\Delta p &= 1 - \langle\tilde{\psi}(t + \Delta t)|\tilde{\psi}(t + \Delta t)\rangle \\
&= \langle\psi(t)|\frac{i}{\hbar}\left(H_{\text{eff}} - H_{\text{eff}}^{\dagger}\right)|\psi(t)\rangle\Delta t \\
&= \langle\psi(t)|\sum_{m} \gamma_m c_m^{\dagger} c_m |\psi(t)\rangle\Delta t \\
&= \sum_{m} \Delta p_m \Delta t\,,
\end{aligned} \tag{4.46}$$

A normalised $|\psi(t+\Delta t)\rangle$ is chosen to be evolved by H_{eff} from the previous instance of time with probability $1-\Delta p$ and acted upon by one of the jump operators with probability Δp. The particular jump operator c_m is chosen with probability $\Delta p_m \Delta t/\Delta p$. Therefore, after normalisation we get,

$$|\psi(t+\Delta t)\rangle = \begin{cases} \frac{(1-\frac{i}{\hbar}H_{\text{eff}}\Delta t)|\psi(t)\rangle}{\sqrt{1-\Delta p}} & \text{with probability } 1-\Delta p \\ \frac{\sqrt{\gamma_m}c_m|\psi(t)\rangle}{\sqrt{\Delta p_m}} & \text{with probability } \Delta p \end{cases} . \tag{4.47}$$

To see the how the ensemble average over the N_{traj} number of quantum trajectories gives equivalent results to the master equation, we construct the corresponding average density operator, $\rho_{av}(t) = |\psi(t)\rangle\langle\psi(t)|$. At time $t+\Delta t$,

$$\begin{aligned} \rho_{av}(t+\Delta t) =& (1-\Delta p)\frac{(1-\frac{i}{\hbar}H_{\text{eff}}\Delta t)|\psi(t)\rangle\langle\psi(t)|(1+\frac{i}{\hbar}H_{\text{eff}}^{\dagger}\Delta t)}{1-\Delta p} \\ &+ \Delta p\sum_m \frac{\Delta p_m \Delta t}{\Delta p}\gamma_m \frac{c_m|\psi(t)\rangle\langle\psi(t)|c_m^{\dagger}}{\Delta p_m} \\ =& \rho_{av}(t) - \frac{i}{\hbar}\Delta t\left(H_{\text{eff}}\rho_{av}(t) - \rho_{av}(t)H_{\text{eff}}^{\dagger}\right) + \Delta t\sum_m \gamma_m c_m \rho_{av}(t) c_m^{\dagger} , \end{aligned} \tag{4.48}$$

which is what the master equation Eq. (4.43) would produce in the first order approximation in time step.

For an operator V, its dynamical expectation value $\langle V\rangle_t$ can be obtained by the following procedure. The trajectories can be taken to be statistically independent under the assumption that the random numbers implemented in the time evolution are truly random. Then $\langle V\rangle_t$ is estimated by the trajectory-average,

$$\overline{V}(t) = \frac{1}{N_{\text{traj}}}\sum_{i=1}^{N_{\text{traj}}} V_i(t) = \frac{1}{N_{\text{traj}}}\sum_{i=1}^{N_{\text{traj}}} \langle\psi_i(t)|V|\psi_i(t)\rangle . \tag{4.49}$$

With the implementation of truly random numbers, $\{V_i(t)\}$ can be taken to be independent and identically distributed random variables with mean $\langle V\rangle_t$. Then in the limit of large N_{traj}, we can apply the central limit theorem and the probability distribution of $\overline{V}(t)$ can be well approximated by a normal distribution with mean $\langle V\rangle_t$. The standard deviation of this distribution is given by,

$$\sigma_{\overline{V}(t)} = \frac{\sigma_{\langle V\rangle_t}}{\sqrt{N_{\mathrm{traj}}}} \,, \tag{4.50}$$

where $\sigma_{\langle V\rangle_t}$ is the true standard deviation for the distribution of $\langle V\rangle_t$. Hence the statistical error of the estimation of $\langle V\rangle_t$, given by $\sigma_{\overline{V}(t)}$, goes as $1/\sqrt{N_{\mathrm{traj}}}$. This formalism of propagating the density operator therefore becomes more accurate as N_{traj} is increased. We would also achieve better results with smaller values of Δt as this method is first order in time-step.

The quantum trajectory algorithm can be easily combined with the TEBD method described in Sec. 4.2. Propagating the state under the effective Hamiltonian H_{eff} or applying a particular jump operator then can be straight-forwardly implemented. For the time evolution normalisation of the state is carried out after a Trotter gate has been applied locally and the normalisation factor is used to determine the nature of the evolution for the next time step as described by Eq. 4.47. The effectiveness of the use of combination of quantum trajectory method with TEBD depends on the behaviour of the entanglement growth in the system which in turn strongly depends on the particular problem and the dynamics in the context of the relevant quantum jumps. These jump operators essentially induce local quantum quenches for individual trajectories which in principle leads to slower growth of entanglement than a global quench [109]. It is advisable, in practice, that the individual trajectories are monitored for the growth of entanglement as it can be significantly for different Hamiltonians and jump operators and for different trajectories.

This brings us to the end of this chapter where we have given an overview of the TEBD method under the DMRG framework to deal with the exponential growth of the Hilbert space in many-body problems. This method can be combined with quantum trajectory algorithm that is also discussed as a means to compute the time evolution in an open quantum system. This particular combination is used in the proceeding chapter to study the open system dynamics of many fermions in optical lattices.

Chapter 5

Dynamics of fermions in optical lattices with radiation bath

5.1 Introduction

This chapter is based on the paper "Light scattering and dissipative dynamics of many fermionic atoms in an optical lattice", Physical Review A, **90**, 023618, (2014) [110]. The objective of this study is to understand the dissipative dynamics due to spontaneous emission in a system of fermionic atoms in an optical lattice formed by far-detuned laser light. We derive the many-body master equation for this system starting from the microscopic description of the atomic structures of both group-I and group-II atoms. We see that the system dynamics is governed by a two-species Fermi-Hubbard Hamiltonian, with tunnelling rate J and onsite interaction energy U, and a master equation that describes light scattering. We then compute the dynamics of the system in two different regimes of interaction

---

This work is taken in part from the publication *Light scattering and dissipative dynamics of many fermionic atoms in an optical lattice*, S. Sarkar, S. Langer, J. Schachenmayer, and A. J. Daley, Phys. Rev. A, **90**, 023618, (2014). The author of this thesis made all of the analytical calculations, and performed or collaborated on all of the numerical calculations, as well as writing most of the article.

that we are particularly interested in, namely, strongly repulsive and strongly attractive. The scattering induced rate of decoherence γ is usually much smaller than the energy scales in the Hamiltonian and in current experiments, γ can be chosen to be around $0.001 - 0.01J$. The relevant dynamical energy scale for the ordered states that are formed in these regimes however comes form spin super-exchange processes in perturbation theory and is $\sim J^2/U$. This implies that the system might be quite susceptible to the rate of decoherence in the strongly interactive regime where $U \sim 10J$. The contrasting results that we obtain for the magnetically ordered ground state in the repulsive case and the ground state comprising mostly of bound dimers in the attractive case are reported in the following sections. In the first case we find the effect of decoherence is greatly suppressed while in the second case the susceptibility of coherence in the system is found to be enhanced. In this work along with analytical methods we also use a combined approach of time-dependent DMRG methods and the quantum trajectories algorithm for the numerical calculations. We start in Sec. 5.2 with an introduction to the atomic physics of a single group-I atom or group-II atom and justify the microscopic assumptions we use as a basis for describing the many-body dynamics. In Sec. 5.3 we outline the derivation of the many-body master equation for light scattering by fermionic atoms. Sec. 5.4 presents the intuitive regime of atoms in a double-well potential, which leads to Sec. 5.5, where we study the full many-body dynamics on a lattice. A brief summary is included in Sec. 5.6.

5.2 Atomic physics

To provide the framework for the derivation of the master equation, we summarise the relevant atomic physics for the atomic species predominantly used in experiments with ultracold atoms. Group-I (alkali-metal) atoms have been used widely, and recently group-II (alkaline-earth-metal) atoms have been established for the realisation of systems with SU(N) symmetry [111, 112] . We consider spontaneous emissions when an atom is trapped in an optical lattice created by a far-detuned laser field and show that the atom returns to the same state it started from with very high probability. In addition the scattered photons are also indistinguishable, resulting in low direct spin decoherence.

To compute the transition rates we start by solving the optical Bloch equations for multi-level systems in the presence of a far-detuned laser field and radiation bath. In the steady state the relative probability amplitude associated with the ith excited level is $\Omega_i/2\Delta_i$, where Ω_i and Δ_i are the Rabi frequency and detuning for that level respectively. Therefore we take an atom consisting of ground states $(|g_1\rangle, |g_2\rangle, ...)$ that can be virtually excited to a set of excited states $(|e_1\rangle, |e_2\rangle, ...)$ due to the presence of a laser which, with respect to $|g_i\rangle$ and $|e_j\rangle$, is detuned by Δ_{ij} and gives rise to a Rabi frequency Ω_{ij}. If $|g_i\rangle$ is the starting state of the atom then the virtually excited state can be shown, by solving the optical Bloch equations, to be $|e_{g_i}\rangle \propto \sum_j (\Omega_{ij}/\Delta_{ij})|e_j\rangle$. The spontaneous decay rate from $|e_{g_i}\rangle$ to a ground state $|g_f\rangle$ is then given by Fermi's golden rule and is $\propto |\sum_q \langle g_f|d_q|e_{g_i}\rangle|^2$ where d_q is the projection of the dipole operator along q, the polarisation of the emitted photon. The dipole matrix elements between two hyperfine states states is given by (see, for example Ref. [15]),

$$\begin{aligned}
&\langle F', m'_F|d_q|F, m_F\rangle \\
&= \langle F', m'_F|\sqrt{\frac{4\pi}{3}} erY_1^q|F, m_F\rangle \\
&\propto \text{Radial part} \times (-1)^{1+I+S+J+L'+J'-m'_F}\sqrt{(2J+1)(2F+1)(2J'+1)(2F'+1)} \\
&\begin{pmatrix} F & 1 & F' \\ m_F & q & -m'_F \end{pmatrix} \begin{Bmatrix} L' & J' & S \\ J & L & 1 \end{Bmatrix} \begin{Bmatrix} J' & F' & I \\ F & J & 1 \end{Bmatrix},
\end{aligned} \tag{5.1}$$

where the array of quantum numbers in parentheses denote the Wigner $3j$ symbols and the array in curly braces denote Wigner $6j$ symbols. The radial part gives the same multiplicative factor for the relevant calculations as we always look at the ratio of dipole elements between S and P orbitals. One can also calculate the dipole transition matrix between two $|J, m_J; I, m_I\rangle$ states and this matrix element is given by (see [15]),

$$\langle J', m_J'; I, m_I' | d_q | J, m_J; I, m_I \rangle \propto \text{Radial part} \times (-1)^{L'+J'-m_J'} \sqrt{(2J+1)(2J'+1)} \begin{pmatrix} J & 1 & J' \\ m_J & q & -m_J' \end{pmatrix} \begin{Bmatrix} L' & J' & S \\ J & L & 1 \end{Bmatrix} \delta_{m_I, m_I'} \,. \tag{5.2}$$

Now we connect this result with the hyperfine atomic structures of group-I and group-II atomic cases. Calculating the dipole matrix elements [15] enables us to write down the excited state that a particular ground state would go to in the presence of a laser with a particular polarisation q. In general the corresponding excited state will be a superposition of different hyperfine states. The interference between the decay channels from these states gives the resultant final decay rate to any of the ground states. In the following we give two prototypical explicit examples for both atomic species, ^{171}Yb (group-II like) and ^{6}Li (group-I).

5.2.1 Group-II like atoms

First we look at the case of group-II like atoms. We specifically choose ^{171}Yb [Fig. 5.1(a)] as it has similar electronic structure to group-II atoms with two valence electrons in the outer shell. This atom has a ground state which is a spin singlet, with zero total electronic angular momentum. Hence the ground states differ only in the z-component of the nuclear spin, $I = 1/2$, and we have two states in the lowest manifold. The electric field of the laser only couples directly to the orbital motion of the electron, and we can define a detuning Δ from the most closely coupled excited level, e.g., $^{1}\mathrm{P}_1$ (using spectroscopic notation), as the difference between the laser frequency and atomic transition frequency. If the field is far detuned, i.e., Δ is large compared with the hyperfine structure energy splitting δ_{hfs}, then the individual hyperfine states cannot be resolved, and the hyperfine coupling cannot be used to rotate the nuclear spin state during spontaneous emissions. Phrased in a different way, we can note that a particular choice of ground state is always coupled to a superposition of excited hyperfine states,

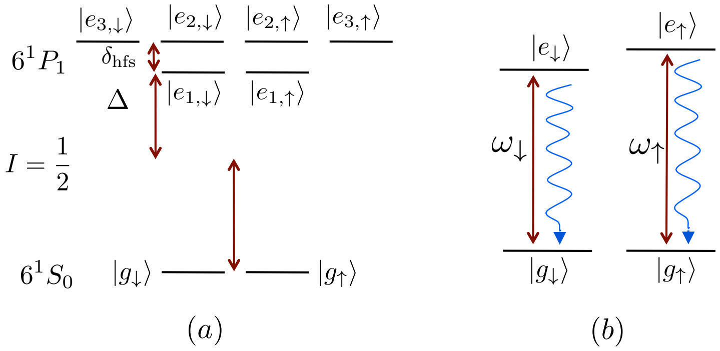

FIGURE 5.1: (a) Atomic structure of ^{171}Yb (nuclear spin $I = 1/2$). We use the spectroscopic notation for the sublevels and show hyperfine structure splittings of the lowest singlet levels (energies are not drawn to scale). The ground states have total electron spin of zero and states in this manifold essentially only differ in the nuclear spin component m_I. We write the two ground states as spin down and spin up states for $m_F = -1, 1$ respectively. (b) Reduction of this hyperfine structure to an effective four-level system where, for very large detuning ($\Delta \gg \delta_{\rm hfs}, |\omega_\uparrow - \omega_\downarrow|$), we can neglect the possibility of a spin flip and can take the photons scattered from each spin system to be identical.

which depends on the detuning. For large detuning this superposition is such that when the atoms return to the ground state, decay channels corresponding to a spin flip interfere destructively and its relative rate is of the order $\sim (\delta_{\rm hfs}/\Delta)^2$.

To give a concrete example, if we take the laser polarisation to be along the $\hat{\mathbf{z}}$-axis i.e. $\mathbf{E} = E\hat{\mathbf{e}}_0$, and apply it on $|g_\uparrow\rangle$ [Fig. 5.1(a)], the atom, in the limit of large detuning, goes to an excited state which is a superposition of $^1P_1$ states with the same m_F (as polarisation is linear) and we have

$$|e\rangle \propto \left[\frac{1}{3\Delta}|e_{1,\uparrow}\rangle + \frac{\sqrt{2}}{3(\Delta+\delta_{\rm hfs})}|e_{2,\uparrow}\rangle\right] . \tag{5.3}$$

The prefactors come from the different dipole matrix elements. Expansion of $|F, m_F\rangle$ basis into $|L, m_L; S, m_S; I, m_I\rangle$ basis reveals that for very large detuning $|e\rangle$ has the same nuclear spin as the starting ground state. Therefore to conserve the nuclear spin under experimental timescales the relative decay rate for a spin flip is suppressed and given by $\propto (\delta_{\rm hfs}/\Delta)^2$. In Table 5.1 we show the different transition rates for different laser polarisations. There is an overall multiplicative factor $\sim (1/\Delta)^2$ for all the rates given.

	$q=0$		$q=1$		$q=-1$	
	$\vert g_\uparrow\rangle$	$\vert g_\downarrow\rangle$	$\vert g_\uparrow\rangle$	$\vert g_\downarrow\rangle$	$\vert g_\uparrow\rangle$	$\vert g_\downarrow\rangle$
$\vert g_\uparrow\rangle$	1	$\left(\frac{\sqrt{2}}{3}\frac{\delta_{\text{hfs}}}{\Delta}\right)^2$	1	0	1	$\left(\frac{\sqrt{2}}{3}\frac{\delta_{\text{hfs}}}{\Delta}\right)^2$

TABLE 5.1: Matrix elements for the possible decay processes in Fig 5.1.

In typical experimental setups where $\delta_{\text{hfs}} \approx 324$ MHz [113, 114], and far-off-resonance lattices can be detuned by tens or hundreds of nanometers ($\sim 10^{14}$Hz), this rate of spin flips is extremely small. In such a limit, the group-II atomic system can be regarded as an assembly of two decoupled two-level systems for the two different nuclear spin states [Fig. 5.1(b)]. Relative shifts of the transition frequencies between the levels are small, but to account for any small difference, we define transition frequencies $\omega_\uparrow$ and $\omega_\downarrow$, as shown in Fig. 5.1(b). For large detuning, $\Delta \gg |\omega_\uparrow - \omega_\downarrow|$ and the relative frequencies of the scattered photons cannot be resolved [115], resulting in suppression of direct spin decoherence. We explore the differences between identical and non-identical photon scattering in more detail in Sec. 5.3.

5.2.2 Group-I atoms

In addition to the considerations in the group-II case, group-I atoms such as ^{6}Li have nonzero electron spin in the ground state. We then need to consider the role of fine structure coupling and include excited levels in $^2P_{1/2}$ and $^2P_{3/2}$ (as shown in Fig. 5.2). These have a fine-structure energy difference δ_{fs} between them and hyperfine-structure energy splittings $\delta_{\text{hfs},P_{1/2}}$ and $\delta_{\text{hfs},P_{3/2}}$ within each manifold of states. Analogous to the group-II case, spin-flip processes that must change the nuclear spin are suppressed if the detuning is much larger than the hyperfine-structure splitting, and also spin-flip processes changing the electronic spin are suppressed when the detuning is much larger than δ_{fs}. An example of a spin flip between two ground states that have different electron spins is $|g_D\rangle \to |g_E\rangle$ in Fig. 5.2. The relative rate of spin flip processes is $\propto (\delta_{\text{fs}}/\Delta)^2$. An example of the flip of a nuclear spin is $|g_D\rangle \to |g_A\rangle$, where the relative spin flip rate from a laser

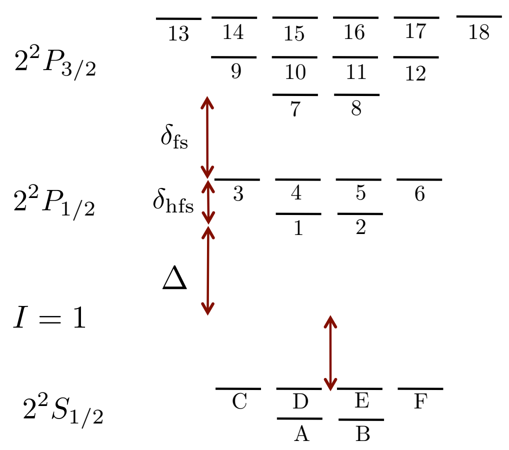

FIGURE 5.2: Diagram of the atomic structure of ^{6}Li (nuclear spin $I = 1$) showing the lowest hyperfine manifolds (energies not drawn to scale). The ground states in the S sublevel are labeled by $A, B, \ldots, F$ and the excited states in P sublevels are labeled by $1, 2, \ldots, 18$. These names will be used in the text in discussing transitions between different levels.

polarised along z-axis is $\propto (\delta_{{\rm hfs},P_{1/2}}/\Delta - \delta_{{\rm hfs},P_{3/2}}/\Delta)^2$, with constants that can be computed from the different dipole matrix elements.

For a detailed example of calculation of the spin flip rates let us look at the ^{6}Li atom starting at $|g_D\rangle$ (Fig. 5.2) with a linearly polarised laser ($q = 0$). The excited state would be a superposition of states in P sub levels with the same nuclear-spin component:

$$|e\rangle \propto -\frac{2\sqrt{2}}{9\Delta_1}|e_1\rangle - \frac{1}{9\Delta_1}|e_4\rangle - \frac{1}{9\Delta_2}|e_7\rangle - \frac{2}{9\sqrt{5}\Delta_2}|e_{10} + \frac{1}{\sqrt{5}\Delta_2}|e_{15}\rangle\,, \tag{5.4}$$

with $\Delta_1 = \Delta$ and $\Delta_2 = \Delta_1 + \delta_{\rm fs}$. There are also possibilities of two different types of spin flips here. Considering a decay towards $|g_A\rangle$ we see that this state is orthogonal to $|g_D\rangle$ in terms of the combination of electron and nuclear spins, namely, in the $|L, m_L; S, m_S; I, m_I\rangle$,

$$|g_D\rangle \propto |0,0\rangle \otimes \left(|\frac{1}{2}, -\frac{1}{2}; 1, 0\rangle + \alpha|\frac{1}{2}, \frac{1}{2}; 1, -1\rangle\right)\,. \tag{5.5}$$

$q = 1$						
	A	B	C	D	E	F
B	0	1	0	0	$\left(\frac{2\sqrt{2}}{9}(\beta_3)\right)^2$	$\left(\frac{2}{3\sqrt{3}}(\beta_3)\right)^2$
E	0	$\left(\frac{2\sqrt{2}}{9}(\beta_3)\right)^2$	0	0	1	$\left(\frac{\sqrt{2}}{3\sqrt{3}}\beta_3\right)^2$
F	0	0	0	0	0	1

$q = 0$						
	A	B	C	D	E	F
B	$\left(\frac{\sqrt{2}}{9}\beta_3\right)^2$	1	0	$\left(\frac{2}{9}\beta_3\right)^2$	$\left(\frac{2\sqrt{2}}{3}(\beta_1 - \beta_2)\right)^2$	$\left(\frac{2}{3\sqrt{3}}\beta_3\right)^2$
E	$\left(\frac{2}{9}\beta_3\right)^2$	$\left(\frac{2\sqrt{2}}{27}(\beta_1 - \beta_2)\right)^2$	0	$\left(\frac{2\sqrt{2}}{9}\beta_3\right)^2$	1	$\left(\frac{\sqrt{2}}{3\sqrt{3}}\beta_3\right)^2$
F	0	$\left(\frac{2}{9\sqrt{3}}\beta_3\right)^2$	0	0	$\left(\frac{\sqrt{2}}{9\sqrt{3}}\beta_3\right)^2$	1

$q = -1$						
	A	B	C	D	E	F
B	$\left(\frac{\sqrt{2}}{9}\beta_3\right)^2$	1	$\left(\frac{2\sqrt{2}}{9\sqrt{3}}(\beta_1 - \beta_2\right)^2$	$\left(\frac{2}{9}\beta_3\right)^2$	$\left(\frac{2\sqrt{2}}{9}\beta_3\right)^2$	0
E	$\left(\frac{2}{9}\beta_3\right)^2$	$\left(\frac{2\sqrt{2}}{9}\beta_3\right)^2$	$\left(\frac{4}{9\sqrt{3}}(\beta_1 - \beta_2)\right)^2$	$\left(\frac{2\sqrt{2}}{9}\beta_3\right)^2$	1	0
F	$\left(\frac{2\sqrt{2}}{9\sqrt{3}}(\beta_1 - \beta_2)\right)^2$	$\left(\frac{2}{3\sqrt{3}}\beta_3\right)^2$	0	$\left(\frac{4}{3\sqrt{3}}\left(\beta_1 - \frac{4}{5}\beta_2\right)\right)^2$	$\left(\frac{\sqrt{2}}{3\sqrt{3}}\beta_3\right)^2$	1

TABLE 5.2: Matrix elements for the possible decay processes in Fig 5.2.

and,

$$|g_A\rangle \propto |0,0\rangle \otimes \left(\alpha|\frac{1}{2},-\frac{1}{2};1,0\rangle - |\frac{1}{2},\frac{1}{2};1,-1\rangle\right) , \tag{5.6}$$

whereas the spin part of the excited state inside each P sublevel looks like that of $|g_D\rangle$. Therefore the contributions from the hyperfine states in each P sublevel cancel each other given the detuning is large compared to hyperfine structure splitting. A different mechanism of cancellation occurs if we consider a spin flip resulting in the state

$$|g_E\rangle \propto |0,0\rangle \otimes \left(|\frac{1}{2},\frac{1}{2};1,0\rangle + \beta|\frac{1}{2},-\frac{1}{2};1,1\rangle\right) , \tag{5.7}$$

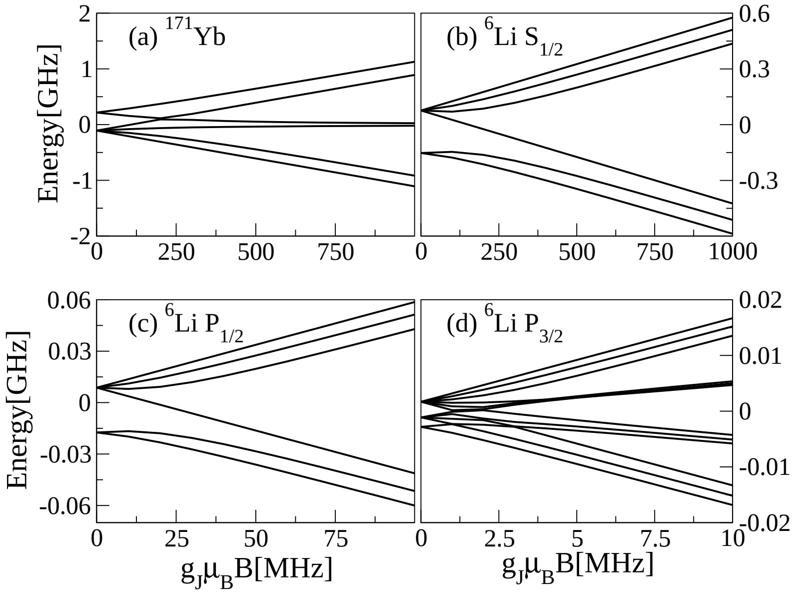

FIGURE 5.3: Zeeman diagram of the different hyperfine levels shows the lifting of degeneracy obtained by numerical diagonalisation for qualitative values of magnetic field. The electron and nuclear spins get decoupled in high enough B field. (a) P_1 sublevel in ^{171}Yb (the S sublevel is already decoupled). (b) Splitting of the $S_{1/2}$ sublevel in ^{6}Li. (c) $P_{1/2}$ sublevel in ^{6}Li needs weaker B field to get decoupled than the previous case as the hyperfine coupling is weaker. (d) Even smaller B field is needed for the even more weakly hyperfine-coupled $P_{3/2}$ sublevel in ^{6}Li. Reprinted figure from S. Sarkar, S. Langer, J. Schachenmayer, and A. J. Daley, Phys. Rev. A, **90**, 023618, (2014) [110].

This is a matrix element for a transition to a state with different electron spin than $|g_D\rangle$. In this case the paths via the two sublevels cancel each other and we obtain a suppression of spin flip as the detuning is large compared to the fine structure splitting. Here also we give in Table 5.2 all the different transition rates for different laser polarisations. There is an overall multiplicative factor $\sim (1/\Delta)^2$ for all the rates given and we define $\beta_1 = \delta_{\mathrm{hfs},P_{1/2}}/\Delta$, $\beta_2 = \delta_{\mathrm{hfs},P_{3/2}}/\Delta$ and $\beta_3 = \delta_{\mathrm{fs}}/\Delta$. The starting states are chosen from the states with positive z-component of total angular momentum in the ground state manifold, as we can perform the same calculations for the other half symmetrically. For a hyperfine structure splitting of $\delta_{\mathrm{hfs}} = 26.1$ MHz for $P_{1/2}$ and 4.5 MHz for $P_{3/2}$, and $\delta_{\mathrm{fs}} = 10.05$ GHz for the fine structure splitting [116], we can again assume that the spin-flip processes are very strongly suppressed in far-detuned lattices and are negligible on experimentally relevant timescales.

This conclusion also holds well when we consider the role of an external magnetic field, included in the Paschen-Back regime. For both ^{171}Yb and ^{6}Li, the spin flip rates stay negligibly small even when an external magnetic field is introduced. For very high magnetic fields though the basic assumption $\Delta \gg |\omega_\uparrow - \omega_\downarrow|$ has to be carefully revisited as the frequencies of the spontaneously emitted photons from different spin states are different now. The field dependence of the energy levels used is showcased in Fig. 5.3. We find that the probability of spin flip processes stays negligible across the whole range of field strengths, provided that the detuning is still much larger than the hyperfine coupling strength. Remarkably, we find that these rates do not change substantially as a function of the magnetic field.

5.3 Master equation for fermionic many-body systems

We now derive the master equation describing fermionic atoms with two internal states, trapped in an optical lattice created by a far-detuned laser field and undergoing spontaneous emissions. We begin from the collective coupling of many atoms to the external radiation field (which we consider as the reservoir or bath), and obtain the equation of motion for the reduced atomic density operator for the motion of the atoms, ρ (traced over the bath) in the form $\dot{\rho} = -i[H, \rho] + \mathcal{L}\rho$ (we take $\hbar \equiv 1$). Here the Hamiltonian H describes the coherent dynamics whereas the Liouvillian $\mathcal{L}\rho$ corresponds to the dissipative dynamics due to spontaneous emission events [93]. Note that this derivation is analogous to the case of a single species of bosonic atoms treated in Ref. [65]. Despite the different particle statistics and in the presence of an additional internal degree of freedom we remarkably obtain qualitatively equivalent terms and a very similar overall structure to the master equation. However, our generalisation now takes into account the effects on the internal state dynamics for multiple electronic ground states, and below we will use this to investigate in detail the interplay between the motional dynamics and correlations in spin-ordered states. The master equation we derive is, however, very general, and can be applied directly to describe fermions in a rich variety of regimes in an optical lattice [117]. Furthermore, while we focus here on the two-species case, we see from the structure of our calculation that both the master equation and the conclusions for spin-ordered states can be straightforwardly generalized to SU(N) spin systems [118, 119].

In our treatment we take an ensemble of atoms, each with a mass m, and with four accessible internal states, electronic ground and excited states $|g\rangle$ and $|e\rangle$ for each of two spin manifolds, giving rise to the four-level systems depicted in Fig. 5.1(b). Initially, we will consider the limit where $\omega_\uparrow = \omega_\downarrow = \omega_{eg}$, denoting the corresponding transition wavenumber by k_{eg}, so that the photons emitted are indistinguishable between the different states. However, we will come back to check this assumption at the end of this section. The system is driven by a laser with frequency ω_L (corresponding to a wavenumber k_L), far detuned from the transition frequency by an amount $\Delta = \omega_L - \omega_{eg}$. Therefore the interactions between the atom and the laser light involve a spatially dependent Rabi frequency $\Omega(\mathbf{x})$, which is proportional to the laser field strength and to the dipole moment of the atom, d_{eg}. To write down the master equation in second quantisation we define the spin (s) dependent field operators $\psi_s(\mathbf{x})$ and they obey fermionic anti-commutation relations $\{\psi_s(\mathbf{x}), \psi^\dagger_{s'}(\mathbf{y})\} = \delta_{s,s'}\delta(\mathbf{x}-\mathbf{y})$. In order to properly account for interactions, as well as losses from short-range contributions, we use standard arguments to separate the dominant contribution to the dynamics at large distances from the short-range physics [77, 120]. This gives rise to interaction terms which for a dilute gas at low scattering energies can be completely characterised by the s-wave scattering length, and for which losses, e.g., due to laser-assisted collisions at short distances can be accounted for via a small imaginary part of this length [121]. In the following we present a detailed derivation of the master equation.

5.3.1 N-atom optical Bloch equation

To write down the second quantised Hamiltonian we use the fermionic field operator $\psi(\mathbf{x}, t)$ (see Fig. 5.1 (b))

$$\psi(\mathbf{x}, t) = \begin{pmatrix} \psi_{e,\uparrow}(\mathbf{x}, t) \\ \psi_{g,\uparrow}(\mathbf{x}, t) \\ \psi_{e,\downarrow}(\mathbf{x}, t) \\ \psi_{g,\downarrow}(\mathbf{x}, t) \end{pmatrix},$$

and raising and lowering operators for the different spins, $\sigma_{\pm,s}$. For the radiation bath the bosonic operators $b_{\lambda,\mathbf{k}}$ ($b^{\dagger}_{\lambda,\mathbf{k}}$) annihilate (create) a photon in the mode $(\mathbf{k}, \lambda)$. The derivation of the master equation is a generalisation of Lehmberg's treatment for deriving the N-atom optical Bloch equation [94], as discussed in Sec. 3.2. Here we also include the atomic motion and fermionic spin into account. The atomic Hamiltonian now contains a kinetic energy term in addition to the internal atomic level structure and coupling to the classical laser field (3.2). The interaction Hamiltonian, which is the dipole coupling with the quantised radiation field, and the field Hamiltonian are similar to their counterparts in 3.2. Proceeding like before we again write down the quantum Langevin equation for an atomic operator, using the standard approximations (the rotating wave approximation and the Born-Markov approximation). For coherent input states, corresponding to the classical laser field, we can equivalently write the master equation for the atomic density operator ρ,

$$\frac{d}{dt}\rho = -i[H_0 + H_{\mathrm{cl}} + H_{\mathrm{dip}}, \rho] + \mathcal{L}\rho\,. \tag{5.8}$$

Here, the first term describes the atomic Hamiltonian, consisting of the kinetic energy term and the atomic structure,

$$H_0 = \int d^3x \psi^{\dagger}(\mathbf{x}, t)\Big(\frac{-\nabla^2}{2m} + \omega_{eg} \sum_{s=\uparrow,\downarrow} |e_s\rangle\langle e_s|\Big)\psi(\mathbf{x}, t)\,. \tag{5.9}$$

The dipole coupling with the classical laser field is described by,

$$H_{\mathrm{cl}} = -\sum_{s=\uparrow,\downarrow} \int d^3x \psi^\dagger(\mathbf{x},t)(\sigma_{+,s}\mathbf{d}_{eg}\cdot\mathbf{E}^+_{\mathrm{cl}}(\mathbf{x},t) + \sigma_{-,s}\mathbf{d}_{eg}\cdot\mathbf{E}^-_{\mathrm{cl}}(\mathbf{x},t))\psi(\mathbf{x},t)\,. \tag{5.10}$$

The Hamiltonian for the dipole coupling with the quantised radiation field is,

$$H_{\mathrm{dip}} = \int d^3x d^3y \Gamma G(k_{eg}\mathbf{r}) \Big(\sum_{s=\uparrow,\downarrow} \psi^\dagger(\mathbf{y},t)\sigma_{-,s}(t)\psi(\mathbf{y},t)\Big)\Big(\sum_{s'=\uparrow,\downarrow} \psi^\dagger(\mathbf{x},t)\sigma_{+,s'}(t)\psi(\mathbf{x},t)\Big)\,, \tag{5.11}$$

and the term describing the dissipative dynamics is,

$$\begin{aligned}\mathcal{L}\rho = \int d^3x d^3y \frac{\Gamma}{2} F(k_{eg}\mathbf{r}) \sum_{s,s'=\uparrow,\downarrow} \Bigg\{ & 2\Big(\psi^\dagger_{e,s}(\mathbf{x},t)\psi_{g,s}(\mathbf{x},t)\Big)\rho\Big(\psi^\dagger_{g,s'}(\mathbf{y},t)\psi_{e,s'}(\mathbf{y},t)\Big) \\ & - \Big(\psi^\dagger_{e,s}(\mathbf{x},t)\psi_{g,s}(\mathbf{x},t)\Big)\Big(\psi^\dagger_{g,s'}(\mathbf{y},t)\psi_{e,s'}(\mathbf{y},t)\Big)\rho \\ & - \rho\Big(\psi^\dagger_{e,s}(\mathbf{x},t)\psi_{g,s}(\mathbf{x},t)\Big)\Big(\psi^\dagger_{g,s'}(\mathbf{y},t)\psi_{e,s'}(\mathbf{y},t)\Big)\Bigg\}\,,\end{aligned} \tag{5.12}$$

where the F and G functions are defined in Sec. 3.2.

5.3.2 Adiabatic elimination

In the limit of large detuning the population in the excited states is negligible compared to that in the ground state and we can write down the master equation solely in terms of ground-state field operators. The precise conditions needed for this requires the detuning Δ to be much larger than Rabi frequency $[\Omega(\mathbf{x}) = 2\mathbf{E}_{\mathrm{cl}}(\mathbf{x})\cdot\mathbf{d}_{eg}]$, spontaneous decay rate Γ, decay rate times the number of particles in a volume λ_L^3 $(\Gamma\langle\psi^\dagger(\mathbf{x})\psi(\mathbf{x})\rangle\lambda_L^3)$, particle kinetic energy and dipole-dipole interaction between the particles.

When these conditions are met we can solve the Heisenberg equation of motion for $\psi^\dagger_{g,+}(\mathbf{x})\psi_{e,+}(\mathbf{x})$ and obtain

$$\psi^\dagger_{g,s}(\mathbf{x})\psi_{e,s}(\mathbf{x}) \approx -\frac{\Omega(\mathbf{x})}{2\Delta}e^{-i\omega_L t}\psi^\dagger_{g,s}(\mathbf{x})\psi_{g,s}(\mathbf{x})\,. \tag{5.13}$$

Treating the other terms similarly we find a master equation for the atoms in the ground state. From here onwards we will follow the convention of omitting the index g in field operators.

In summary the far detuned laser drive allows adiabatic elimination of the atoms in the excited states [94]. In this case working in a frame rotating with the laser frequency we obtain a master equation of the form

$$\frac{d}{dt}\rho = -i\left(H_{\text{eff}}\rho - \rho H^\dagger_{\text{eff}}\right) + \mathcal{J}\rho\,. \tag{5.14}$$

Here the non-Hermitian effective Hamiltonian is:

$$H_{\text{eff}} = H_0 + H^{\text{light}}_{\text{eff}} + H^{\text{int}}_{\text{eff}}\,. \tag{5.15}$$

This effective Hamiltonian describes in addition to the coherent dynamics and the collisional processes also the scattering processes that transfer away the ground state population (therefore not trace preserving). The first term, H_0 is the Hamiltonian for non-interacting atoms in an optical lattice potential originating from the AC-Stark shift [11] induced by a standing wave of laser light:

$$H_0 = \sum_s \int d^3x\psi^\dagger_s(\mathbf{x})\left(-\frac{\nabla^2}{2m} + \frac{|\Omega(\mathbf{x})|^2}{4\Delta}\right)\psi_s(\mathbf{x})\,. \tag{5.16}$$

To model spontaneous emissions we couple the atoms to a radiation bath, namely the vacuum modes of the laser field. The effective Hamiltonian describing the atom-light interaction is given by:

$$\begin{aligned}
H_{\text{eff}}^{\text{light}} =& \sum_{s,s'} \Gamma \int d^3x d^3y G(k_{eg}\mathbf{r}) \frac{\Omega(\mathbf{y})\Omega^*(\mathbf{x})}{4\Delta^2} \psi_s^\dagger(\mathbf{x})\psi_{s'}^\dagger(\mathbf{y})\psi_{s'}(\mathbf{y})\psi_s(\mathbf{x}) \\
&- i\frac{\Gamma}{2} \sum_s \int d^3x \frac{|\Omega(\mathbf{x})|^2}{4\Delta^2} \psi_s^\dagger(\mathbf{x})\psi_s(\mathbf{x}) \\
&- i\frac{\Gamma}{2} \sum_{s,s'} \int d^3x d^3y \frac{\Omega(\mathbf{y})\Omega^*(\mathbf{x})}{4\Delta^2} F(k_{eg}\mathbf{r}) \psi_s^\dagger(\mathbf{x})\psi_{s'}^\dagger(\mathbf{y})\psi_{s'}(\mathbf{y})\psi_s(\mathbf{x})\,. \qquad (5.17)
\end{aligned}$$

5.3.3 Discussion

The first term in $H_{\text{eff}}^{\text{light}}$ gives the dipole-dipole (created by photon exchange) interaction energy. The second term contains single-atom processes which absorb and then emit laser photons. The third term describes a collective two-atom excitation and de-excitation that can give rise to superradiance or subradiance in appropriate limits [94, 122]. Now as G decays as a function of interatomic distance we can focus only on interaction on a small scale set by the laser wavelength. At very short distances ($k_{eg}r \to 0$) it is possible to absorb the dipole-dipole interaction as a small modification to the collisional interactions,

$$H_{\text{eff}}^{\text{int}} = \int d^3x \, g(\mathbf{x})\psi_\uparrow^\dagger(\mathbf{x})\psi_\downarrow^\dagger(\mathbf{x})\psi_\downarrow(\mathbf{x})\psi_\uparrow(\mathbf{x})\,. \qquad (5.18)$$

This term contains short range low-energy two-body scattering processes in the atomic system, characterised by a single parameter, the scattering length a_s. The same scattering length can be obtained using a pseudo-potential in $H_{\text{eff}}^{\text{int}}$ which is a contact potential [77, 120] with $g = 4\pi\hbar^2 a_s/m$. Now in the presence of laser light we also need to take into account light assisted collisional interactions. A red-detuned laser can give rise to optical Feshbach resonance resulting in modification of the scattering length which will depend on the laser intensity [21, 121]. This spatial dependence is reflected in $g(\mathbf{x})$ and away from the resonance we would get back $g \sim 4\pi\hbar^2 a_s/m$. Loss of atoms due to light assisted collisions can be contained in an intensity dependent (and thus spatially dependent) imaginary part to the scattering length. As the rate of such losses are much less than the scattering rate, we can work in a regime where such loss processes have not occurred and can therefore leave out the imaginary part. Higher order corrections such as three-body collisions have also not been considered in this Hamiltonian as we work with dilute gases.

The last term in the master equation is the recycling term:

$$\mathcal{J}\rho = \Gamma \int d^3x d^3y \frac{\Omega(\mathbf{y})\Omega^*(\mathbf{x})}{4\Delta^2} F(k_{eg}\mathbf{r}) \left(\sum_s \psi_s^\dagger(\mathbf{y})\psi_s(\mathbf{y}) \right) \rho \left(\sum_s \psi_s^\dagger(\mathbf{x})\psi_s(\mathbf{x}) \right) , \tag{5.19}$$

which contains Lindblad operators in the form of atomic densities $[\sum_s \psi_s^\dagger(\mathbf{x})\psi_s(\mathbf{x})]$. As the function $F(k_{eg}\mathbf{r})$ falls off on the length scale of laser wavelength, a spontaneous emission process will tend to localise a particle within this length scale, decohering the many-body state. The term $\mathcal{J}\rho$ together with H_{eff} also preserves the trace of the density operator.

5.3.4 Fermi-Hubbard model

We can obtain a multi-band Fermi-Hubbard model for the coherent part of the evolution in the master equation by expanding the field operators in a Wannier basis [81],

$$\psi_s(\mathbf{x}) = \sum_{n,i} w_n(\mathbf{x} - \mathbf{x}_i) c_{n,i,s} , \tag{5.20}$$

under the assumptions of nearest neighbour tunnelling and local interaction in a deep lattice. Here, for the i-th site of the n-th Bloch band, $w_n(\mathbf{x} - \mathbf{x}_i)$ is the Wannier function and $c_{n,i,s}$ is the fermionic annihilation operator for spin s. In an isotropic three-dimensional (3D) cubic lattice we get,

$$\frac{d}{dt}\rho = -i[H, \rho] + \mathcal{L}\rho , \tag{5.21}$$

with the Fermi-Hubbard Hamiltonian,

$$H = -\sum_{n,<i,j>,s} J^{(n)}_{i,j,s} c^{(n)\dagger}_{i,s} c^{(n)}_{j,s} + \sum_{n,i,s} \epsilon^{(n)}_{i,s} c^{(n)\dagger}_{i,s} c^{(n)}_{i,s} + \sum_{i,k,l,m,n} U^{(k,l,m,n)} c^{(k)\dagger}_{i,s} c^{(l)\dagger}_{i,s'} c^{(m)}_{i,s'} c^{(n)}_{i,s} \,. \tag{5.22}$$

Here $J^{(n)}_{i,j,s}$ is the next neighbour tunnelling rate corresponding to the kinetic energy, $U^{(k,l,m,n)}$ is onsite interaction energy coming mainly from collisional interaction with small modification from dipole interactions and $\epsilon^{(n)}_{i,s}$ is the onsite energy offset. The Lindblad term describing the scattering of laser photons is

$$\mathcal{L}\rho = -\sum_{i,j,k,l,m,n,s,s'} \frac{\gamma^{k,l,m,n}_{i,j,s,s'}}{2} \left[c^{(k)\dagger}_{i,s} c^{(l)}_{i,s}, \left[c^{(m)\dagger}_{j,s'} c^{(n)}_{j,s'}, \rho \right]\right] , \tag{5.23}$$

and the matrix elements for different scattering processes is

$$\begin{aligned} \gamma^{k,l,m,n}_{i,j} =& \Gamma \int d^3x d^3y \frac{F(k_{eg}(\mathbf{x}-\mathbf{y}))}{4\Delta^2} \Omega^*(\mathbf{x}) \Omega(\mathbf{y}) \\ & w_k(\mathbf{x}-\mathbf{x}_i) w_l(\mathbf{x}-\mathbf{x}_i) w_m(\mathbf{x}-\mathbf{x}_j) w_n(\mathbf{x}-\mathbf{x}_j) \,. \end{aligned} \tag{5.24}$$

Note that the notation used in Eq. (5.21) is the result of a simple regrouping of the terms in Eq. (5.14) and chosen to make the following arguments towards the use of a single-band Fermi-Hubbard model more transparent. In the Lamb-Dicke regime (i.e. Lamb-Dicke parameter, $\eta = k_L a_0 \ll 1$ with a_0 as the extension of the Wannier functions in the lowest band), for a red detuned lattice spontaneous emissions dominantly return the atoms into the lowest Bloch band [65] as the relative probability for the atom to return to the first excited band scales as η^2. Therefore we focus on the physics that arises from the treatment which is confined only to the lowest band and write down the corresponding master equation,

$$\dot{\rho} = -i[H_{FH}, \rho] + \mathcal{L}_1 \rho \,. \tag{5.25}$$

We now only have a single-band Fermi-Hubbard Hamiltonian

$$H_{FH} = -J \sum_{<i,j>,s} c^{\dagger}_{i,s} c_{j,s} + U \sum_{i} n_{i,\uparrow} n_{i,\downarrow} \,, \tag{5.26}$$

where we have omitted the band indices for the fermionic operators and the Liouvillian term is,

$$\mathcal{L}_1 \rho = \frac{\gamma}{2} \sum_{i} (2 n_i \rho n_i - n_i n_i \rho - \rho n_i n_i) \,. \tag{5.27}$$

Here γ is the effective scattering rate obtained by keeping only the onsite elements in Eq. (5.24) and the Lindblad operators n_i are number operators at each site ($n_i = n_{i,\uparrow} + n_{i,\downarrow} = c^{\dagger}_{i,\uparrow} c_{i,\uparrow} + c^{\dagger}_{i,\downarrow} c_{i,\downarrow}$). It is clear at this point that the dissipative processes do not discriminate between the different spin orientations and can only decohere the many-body state by treating the lattice sites with different total particle numbers differently. In a system where particle numbers for each species are conserved individually, the term in the Hamiltonian corresponding to an energy offset is just a constant and thus can be neglected. Even though we have derived the master equation with two component systems in mind, the generalisation to any number of internal states is straightforward and we can handle SU(N) magnetism with the same formalism. For simplicity, we will mainly focus on the physics of systems with two internal states for the rest of this article.

5.3.5 Non-identical photon scattering

We now come back to the role of large detuning in avoiding direct spin decoherence when the transition frequencies differ for the two two-level systems that represent the different spin states, i.e., $\omega_{\uparrow} \neq \omega_{\downarrow}$. We can modify the above derivation of the master equation at the expense of generating additional terms and look at the dynamics in this more general case. In the following we illustrate the effect for a single particle fixed in space at $\mathbf{x}_0$ having only two internal degrees of freedom, given by the spin s (with energy ω_s associated with its excited state).

The corresponding master equation is given by

$$\begin{aligned}\frac{d}{dt}\rho(t) =& - i\sum_s[\omega_s|e_s\rangle\langle e_s|,\rho] + \sum_s \frac{\gamma_{s,s}}{2}\left(2n_s\rho n_s - n_s n_s\rho - \rho n_s n_s\right) \\ &+ \sum_{s\neq s'}\frac{\gamma_{s,s'}}{2}\left(2n_s\rho n_{s'} - n_s n_{s'}\rho - \rho n_s n_{s'}\right)\,, \end{aligned} \tag{5.28}$$

where the spin dependent scattering rates are defined as follows

$$\gamma_{s,s'} = \Gamma_s \int d^3x \frac{\Omega^*(\mathbf{x}_0)\Omega(\mathbf{x}_0)}{4\Delta_s\Delta_{s'}}|w_0(\mathbf{x}-\mathbf{x}_0)|^4\,. \tag{5.29}$$

The general solution for the atomic density matrix can be obtained analytically and is given by

$$\rho(t) = \left(\begin{array}{cc} \rho_{\uparrow,\uparrow}(0) & \rho_{\uparrow,\downarrow}(0)e^{-(i\triangle\epsilon+\gamma_{\text{eff}})t} \\ \rho_{\downarrow,\uparrow}(0)e^{(i\triangle\epsilon-\gamma_{\text{eff}})t} & \rho_{\downarrow,\downarrow}(0) \end{array}\right)\,,$$

where $\gamma_{\text{eff}} = \left(\gamma_{\uparrow,\uparrow} + \gamma_{\downarrow,\downarrow} - \gamma_{\uparrow,\downarrow} - \gamma_{\downarrow,\uparrow}\right)/2$ and $\triangle\omega = \omega_\uparrow - \omega_\downarrow$ and the associated decay rates Γ_s can differ between spin states. The off-diagonal elements of the density matrix decay in magnitude exponentially with an effective rate γ_{eff}. This direct decoherence of the wave function is an effect of the spontaneous emission processes. Now in the limit of large detuning (i.e. $|\omega_\uparrow - \omega_\downarrow|/\Delta \to 0$) we now show, by expressing all the $\gamma_{s,s'}$ in terms of $\gamma_{\uparrow,\uparrow}$, that the decay rate γ_{eff} scales as $|\omega_\uparrow - \omega_\downarrow|/\Delta$.

To see this we define the small parameters $\epsilon = (\omega_\uparrow - \omega_\downarrow)/\Delta_\uparrow$ and $\epsilon' = (\omega_\uparrow - \omega_\downarrow)/\omega_\uparrow$. Using them we can write $\omega_\downarrow = (1-\epsilon')\omega_\uparrow$ and $\Delta_\downarrow = \Delta_\uparrow/(1-\epsilon)$. The spin-dependent decay rates now can be rewritten in terms of $\gamma_{\uparrow,\uparrow}$ and we get,

$$\begin{aligned}\gamma_{\downarrow,\downarrow} &= \gamma_{\uparrow,\uparrow}(1-\epsilon')^3(1-\epsilon)^2 \\ \gamma_{\uparrow,\downarrow} &= \gamma_{\uparrow\uparrow}(1-\epsilon) \\ \gamma_{\downarrow,\downarrow} &= \gamma_{\uparrow,\uparrow}(1-\epsilon')^3(1-\epsilon)\,. \end{aligned} \tag{5.30}$$

The effective decay rate is therefore,

$$\gamma_{\text{eff}} = \frac{(\gamma_{\uparrow,\uparrow} + \gamma_{\downarrow,\downarrow} - \gamma_{\uparrow,\downarrow} - \gamma_{\downarrow,\uparrow})}{2} = \epsilon\gamma_{\uparrow\uparrow}\frac{(1-(1-\epsilon)(1-\epsilon')^3)}{2} \,. \tag{5.31}$$

Therefore, for large detuning as $\epsilon \to 0$ the off-diagonal elements of $\rho(t)$ do not decay as $\gamma_{\text{eff}} \to 0$. This absence of direct spin decoherence in the system due to spontaneous emission is caused by the fact that the master equation contains cross terms of equal magnitude to the diagonal terms . On the technical level this means the Liouvillian part in Eq. (5.28) reduces to a single particle and single-site version of Eq. (5.27). This case of identical photon scattering is the standard case for fermionic atoms both from group-I and group-II in far-detuned optical lattices.

5.4 Decoherence in a double well

We now proceed to study the effects of spontaneous emissions as described by the master equation derived in the previous section, focusing on the resulting many-body dynamics. We primarily take examples from strongly interacting regimes so that the spatial decoherence in the many body wave function due to localisation of the spin particle following a spontaneous emission event is minimal [65]. We want to investigate the robustness of anti-ferromagnetic spin order of two species fermions in the repulsive case and of the correlation function of the composite bosons [123–125] formed in the case of strong attractive interactions. Therefore we start in the ground states of the strongly interacting Fermi-Hubbard Hamiltonian which are particularly ordered states and investigate the effects of decoherence by evolving with the master equation. Before we present our results for larger lattice systems, we give an intuitive example discussing the decoherence in a double well. For bosons, the dynamics of a related case is discussed in Ref. [126]. Here we particularly focus on the dynamics of the spin degree of freedom, which we treat first by considering the case of an initial ground state with $U > 0$, $|U| \gg J$. We then return to the case of delocalised doublons for strong attractive interactions $U < 0$.

5.4.1 Repulsive interactions

We consider an optical lattice chain with a length of two, containing one spin-up particle and one spin-down particle. Now, in the limit of strong interaction ($U \gg J$) the ground state would be a spin singlet with an admixture of states having both spins in one of the sites. It is instructive to work in a particular basis formed by a combination of Fock states given by $|1\rangle = (|\uparrow,\downarrow\rangle + |\downarrow,\uparrow\rangle)/\sqrt{2}$, $|2\rangle = (|\uparrow,\downarrow\rangle - |\downarrow,\uparrow\rangle)/\sqrt{2}$, $|3\rangle = |\uparrow\downarrow,0\rangle$, and $|4\rangle = |0,\uparrow\downarrow\rangle$. We first calculate the ground state of the two site Fermi-Hubbard Hamiltonian which is nearly a spin singlet with $\mathcal{O}(J^2/U^2)$ population in the manifold with double occupation at one of the sites (Fig. 5.4). Evolving this initial state under the master equation shows that the wave function of the system decoheres due to spontaneous emission until it reaches a steady state ($\dot{\rho} = 0$) where population is equally distributed in all three basis states that were populated at the initial time (Fig. 5.4). The rate at which the spin correlation decays is proportional to that of the increase in the population of doubly occupied states (for a doubly occupied site $S^z = 0$). We calculate this rate in perturbation theory in J/U, where the coherences between the manifolds are eliminated adiabatically to give the decay rate of the spin order. We begin by calculating the decay rate of population in state $|1\rangle$, which is being transferred to the doublet manifold spanned by $|3\rangle$ and $|4\rangle$. Now from the master equation

$$\frac{d}{dt}\rho_{1,1} = -\sum_{k=3,4} 2\sqrt{2}J\mathrm{Re}\left(i\rho_{1,k}\right) . \tag{5.32}$$

The coherences between state $|1\rangle$ and the doublet manifold obey

$$\frac{d}{dt}\rho_{1,3} = i\sqrt{2}J\left(\rho_{3,3} + \rho_{4,3} - \rho_{1,1}\right) + (iU - \gamma)\rho_{1,3}\, , \tag{5.33}$$

and $\rho_{1,4}$ follows an analogous equation. Now the coherence within the doublet manifold is given by

$$\frac{d}{dt}\rho_{3,4} = i\sqrt{2}J\left(\rho_{1,4} - \rho_{3,1}\right) - 4\gamma\rho_{3,4}\, . \tag{5.34}$$

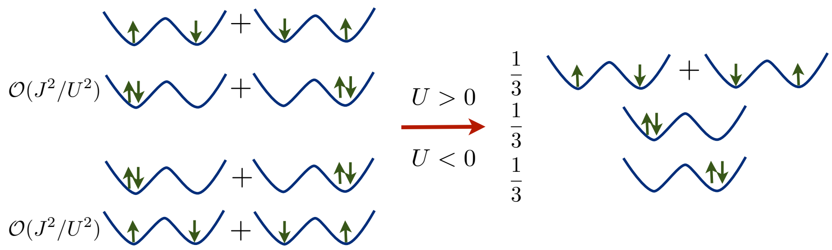

FIGURE 5.4: Decoherence of fermions in a double-well. In the limit of strong interactions for $U > 0$, the ground state of the Fermi-Hubbard Hamiltonian with strong repulsive interactions is primarily a spin singlet (therefore symmetric spatially across the double-well). The population of doubly occupied sites is small $[\mathcal{O}(J^2/U^2)]$. Now for $U < 0$, the initial ground state is a coherent superposition of states with doubly occupied sites with $\mathcal{O}(J^2/U^2)$ population in the spin singlet state. Spontaneous emission events over a significant period of time lead to decoherence of virtual double-occupations, and populate states in which the final steady-state population is evenly distributed in the state with single occupancy and those with doubly occupied sites.

Now in the limit $U \gg J, \gamma$ we can eliminate the coherences between state $|1\rangle$ and the doublet manifold first and that leads us to

$$\frac{d}{dt}\rho_{1,1} = -\left(\frac{4J^2\gamma}{U^2+\gamma^2}\right)(2\rho_{1,1} - \rho_{3,3} - \rho_{4,4}) + 4J^2\mathrm{Re}\left(\frac{\rho_{3,4}+\rho_{4,3}}{\gamma - iU}\right), \tag{5.35}$$

and

$$\frac{d}{dt}\rho_{3,4} = -4\gamma\rho_{3,4} + \frac{4J^2\gamma}{U^2+\gamma^2}(\rho_{4,4} - \rho_{1,1} - \rho_{3,4}). \tag{5.36}$$

Now we can eliminate the coherence in Eq. (5.36) as it contains a term proportional to γ whereas all the other terms are suppressed by a factor of $\mathcal{O}(J^2/U^2)$. We rewrite Eq. (5.35) as

$$\frac{d}{dt}\rho_{1,1} \approx -\left(\frac{4J^2\gamma}{U^2+\gamma^2}\right)(2\rho_{1,1} - \rho_{3,3} - \rho_{4,4}), \tag{5.37}$$

which gives a decay rate proportional to $\beta = 4J^2\gamma/(U^2+\gamma^2)$. The result obtained by evolving the master equation using exact diagonalisation is in agreement with this analytical value as illustrated in Fig. 5.5(a). The spatial average of the spin

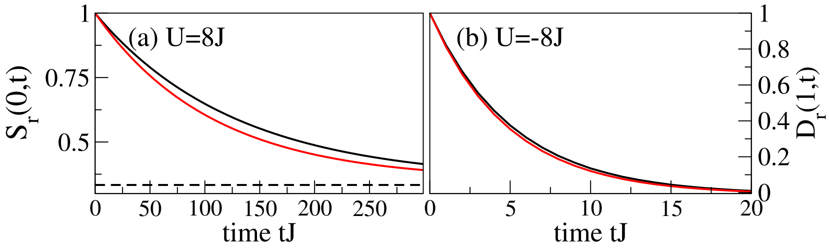

FIGURE 5.5: Decoherent dynamics starting from the ground state of one particle of each spin species interacting strongly in a double well ($M = 2$) for $\gamma = 0.1J$, computed in both, our perturbative approach (red dots) and exact diagonalisation (solid line): (a) decay of the rescaled spin correlations between the sites [Eq. (5.39)] for $U = 8J$. The dashed line indicates the steady-state expectation value. (b) Time evolution of rescaled doublon correlation [Eq. (5.40)] for $U = -8J$ which vanishes in the final steady state.

correlation function is defined as

$$S(\Delta x, t) = \frac{1}{M} \sum_i \langle S_i^z(t) S_{i+\Delta x}^z(t) \rangle \,. \tag{5.38}$$

Here, S_i^z is the z component of spin at lattice site i, defined as $S_i^z = (n_{i,\uparrow} - n_{i,\downarrow})/2$. For the half filled Hubbard model, these spin correlations can also be interpreted as a measure of density fluctuations. All spin components are equivalent due to the SU(2) symmetry of the lattice Hamiltonian and the dissipative terms. Therefore we focus on the z component of spin and for plotting purposes we also consider the rescaled spatial average:

$$S_r(\Delta x, t) = \frac{S(\Delta x, t)}{S(\Delta x, t = 0)} \,. \tag{5.39}$$

The physical process giving rise to the observed decay can be outlined as follows. A spontaneous emission event does not differentiate between the different spin states, but as we saw before, what it effectively detects is the occupation number at the site involved as indicated by the Lindblad operators in Eq. (5.27). In this sense, it distinguishes states with doubly occupied sites from states with singly occupied sites, decohering virtual population of doubly occupied states. This drives the system away from the initial spin ordered ground state which has mostly singly occupied sites with very small doubly occupied population

$[\mathcal{O}(J^2/U^2)]$ and transfers population from states with singly occupied sites to states with doubly occupied sites. The resulting state is no longer an eigenstate and the Hamiltonian therefore starts redistributing population coherently whereas spontaneous emission events continue to disrupt rebuilding of coherence. This interplay between the Hamiltonian and the dissipative dynamics gives rise to the resulting decoherence and change in spin correlation. The rate of decoherence depends on the effective scattering rate γ as well as on the relative population in the doublet manifold which grows proportionally with its initial value. This is the reason we have a term $\mathcal{O}(J^2/U^2)$ in the expression of β, and this reflects the ability of the Hamiltonian to populate doubly occupied sites via tunnelling in the presence of an energy gap. It also shows that the spin order decays much slower than the scattering rate and can be quite robust against spontaneous decay for strongly interacting systems. Alternatively one could argue that the initial state is the ground state which is an eigenstate of the Hamiltonian, and hence the first order of time-dependent perturbation theory is given solely by the action of the dissipative part on the initial state. For the correlation function of interest, we find a vanishing first order term as we don't have direct spin decoherence. Hence the leading order term in the decay rate has to be $\mathcal{O}(J^2/U^2)$.

5.4.2 Attractive interactions

We now consider the case of attractive interactions ($U < 0$), again for one atom of each spin in a double-well, where we observe markedly different dynamics for strong interactions. The ground state of the Hamiltonian now consists of states with double occupation, because the attractive interactions favour the formation of a dimer. The key physical property is that the dimer is delocalised over the two sites, i.e., the ground initial state is essentially a coherent superposition $(|3\rangle + |4\rangle)/\sqrt{2}$. Again, there is a small admixture of the singlet singly occupied state, i.e., a population $\mathcal{O}(J^2/U^2)$ in $|1\rangle$. The final steady state of the master equation at long times is the same with equal population in all these three basis states. However, the initial dynamics towards the steady state begin by rapidly removing the coherence between $|3\rangle$ and $|4\rangle$, markedly changing the state when we consider the dynamics of dimers. We can calculate the decay rate of the doublon correlation functions, e.g., $d_1^\dagger d_2$ in perturbation theory like before. Defining a spatially averaged and rescaled doublon correlation function analogous to the spin case

$$D_r(\Delta x, t) = \frac{1}{M} \frac{\sum_i \langle d_i^\dagger(t) d_{i+\triangle x}(t) \rangle}{\langle d_i^\dagger(t=0) d_{i+\triangle x}(t=0) \rangle}\,, \tag{5.40}$$

we check the agreement between results obtained in exact diagonalisation and perturbation theory (Fig. 5.5(b)). The decay rate for the doublon correlations turns out to be 4γ and is approximately independent of the system size and filling factor, as we show up to first order in time-dependent perturbation theory in Sec. 5.5.3. In that section, we also discuss the enhancement factor, which arises from a combination of having two atoms in a given site, and also having superradiant enhancement because of the scattering of identical photons. An instructive way to check this enhancement factor is to look at the optical Bloch equations for a system of identical two-level atoms fixed on lattice sites and solve for an effective decay rate which is equivalent to calculating the rate of change in ground state population when the excited states can be adiabatically eliminated in the limit of large detuning (Δ) of the driving laser field. For N atoms the atomic density operator (ρ_a) obeys the following equation where the non-Hermitian effective Hamiltonian H', written in terms of Pauli matrices,

$$\frac{d}{dt}\rho_a = -i[H', \rho_a] + \sum_{k,l} \Gamma_{kl} \sigma_k^- \rho_a \sigma_l^+\,, \tag{5.41}$$

with

$$H' = \sum_{k=1}^{N} \left(-\Delta\sigma_k^z - \frac{\Omega_k}{2}(\sigma_k^+ + \sigma_k^-) \right) - \frac{i}{2} \sum_{k,l} \Gamma_{kl} \sigma_k^+ \sigma_l^-\,. \tag{5.42}$$

Here Ω_k is the Rabi frequency for the k-th atom (which we will take to be position independent) and $\Gamma_{kl} = \Gamma F(k_{eg}\mathbf{r}_{kl})$ where Γ is just the spontaneous decay rate of the excited state of an atom and the function F introduces a localising effect on the scattering element between kth and lth site (at a distance r_{kl}) on a scale set by the atomic transition wavelength k_{eg}. We can determine an effective decay rate in the ground-state population which initially (when the system is the ground state $|\psi_0\rangle$) is the rate of decrease in the norm for evolution under the effective Hamiltonian, namely,

$$\Gamma_{\text{eff}} = -\frac{1}{\delta t}[\langle\psi_0|(e^{iH'^{\dagger}\delta t}e^{-iH'\delta t)}|\psi_0\rangle] \approx \langle\psi_0|\sum_{k,l}\Gamma_{kl}\sigma_k^-\sigma_l^+|\psi_0\rangle\,. \tag{5.43}$$

In the single atom case, using second order time-dependent perturbation theory (the dipole coupling with the laser field is the perturbative part of the Hamiltonian), it is easy to calculate this effective decay rate $\Gamma_{\text{single}} = \Gamma\Omega^2/(4\Delta^2)$. Now for two atoms we look at two limiting cases. When the atoms are separated by a distance much larger than the atomic transition wavelength, the scattering elements turn into on-site terms ($\Gamma_{kl} \to \Gamma\delta_{k,l}$) and the effective rate is $2\Gamma_{\text{single}}$. This is what one would expect for the total decay rate of two independent entities. In the opposite case, where the atomic distance is much smaller than the transition wavelength, all the scattering elements become independent of the distance between the atoms ($\Gamma_{kl} \to \Gamma$) and we indeed obtain an effective decay rate of $4\Gamma_{\text{single}}$.

5.5 Dynamics for many atoms

In order to further quantify the impact of spontaneous emissions on many-body correlations we discuss the full many-body problem using approximate analytic and numerically exact solutions to the master equation derived in Sec. 5.3. First we discuss the effects of spontaneous emission on the momentum distribution of non-interacting fermions. Second we analyse the decoherence of antiferromagnetic spin order in the case of strong repulsive interactions, comparing time-dependent perturbation theory for $J/U \to 0$ to numerical data. Depending on the system size we use either exact diagonalisation or combine adaptive time-dependent DMRG with the quantum trajectory approach [73], to capture the decoherence and time dependence of first-order correlation functions in detail. While the first approach is exact, time-dependent DMRG is well established as a convenient means to model the real-time dynamics induced by stochastic processes in one-dimensional systems that remain close to equilibrium.

Our main results on the repulsive case are that the spin-correlation functions are robust on experimentally relevant timescales and that the spin decoherence is governed by a single decay rate which is suppressed by the number of double occupancies in the initial state. In the limit of strong attractive interactions, both the perturbation theory approach and the numerical simulations unveil decay rates of the doublon correlation function enhanced by a factor of 4, which can be understood as a consequence of superradiance [122, 127, 128].

As a first general result we calculate the rate of energy increase induced by the spontaneous emissions for N atoms. This can be obtained analytically from the master equation (5.14), as was done for bosons in Ref. [65], evaluating

$$\frac{d}{dt}\langle H\rangle = \mathrm{Tr}(\mathcal{L}_1 \rho H)\,. \tag{5.44}$$

The final result strongly resembles the result for bosons [65] and is not only independent of the interaction strength but also completely determined by single particle physics [64]:

$$\frac{d}{dt}\langle H\rangle = \frac{\Gamma\Omega_0^2}{4\Delta^2}\frac{k_L^2}{2m}N \qquad (\Omega = \Omega_0 \cos k_L x)\,. \tag{5.45}$$

However, as in the case of bosons, this result does not properly characterise the heating induced by spontaneous emissions as the energy increase predominantly results from excitations to higher bands which will in general not thermalise on experimental time-scales [65]. For bosons this has been quantified in Ref. [66]. Hence, even a qualitative analysis requires at least an analysis of first-order correlation functions such as spin correlations, momentum distribution functions, or the single particle density matrix. In the following we perform such an analysis, first for free fermions, then for repulsive interactions and finally for attractive interactions.

5.5.1 Free fermions

The case of free fermions is another instructive example that can be dealt with exactly. We here focus on the time dependence of the momentum distribution for N fermions on M lattice sites

$$\tilde{n}_q = \sum_s \tilde{c}^\dagger_{q,s}\tilde{c}_{q,s}, \text{ with } \tilde{c}_{q,s} = \sum_{l=1}^{M} \frac{1}{\sqrt{M}} e^{-iql} c_{l,s} \,. \tag{5.46}$$

For $U = 0$ the Hamiltonian is diagonal in momentum space and hence the time-evolution of $\langle \tilde{n}_q \rangle$ is solely given by the action of the dissipative part which results in

$$\frac{d}{dt}\langle \tilde{n}_q \rangle = \mathrm{Tr}(\tilde{n}_q \mathcal{L}_1 \rho) = -\frac{\gamma}{2}\sum_l [n_l, [n_l, \tilde{n}_q]] = -\gamma \langle \tilde{n}_q \rangle + \frac{N}{M}\gamma \,. \tag{5.47}$$

Therefore the steady-state momentum distribution function $\langle n_k \rangle \to N/M$ for $t \to \infty$, i.e., the momentum distribution corresponding to all particles being localised in space by spontaneous emissions. The dynamics leading to this state occur gradually, as particles are spread throughout the Brillouin zone via spontaneous emissions.

5.5.2 Repulsive interactions

In the next step we focus on the repulsively interacting case of fermions which is closely related to the rich physics of magnetic ordering. Spin correlations in the 1D Fermi-Hubbard model is numerically investigated. The effect of different decohering mechanisms on the characteristic correlation functions in this case are essential to be understood and characterised in order to observe quantum magnetism in real experiments. Analytical results [82] and numerical computations [99] show that in 1D interesting many-body effects like the absence of long-range order emerge from strong correlation effects. For strong repulsive interactions a perturbative approach in J/U reduces the Fermi-Hubbard model in 1D to Heisenberg model, a paradigm model of quantum magnetism [129]. This highlights the characteristic energy scale to observe quantum magnetism [32, 41, 130]. The antiferromagnetic order has been measured in experiments and has been found to persist for finite J/U [131]. The decay due to decoherence of the spatially averaged spin correlation functions defined in Eq. (5.38) is investigated here for larger lattice sizes.

In the perturbative approach for the double well in the previous section the decoherence rate was found out to be the scattering rate scaled by the initial population in the doublet manifold. Here we show a generalisation of that behaviour for a chain of length M. To see this we first calculate the decay of spin order using adiabatic elimination process and then connect the pre-factor of scattering rate in this decay rate to the population in the doublet manifold by making the connection between the Fermi-Hubbard Hamiltonian and the Heisenberg Hamiltonian using degenerate perturbation theory, in the limit of strong interaction ($U \gg J$).

The Fermi-Hubbard Hamiltonian, in this limit, can be written as $H_{FH} = H_0 + H_1$ with $H_0 = U\sum_i n_{i,\uparrow}n_{i,\downarrow}$ and $H_1 = -J\sum_{<i,j>,s} c^\dagger_{i,s}c_{j,s}$. We take $|n\rangle$ as the zeroth order ground state (which is just a particular superposition of all the fock states with only singly occupied sites) and let $|k\mu\rangle$ be a fock state with a doubly occupied k-th site and an empty adjacent $(k+\mu)$-th site (μ can be ± 1, except at the boundaries). Using the master equation we the write,

$$\dot{\rho}_{n,n} = \sum_{k\mu} 2\mathrm{Re}\left(ic^*_{k\mu}\rho_{n,k\mu}\right) \qquad\qquad (c_{k\mu} = \langle n|H_1|k\mu\rangle)\,. \tag{5.48}$$

The coherences between the singlet and doublet manifold is governed by,

$$\dot{\rho}_{n,k\mu} = -i\left(\sum_{k'\mu'} c_{k'\mu'}\rho_{k'\mu',k\mu} - c_{k\mu}\rho_{n,n}\right) + (iU-\gamma)\rho_{n,k\mu}\,, \tag{5.49}$$

and the coherences inside the doublet manifold obey,

$$\begin{aligned}
&\dot{\rho}_{k'\mu',k\mu} \\
&= - i \left(c^*_{k'\mu'}\rho_{n,k\mu} - c_{k\mu}\rho_{k'\mu',n}\right) + \frac{\gamma}{2}\sum_j \langle k'\mu'|2n_j\rho n_j - n_jn_j\rho - \rho n_jn_j|k\mu\rangle \\
&= - i \left(c^*_{k'\mu'}\rho_{n,k\mu} - c_{k\mu}\rho_{k'\mu',n}\right) \\
&\quad - \gamma\alpha_{k'\mu',k\mu}\rho_{k'\mu',k\mu} \qquad \left(\alpha_{k'\mu',k\mu} = \begin{cases} 0 & \text{if } k=k', \mu=\mu' \\ >0 & \text{otherwise}\end{cases}\right) . \qquad (5.50)
\end{aligned}$$

Now in this strong interaction limit we first eliminate the coherence between the singlet and doublet manifold and that leads to,

$$\dot{\rho}_{n,n} = -2\sum_{k\mu}\left(\frac{\gamma|c_{k\mu}|^2}{U^2+\gamma^2}\right)(\rho_{n,n}-\rho_{k\mu,k\mu}) + 2\sum_{k'\mu'\neq k\mu}\mathrm{Re}\left(\frac{c^*_{k\mu}c_{k'\mu'}}{\gamma - iU}\rho_{k'\mu',k\mu}\right) , \qquad (5.51)$$

and

$$\begin{aligned}
\dot{\rho}_{k'\mu',k\mu} = {} & ic^*_{k'\mu'}\left(\frac{ic_{k\mu}}{iU-\gamma}\rho_{n,n} + \sum_{k''\mu''}\frac{ic_{k''\mu''}}{iU-\gamma}\rho_{k''\mu'',k\mu}\right) \\
& - ic_{k\mu}\left(\frac{ic^*_{k'\mu'}}{iU+\gamma}\rho_{n,n} - \sum_{k''\mu''}\frac{ic^*_{k''\mu''}}{iU+\gamma}\rho_{k'\mu',k''\mu''}\right) - \gamma\alpha_{k'\mu',k\mu}\rho_{k'\mu',k\mu} . \qquad (5.52)
\end{aligned}$$

With further elimination of coherence in Eq. (5.52) we can now write for the population in the singlet manifold as,

$$\dot{\rho}_{n,n} \approx -2\sum_{k\mu}\left(\frac{\gamma|c_{k\mu}|^2}{U^2+\gamma^2}\right)(\rho_{n,n}-\rho_{k\mu,k\mu}) \qquad (5.53)$$

This equation gives a population transfer rate of $2\sum_{k\mu}\gamma|c_{k\mu}|^2/(U^2+\gamma^2)$. To see the connection of this decay rate to the initial relative population in the doublet manifold , $N_D = 1/N\sum_i d_i^\dagger d_i$ (with $d_i = c_{i,\uparrow}c_{i,\downarrow}$ as the doublon annihilation operator), we first recognise the Fermi-Hubbard Hamiltonian as a Heisenberg Hamiltonian using degenerate perturbation theory in J/U [132, 133]. To see that, let the ground state of H_0 belong to the degenerate subspace S, comprised of states with only singly occupied sites. Therefore we can use degenerate perturbation theory to look at the first order correction to energy and wavefunction. In order to do so we must know the correct zeroth order ground state in S subspace, which can be obtained by diagonalising the tunnelling matrix in the said subspace. But in our case, all these matrix elements are zero as they only connect the S subspace with D, which is the subspace of states with one doubly occupied site adjacent to an empty site. Therefore we have to include the second order processes. This will enable us to build the wavefunction up to first order which is a good estimation of the actual ground state obtained by diagonalising H_{FH}. The ground state in the zeroth order is the solution of the secular equation in the subspace S, given by, $V\psi^{(0)} = \delta E^{(1)}\psi^{(0)}$ where matrix elements of V are,

$$\begin{aligned} V_{n,n'} =& \sum_{k\in D} \frac{\langle n|H_1|k\rangle\langle k|H_1|n'\rangle}{E_n^0 - E_k^0} \qquad (n, n' \in S) \\ =& \frac{J^2}{U}\langle n| \sum_{<k,l>} 2\left[\mathbf{S}_k\cdot\mathbf{S}_l - \frac{1}{4}\mathbb{1}\right]|n'\rangle \end{aligned} \tag{5.54}$$

The ground state of this Heisenberg-like Hamiltonian in subspace S is the correct zeroth order ground state of the Fermi-Hubbard Hamiltonian, $\psi^{(0)}$. Let the eigenstates of V be denoted by $|n\rangle, |n'\rangle, |n''\rangle, \ldots$ and let $|n\rangle = \psi^{(0)}$. Now up to the first order, the ground state of H_{FH} is given by

$$\psi^{(1)} = \psi^{(0)} + \sum_{m=n',n'',\ldots} c_m^{(1)}|m\rangle + \sum_{k\in D} c_k^{(1)}|k\rangle \tag{5.55}$$

with

$$c_m^{(1)} = \frac{1}{\langle n|V|n\rangle - \langle m|V|m\rangle}\sum_{k\in D}\frac{\langle m|H_1|k\rangle\langle k|H_1|n\rangle}{E_n^0 - E_k^0} \text{ and } c_k^{(1)} = \frac{\langle k|H_1|n\rangle}{E_n^0 - E_k^0} \tag{5.56}$$

Therefore the double occupancy in this state

$$N_D = \sum_{k\in D}\frac{|c_k^{(1)}|^2}{|\psi^{(1)}|^2} = \frac{1}{|\psi^{(1)}|^2}\sum_{k\in D}\frac{|\langle k|H_1|n\rangle|^2}{U^2}\,, \tag{5.57}$$

which, in the strong interaction limit, is proportional to the pre-factor of γ in the

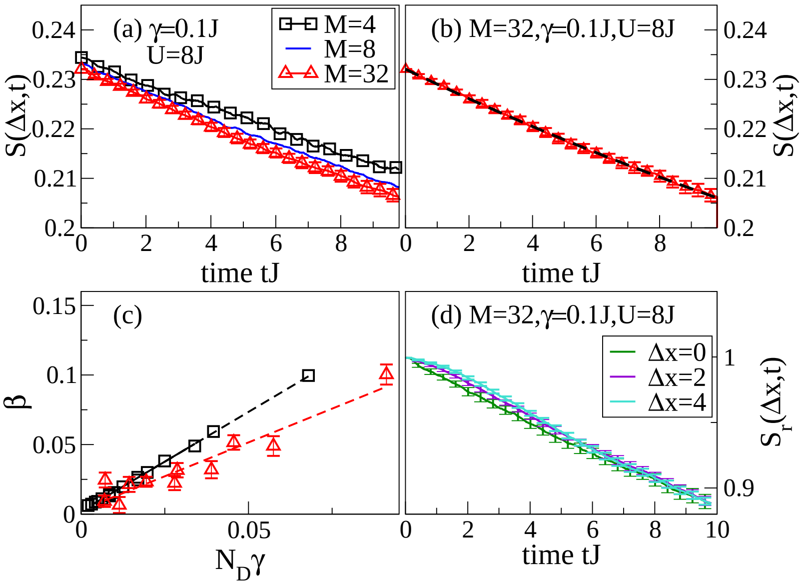

FIGURE 5.6: Comparison of the decay of spin correlations [see Eq. (5.38)] averaged over the chain obtained from exact diagonalisation using the EXPOKIT package [134] for $M = 4, 8$ and tDMRG with $D = 128$ for $M = 32$. (a) Decay of the on-site contribution $S(\Delta x = 0, t)$ for different system sizes $M = 4, 8, 32$ at $U = 8J$ and $\gamma = 0.1J$ using 500 trajectories for $M = 4, 8$ and 250 trajectories for $M = 32$. (b) Example fit to the data shown in panel (a) for $M = 32$. (c) The decay rates β extracted from numerical fits as shown in panel (b) as a function of $N_D\gamma$. The dashed lines in (b) and (c) are linear fits to the data for different system sizes [M=4 (black squares) and M=32 (red triangles), which exhibit the scaling $\beta \sim N_D\gamma$ predicted by perturbation theory. Panel (d) shows the rescaled $S_r(\Delta x, t)$ [Eq. (5.39)] for $M = 32$, $U = 8J$ and different Δx which shows only a weak distance dependence, especially at larger times. Reprinted figure from S. Sarkar, S. Langer, J. Schachenmayer, and A. J. Daley, Phys. Rev. A, **90**, 023618, (2014) [110].

expression obtained earlier for population transfer rate from singlet to doublet manifold. Therefore within the same perturbative approach we can directly relate our expression for the decay rate of the spin correlation, namely $\beta \propto \gamma N_D$. The scaling predicted here are checked numerically for repulsive 1D systems up to $M = 32$ lattice sites.

We report our numerical findings and comparison to perturbative results in Fig. 5.6. Here (a) shows the on-site contribution $S(\Delta x = 0, t)$ decaying with time for interaction value $U = 8J$, $\gamma = 0.1J$, and system sizes $M = 4, 8, 32$, with time-step of $dtJ = 0.01$ and bond dimension of $8M$ in the DMRG calculations keeping the discarded weight below 10^{-5} for $M = 32$ and up to $tJ = 10$. For the averaged quantities finite size effects are found to be small for $M \geq 6$. In Fig. 5.6(c) we show the decay rate β, extracted from a numerical fit of $a \cdot e^{-\beta t} +$ const. to the plots shown in (a) for parameter ranges with $U/J = 4, 6, 8, 10, 12$ and $\gamma/J = 0.2, 0.1, 0.05, 0.025$ as a function of the effective decay rate calculated with perturbation theory, $N_D\gamma$. Fig. 5.6(b) shows an explicit example for $M = 32$ and $\gamma = 0.1J$. The numerically obtained decay rates, within the error bars obtained from the fits, scale linearly with $N_D\gamma$. The system size dependence is essentially captured in the values of N_D. This result matches with our findings from perturbation theory calculations, where we see that the effective decay rate is suppressed with increase in U/J as it is proportional to the value of double occupancies in the initial state. In Fig. 5.6(d) we show the result for $S_r(\Delta x, t)$, for distances $\Delta x = 0, 2, 4$ with $U = 8J$ and $\gamma = 0.1J$, at $M = 32$. Rescaling the data according to Eq. (5.39) shows that the decay of the correlation functions is independent of the distances. The alternating sign of $S(\Delta x, 0)$, which is a necessary condition for antiferromagnetic correlations, is unchanged during the time evolution.

The numerical study presented above of the decay of spin correlation functions for the repulsive Fermi Hubbard model undergoing spontaneous emissions shows that changes in antiferromagnetic correlations are inhibited because the rate is controlled by the number of double occupancies that can be formed. An important role is played by the energy gap in suppressing the coherent processes that form virtually doubly-occupied sites. This leads to a suppression of the decay of magnetic correlations somewhat analogous to the inhibition of diffusion seen for Bosons in Refs. [126, 135]. The fraction of doubly occupied sites is an experimentally controllable parameter [60, 136], and the time-dependence of the spin correlations should be directly measurable in experiments, e.g. using quantum gas microscopes [32, 137]. This robustness shifts the typical rate of decay from γ to $N_D\gamma \sim (J^2/U^2)\gamma$. This compares favourably with the energy scale J^2/U of typical dynamics in this regime. Due to this suppression, the new dominant effect of spontaneous emissions for large enough U will be transfer of particles to higher Bloch bands, the timescales of which is given by $1/(\eta^2\gamma)$.

5.5.3 Attractive interactions

This robustness in the repulsive case against the decay of spin correlation functions is in strong contrast to the effects we observe for attractive interactions, which was also seen in the case of the double-well previously. The analysis of the characteristic correlation functions for many fermions with strong attractive interactions is investigated here. With $U < 0$ and the focus on strong interactions at moderate to low densities, we see that the ground state of the Fermi-Hubbard model consists of bound dimers that behave as composite bosons, and condense to allow condensation, and off-diagonal long-range order of dimers. In the regime of strong attractive interactions doubly occupied sites would contribute heavily in the ground state of our lattice model. This can be shown with the use of degenerate perturbation theory in J/U, as was done in Ref. [138], to arrive at an effective Hamiltonian H_D, which clearly shows the dynamics of bound pairs,

$$H_D = \frac{2J^2}{U} \sum_{<i,j>} \left(d_i^\dagger d_j - n_i^{(D)} n_j^{(D)} \right) . \tag{5.58}$$

This Hamiltonian contains a doublon tunnelling term and a nearest neighbour interaction term with the on-site number operator for doublons, $n_i^{(D)} = d_i^\dagger d_i$. This model prefers pair formation on alternative sites as the energy can then be lowered through virtual tunnelling of doublons ($U < 0$). These pairs approximately behave as composite bosons and due to Pauli-exclusion principle, more than one pair cannot occupy the same lattice site. This perturbative Hamiltonian therefore essentially describes hardcore bosons with next-nearest neighbour interactions. The ground state at low densities is expected to be a superfluid of pairs with the doublon correlation function decaying algebraically [Eq. (5.40)].

We now look at the decay of these correlation functions due to the dissipative dynamics. The first order of time-dependent perturbation theory is given solely by the action of the dissipative part on the initial state as it is the ground state. We calculate the following decay rates:

$$\frac{d}{dt}\langle d_i^\dagger d_j\rangle = \mathrm{Tr}\left(d_i^\dagger d_j \mathcal{L}_1 \rho\right) = \frac{\gamma}{2}\sum_k \langle 2n_k d_i^\dagger d_j n_k - n_k n_k d_i^\dagger d_j - d_i^\dagger d_j n_k n_k\rangle\,, \quad (5.59)$$

where $n_k = n_{k,\uparrow} + n_{k,\downarrow}$. We then compute

$$\begin{aligned} &n_k d_i^\dagger d_j - d_i^\dagger d_j n_k \\ &= -\left(c_{i,\uparrow}^\dagger c_{i,\downarrow}^\dagger c_{j,\downarrow} c_{k,\uparrow} + c_{i,\uparrow}^\dagger c_{i,\downarrow}^\dagger c_{k,\downarrow} c_{j,\uparrow}\right)\delta_{k,j} + \left(c_{k,\uparrow}^\dagger c_{i,\downarrow}^\dagger c_{j,\downarrow} c_{j,\uparrow} + c_{i,\uparrow}^\dagger c_{k,\downarrow}^\dagger c_{j,\downarrow} c_{j,\uparrow}\right)\delta_{k,i}\,, \end{aligned} \quad (5.60)$$

and use this identity to perform the sum over k and arrive at

$$\frac{d}{dt}\langle d_i^\dagger d_j\rangle = \gamma\langle -2d_i^\dagger d_j - 2d_i^\dagger d_j\rangle = -4\gamma\langle d_i^\dagger d_j\rangle\,. \quad (5.61)$$

The pair correlations therefore decay with a rate that is four times the scattering rate. For the Bose-Hubbard model previously calculated rates of decay for off-diagonal elements of the single particle density matrix for interacting bosons was found to be γ [65]. From our calculations in a double well, one factor of 2 arises as two particles form each dimer, whereas the other factor of 2 arises from the superradiant enhancement discussed in Sec. 5.4.2. In a spontaneous emission event from a doublon, the dimension of a single lattice site limits the spatial separation, which is much smaller than the wavelength of the light. The atoms therefore interact with the light in a coherent and collective way [127, 128]. For N_l particles on site l the resulting spontaneous emission rate therefore becomes $N_l^2\gamma$.

Although the perturbative results are expected to be valid only on a short timescale, which is set by the tunnelling rate, our numerical findings for finite size systems, reported in Fig. 5.7, show that the result persists for even longer times. In Fig. 5.7 (a) we report the spatial dependence of D_r (Eq. (5.40)) for system size $M = 8$ at $U = -8J$ and $\gamma = 0.05J$. The results obtained with exact diagonalisation (squares) method and tDMRG method (diamonds) are compared

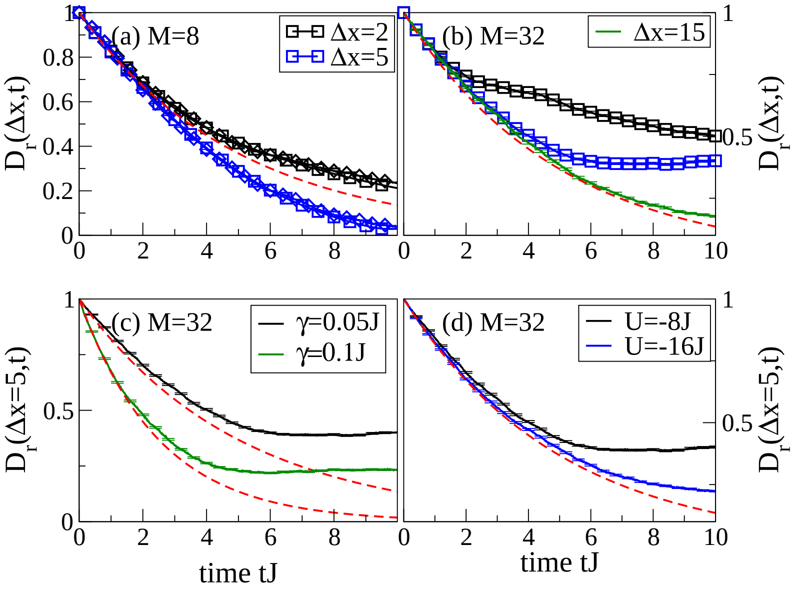

FIGURE 5.7: Comparison of doublon correlation obtained numerically and in perturbation theory (dashed line) in the strong attractive interaction limit, averaged over chain and rescaled by the initial value [Eq. (5.40)]. (a) Time dependence of the doublon correlation at $\Delta x = 2, 5$ for system size $M = 8$ at $U = -8J$ and $\gamma = 0.05J$. We see that the quantum trajectory results (diamonds) from tDMRG with $D = 64$ are in good agreement with the result obtained by doing exact diagonalisation (squares) using the EXPOKIT package [134] and that perturbation theory does not take into account the rebuilding of correlations destroyed by spontaneous emissions and hence underestimates the decay at short distances, but overestimates the decay at large distances. Using same line symbols in panel (b) we show the quantum trajectory results for spatial dependence for $M = 32$ at $U = -8J$ and $\gamma = 0.05J$ qualitatively similar to $M = 8$. (c) Effects of different decay rates for $M = 32$ at $U = -8J$. (d) Dependence on interaction strength for $M = 32$, $\gamma = 0.05J$. The time for which our perturbation theory is reliable scales with U. Panels (b) to (d) show tDMRG data using a bond dimension D=128 and the number of trajectories used in all of the calculations here is 528. Reprinted figure from S. Sarkar, S. Langer, J. Schachenmayer, and A. J. Daley, Phys. Rev. A, **90**, 023618, (2014) [110]

.

with the results calculated using first order time dependent perturbation theory. The perturbative result, showing an exponential decay of the doublon correlation function with a rate of 4γ, is found to be in accordance with the numerical result not only for very short time but also for time up to $\approx 2/J$. If we go to times longer than that, two different types of behaviour are found to be occurring, depending strongly on the spatial separation of the pairs. This happens due to the coherent dynamics, which is not taken into consideration in the first-order perturbation theory. For small separations (Δx), following a spontaneous emission event, the tunnelling terms induce the rebuilding of the correlations between the separated sites relatively quickly, resulting the average decay to be slower than what is expected from perturbation theory. This correlation rebuilding process requires longer time as the distance Δx between the sites is increased and therefore gets affected by higher order processes. We move to a bigger system size and show the similar plots in Fig. 5.7 (b) for $M = 32$, $U = -8J$ and $\gamma = 0.05J$, using the combination of t-DMRG methods with quantum trajectories techniques. Going to a bigger system size shows clearly the separation dependance and for large Δx the numerical results are closer to those obtained using perturbation theory. The results of varying the decay rate γ are shown in Fig. 5.7 (c), for $M = 32$ at $U = -8J$, which display the expected behaviour. The dependence on interaction strength is reported in Fig. 5.7(d) for $M = 32$ and $\gamma = 0.05J$, where the time during which perturbation theory produces reliable result was found to be scaling with U.

The result found here is inherently different from exponential decay with a rate γ, which we obtain for the single particle density matrix considering only singly occupied lattice sites. As superradiance [122] does not depend on particle number statistics, the same enhanced decay rate is predicted for bosonic pair correlations. This is consistent with the bosonic version of the perturbative result stated by Eq. (5.61). Also, here we are in a regime where the photons scattered by atoms of different states are indistinguishable which is the key origin of the superradiance in this case. This process does not change the total rate of increase in energy in spite of changing the total scattering rate. However, ongoing experiments should be able to measure the change in the correlation functions, which can be done by measuring the off-diagonal correlations of dimers by associating two particles on a specific lattice site to molecules, followed by measuring the momentum distribution of molecules.

5.6 Summary

In this chapter we have taken an open system of two species fermions in a far-detuned optical lattice setup that introduces spontaneous emissions as a decoherence channel in which the scattered photons are essentially indistinguishable. After deriving a microscopic master equation for the fermionic system we investigate the decoherence dynamics in strongly interacting regimes with perturbative approach as well as numerically. The formalism used for this derivation can easily be generalised for higher dimensions and also to group-II atoms with SU(N) magnetic order. The work in this chapter can be further continued in the directions of thermalisation problems within the lattice, e.g. thermalisation between atoms in the lowest Bloch band and those taken to higher bands due to spontaneous emissions [66], as well as many-body localised states, as will be discussed in Chapter 6.

We find that for the strongly repulsive case the magnetic order in the ground state is particularly robust against decoherence as the decay rate is suppressed by a factor proportional to the population in doubly occupied sites. This is due to the fact that the spontaneously emitted photons are unable to distinguish the two different spins and can only detect the difference in the total number of particles at each site. This is encouraging from an experimental point of view in the context of detecting magnetic order. There is a stark contrast which is presented by the strongly attractive case. Here the ground state is mostly made up by dimers which dynamically exhibit a decay rate enhanced by superradiance. This means it would be advantageous to use a blue detuned lattice over a red detuned lattice as the spontaneous emission rate is much lower in the former case.

Chapter 6

Light scattering and state localisation with fermions in disordered optical lattices

6.1 Introduction

As discussed in previous chapters, decoherence for atoms in optical lattices due to light scattering can be understood and controlled on a microscopic level. Our work presented in Chapter 5 deals specifically with this issue and provides a theoretical model for this particular experimental situation. In this chapter we discuss the application of this theoretical framework in a recent experiment that was carried out to study the effect of spontaneous emissions in a system realised with ultracold two-species fermions in optical lattices, which exhibit persistent

---

This work is taken in part from the publication *Signatures of many-body localization in a controlled open quantum system*, H. P. Lüschen, P. Bordia, S. S. Hodgman, M.Schreiber, S. Sarkar, A.J. Daley, M. H. Fischer, E. Altman, I. Bloch, and U. Schneider, Phys. Rev. X, **7**, 011034, (2017). The author of this thesis contributed the full analytical and numerical studies for light scattering from a single atom, and the resulting understanding of the atomic physics, that assisted in the design and the interpretation of the experiment, and was covered in details in the appendices of the article.

many-body localisation (MBL). The work was performed in collaboration with an experimental team led by Immanuel Bloch and Ulrich Schneider. A peer reviewed version of our work can be found in Physical Review X, **7**, 011034 (2017), titled "Signatures of Many-Body Localization in a Controlled Open Quantum System" [139]. In this chapter, in Sec. 6.2 we present a brief overview of thermalisation and many-body localisation. Sec. 6.3 presents the experimental details along with the model Hamiltonian that is realised, as well as results for the case of no decoherence. In Sec. 6.4 we focus on the fermionic atomic species that is used in the experiment (^{40}K) and compute the relevant level transition rates that lead to the calculation of the decoherence rates arising from spontaneous emission events. Sec. 6.5 shows the results and discusses the effect of decoherence on the stability of the MBL. Sec. 6.6 presents a brief summary.

6.2 Overview of many-body localisation

The notion of thermalisation is usually relevant in the context of a system at equilibrium with an external reservoir. However the expansion of the definition thermalisation for closed systems is also of great importance for many experiments. In a thermalisation process these closed systems reach a homogenised state after a sufficient amount of time. However under the right conditions, alternative possibilities exist, where a closed quantum system fails to thermalise. Many-body localised states belong to a class where local quantum correlations do not thermalise even after arbitrarily long times [57, 140–151]. In this section we will briefly discuss some of the important concepts needed to understand thermalisation and MBL.

6.2.1 Thermalisation

We start with the discussion of thermalisation in closed quantum systems. We consider a finite subsystem S to which the rest of the system acts as a bath B. With D being the total number of degrees of freedoms of the whole system, the density operator for the full system $\rho_D(t)$ evolves under the total Hamiltonian H_D (usually consisting of local operators) according to $i\hbar\dot{\rho}_D(t) = [H_D, \rho_D(t)]$. Now to define a thermal equilibrium, the thermodynamic limit is taken by increasing D, which is done by adding more degrees of freedoms to B while keeping S fixed. Using the canonical ensemble one can define an equilibrium density operator at temperature T by, $\rho_D^{eq} = e^{-H_D/k_BT}/\mathrm{Tr}(e^{-H_D/k_BT})$. The corresponding reduced density operator for S is given by $\rho_{S,D}^{eq} = \mathrm{Tr}_B\rho_D^{eq}$. The system is now chosen to start in a set of initial states $\{\rho_D(t=0)\}$ of which the energy distribution falls in a narrow range around the equilibrium average energy given by ρ_D^{eq}. With this choice of initial states, the system is considered to be in thermal equilibrium at temperature T if, for all choices of finite subsystems S that are described by $\rho_{S,D}(t) = \mathrm{Tr}_B\rho_D(t)$, the following condition is satisfied,

$$\lim_{D\to\infty}\lim_{t\to\infty}\rho_{S,D}(t) = \lim_{D\to\infty}\rho_{S,D}^{eq}\,, \tag{6.1}$$

when both the thermodynamic limit and long-time limit are taken together [152–154]. This definition of thermalisation also tells us although the information about the initial state of the system is not lost as the evolution is unitary, it is in general inaccessible by doing local operations on a subsystem as it gets more and more entangled with the bath with progression of time.

6.2.2 Eigenstate thermalisation hypothesis

In conventional statistical mechanics, if a system thermalises in the long time limit, it does so for all out-of-equilibrium initial states. For a closed quantum system, a general initial state $|\psi(0)\rangle$, that is not necessarily an eigenstate of the system, can be expanded in the eigenbases $\{|j\rangle\}$ i.e. $|\psi(0)\rangle = \sum_j c_j|j\rangle$. The time-evolution of this state is given by $|\psi(t)\rangle = \sum_j c_j e^{-iE_jt}|j\rangle$. The expectation value of an operator V, as a function of time, is therefore,

$$\overline{V}(t) = \sum_{j,j'} c_{j'}^* c_j e^{i(E_{j'}-E_j)t}\langle j'|V|j\rangle\,. \tag{6.2}$$

If the system thermalises, the expectation value of V in that steady state (V_{thermal}) will be the long-time average of $\overline{V}(t)$, i.e.

$$V_{\text{thermal}} = \lim_{T\to\infty} \frac{1}{T} \int dt \sum_{j,j'} c^*_{j'} c_j e^{i(E_{j'}-E_j)t} \langle j'|V|j\rangle = \sum_j |c_j|^2 \langle j|V|j\rangle \,. \tag{6.3}$$

The expectation value of an operator in the thermalised state is therefore determined by its expectation values with respect to the eigenstates and by the expansion coefficients of the initial state. According to the eigenstate thermalisation hypothesis (ETH), if the eigenstate expectation values ($\langle j|V|j\rangle$) do not fluctuate for eigenstates in a narrow energy window around the initial energy, determined by the expansion coefficients c_j, then the expectation value in the thermalised state can be described by a microcanonical ensemble [152–154]. As the unitary evolution for an initial state that is an eigenstate is trivial, i.e. $\rho_D(t) = \rho_D(t=0)$, the eigenstates stay thermalised at all times. Considering a many-body eigenstate of the full system $|n\rangle$ that correspond to a equilibrium temperature T_n under ETH, in thermodynamic limit we have $\rho_D^{eq} = \rho_{S,D} = \text{Tr}_B|n\rangle\langle n|$. In this case the bipartite entanglement between S and B, given by the von Neumann entropy, $S_{\text{vN}} = -\text{Tr}(\rho_{S,D}\log_2\rho_{S,D})$, is also the thermal entropy of S which is proportional to its volume for non-zero T_n.

6.2.3 Single-particle localisation

An interesting class of systems where quantum thermalisation does not occur and ETH is violated by the many-body eigenstates are Anderson localised systems. The case of single particle localisation, introduced by Anderson [155], can be essentially illustrated with the help of a tight-binding Hamiltonian describing a single particle on an infinite lattice with next-neighbour tunnelling J and random onsite interaction U_i at site i [147],

$$H = -J \sum_{<ij>} \left(c_i^\dagger c_j + \text{h.c.} \right) + \sum_i U_i c_i^\dagger c_i \,. \tag{6.4}$$

The random potential U_i can be chosen from a range $[-W/2, W/2]$ with the width W as a measure of the strength of the disorder. All the eigenstates of this Hamiltonian in 1D and 2D are exponentially localised i.e. the wavefunctions have an asymptotic form $\psi_n(\boldsymbol{r}) \sim \exp(-|\boldsymbol{r} - \boldsymbol{r}_n|/\xi)$, localised around the position $\boldsymbol{r}_n$, where the localisation length ξ depends on the disorder strength and energy. In three or more dimensions for weak enough disorder the eigenstates give rise to extended wavefunctions which have asymptotic form of $\sim 1/\sqrt{V}$, where V is the volume.

6.2.4 Many-body localisation

Localisation in the single particle scenario can also be expanded to the case of multiple interacting particles, giving rise to MBL. One can illustrate this in terms of a spin model [144],

$$H = J \sum_{<ij>} \boldsymbol{\sigma}_i \cdot \boldsymbol{\sigma}_j + \sum_i h_i \sigma_i^z \,, \tag{6.5}$$

where J is the nearest neighbour interaction and h_i is the onsite magnetic field, chosen from a random distribution with width W. A single particle localisation is said to be observed with this model if an initial state with a single spin up at a particular site while all other spins are down can be preserved in the system memory by the existence of a finite probability of having the spin up at that site in the long time limit . In the many-body case the eigenstates show localisation for high values of disorder which can be shown using perturbation theory [140]. Even for smaller values of disorder where perturbation theory is not valid, there is numerical evidence of MBL in 1D for some of the many-body eigenstates [144]. A quantum phase transition therefore occurs as disorder strength is varied where for weak disorder all the eigenstates obey ETH and for strong disorder not all eigenstates obey ETH. In addition to systems with static random disorder, systems with quasiperiodicity also show MBL where the disorder potential has a periodicity that is incommensurate with the underlying lattice [156]. We specifically consider such systems in this chapter.

6.3 MBL experiment with cold atoms

In the case of non-interacting particles Anderson localisation has been observed in experiments for various systems [157–159], including ultracold atom experiments [160–163]. Conclusive evidence of MBL in experiments however only was presented very recently, in 2015 [57] by our collaborators for the work presented in this chapter. MBL affected by decoherence in the same physical system of two species fermions with the same experimental techniques in the presence of a controlled source of dissipation introduced by an extra laser was used for this work. In this section we will discuss the experimental setup.

6.3.1 Aubry-André model

The system Hamiltonian describing the two-species fermions in a 1D optical lattice is given by the Aubry-André model, in the presence of interactions [156, 164]:

$$\begin{aligned} H_{\mathrm{AA}} = &- J \sum_{i,\sigma} \left(c^\dagger_{i,\sigma} c_{i+1,\sigma} + \mathrm{h.c.} \right) + U \sum_i n_{i,\uparrow} n_{i,\downarrow} \\ &+ \Delta \sum_i \cos\left(2\pi\beta i + \phi\right) \left(n_{i,\uparrow} + n_{i,\downarrow}\right) , \end{aligned} \tag{6.6}$$

which essentially is a two-species, single band Fermi-Hubbard Hamiltonian, as discussed in the previous chapter, with a quasi-random disorder potential. As before, J is the tunnelling rate, U is the onsite interaction energy with $c_{i,\sigma}(c^\dagger_{i,\sigma})$ as annihilating (creating) a fermion at i-th site with spin index $\sigma \in \{\uparrow, \downarrow\}$ and obeying the anti-commutation relation $\left\{ c_{i,\sigma}, c^\dagger_{j,\sigma'} \right\} = \delta_{i,j} \delta_{\sigma,\sigma'}$. The disorder potential with disorder strength Δ is added by introducing an incommensurate lattice, where β is the ratio of the lattice constants and ϕ is a phase offset.

This Aubry-André model was originally introduced in the context of showing single particle localisation with quasiperiodicity instead of static random disorder. For the single particle version of the Hamiltonian in Eq. (6.6) with periodic boundary condition and irrational β it can be mathematically shown for zero phase offset to have a phase transition at $\Delta = 2J$ [164, 165]. All single particle eigenstates are spatially localised for $\Delta > 2J$ and spatially extended for $\Delta < 2J$. This was checked in the experimental setup we are working with on this chapter [57]. Numerical evidence of MBL with this model was established in Ref. [156] which opened up the possibility to realise it in cold atom experiments.

6.3.2 Experimental details

The two species fermions are realised in the experiments with ^{40}K atoms with the two lowest hyperfine states as the two spin states, namely, $|F, m_F\rangle = |9/2, -9/2\rangle \equiv |\downarrow\rangle$, and $|F, m_F\rangle = |9/2, -7/2\rangle \equiv |\uparrow\rangle$. After the cooling sequence [166] a two component degenerate Fermi gas is formed with equal mixtures of these two states at an initial temperature of $0.15T_F$ where T_F is the Fermi temperature. The quasi one-dimensional lattice consists of two deep orthogonal lattices (say, along y and z directions) with wavelength $\lambda_o = 738.2$ nm and depth $V_o = 36E_{Ro}$ and the primary, *short* lattice along x direction with $\lambda_p = 532.2$ nm and depth $V_p = 8E_{Rp}$. Here $E_{R\text{lat}}$ stands for the recoil energy corresponding to the lattice laser with wavelength λ_{lat}. The disorder potential in the Aubry-André model is realised by superimposing the primary lattice with an disorder lattice with incommensurate wavelength $\lambda_d = 738.2$ nm and $V_d = s_d E_{Rd}$. Here s_d gives the relative strength of the disorder potential with $\Delta \approx 6.67 s_d J$ where J in this experiment was set around $500h$ Hz. While the lattice depths and relative phases set the values of J, Δ and ϕ, the onsite interaction U is tuned via magnetic Feshbach resonance around 202.1 G. The relative wavelength gives the incommensurate ratio, $\beta = \lambda_p/\lambda_d = 532.2/738.2 \approx 0.721$. The controlled dissipation in this system is introduced by applying a scattering laser pulse that is π-polarised and is detuned below the D_2 line of ^{40}K by 1.3 GHz. To be more precise the scattering laser wavelength λ_s is chosen such that it is blue detuned by 24 MHz to the transition between $F = 7/2$ in the $S_{1/2}$ level and $F = 9/2$ in the $P_{3/2}$ level. We will discuss in detail the atomic structure and the dissipation channels due to photon scattering in the next section.

The initial state of the system is chosen to be a charge density wave with particles only in the even sites. This state is prepared with the help of a *long* lattice with wavelength $\lambda_l = 2\lambda_p$ superimposed with the short lattice to create a tilted superlattice that results in all the particles loading on the even sites. The long lattice is then switched off during the desired evolution time in the experiments. The observable used for all the measurements is the imbalance $\mathcal{I}$ between the total atom numbers on even and odd sites, N_e and N_o respectively, and is defined as $\mathcal{I} = (N_e - N_o)/(N_e + N_o)$. The initial value is quite close to unity. At the end of the experiment the populations on the even and odd sites are measured using a superlattice band-mapping technique.

6.3.3 Result without decoherence

The imbalance $\mathcal{I}$ is tracked with time for different values of U and Δ. In the absence of the scattering laser, the coherent dynamics shows the following behaviour. For short times there is a fast decay of $\mathcal{I}$ followed by damped oscillatory dynamics which approach a stationary value at longer times. In the absence of disorder ($\Delta = 0$) it is an ergodic system and $\mathcal{I}$ is expected to approach zero. As the disorder is increased the ergodic behaviour dramatically ceases to exist and the imbalance approaches a finite stationary value at long times. This establishes the signature of MBL persisting in the system. The stationary value increases with increasing value of Δ/J. In the non-interacting case the transition between the ergodic and the localised phase happens at $\Delta/J = 2$. In presence of a moderate interaction the degree of localisation slightly reduces and therefore the transition happens at a higher value of Δ/J. For strong interactions however the effective tunnelling rate decreases as the initial state can be thought of consisting of doublons that tunnel with a second-order rate $\sim J^2/U$ which is much smaller than J. The transition therefore happens at smaller values of Δ/J.

Coupling to a thermal environment gives rise to decoherence effects which are expected to destroy the MBL behaviour due to the relaxation of local observables. To study this open quantum system we would like to write a master equation for the system density operator in the Lindblad form as was done in the previous chapters. In the next section we discuss the various decay channels in the ^{40}K atomic system due to spontaneous emission in the presence of a scattering laser.

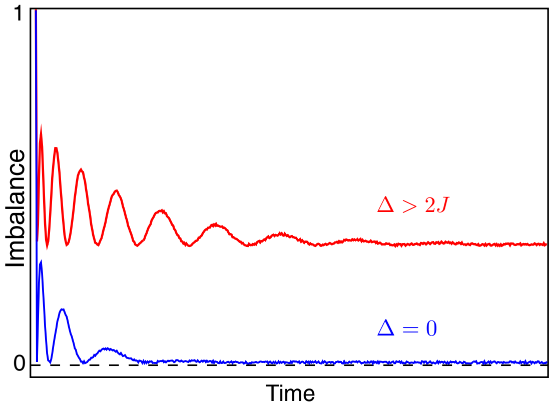

FIGURE 6.1: Schematic diagram showing the imbalance $\mathcal{I}$ as a function of time (adapted from [57]). In the initial state $\mathcal{I}$ is 1 and in absence of disorder it relaxes to 0 (Blue line). For strong enough disorder ($\Delta > 2J$) the system fails to thermalise and $\mathcal{I}$ approaches a positive stationary value at long times (red line).

6.4 Level scheme in ^{40}K and scattering bursts

For the ^{40}K atoms in an optical lattice and driven by a dedicated detuned laser, spontaneous emission events can give rise to two dissipative processes. The atom, initially in a localised superposition of Wannier states becomes localised on a length scale set by the scattered photon's wavenumber, which dephases the coherent superposition to an incoherent mixture of single Wannier states [65, 110]. Also the atom can be excited to a higher band, which can result in a loss process due to weak trapping and higher tunnelling rates in higher bands. The total scattering rate γ therefore consists of two parts, rate of dephasing γ_{dp}, and rate of excitations to higher bands γ_{ex}. In this section we provide the details of the calculations that lead to the determination of the fractional loss to excited bands i.e. $\gamma_{\mathrm{ex}}/\gamma_{\mathrm{dp}}$.

To do so we first focus on the hyperfine splitting of the fine-structure levels of ^{40}K relevant to the experiment. In spectroscopic notation the fine-structure is given by $^2S_{1/2}$ as the ground level, $^2P_{1/2}$ as the first excited level or D_1 transition and $^2P_{3/2}$ as the next excited level or D_2 transition. The hyperfine Hamiltonian for

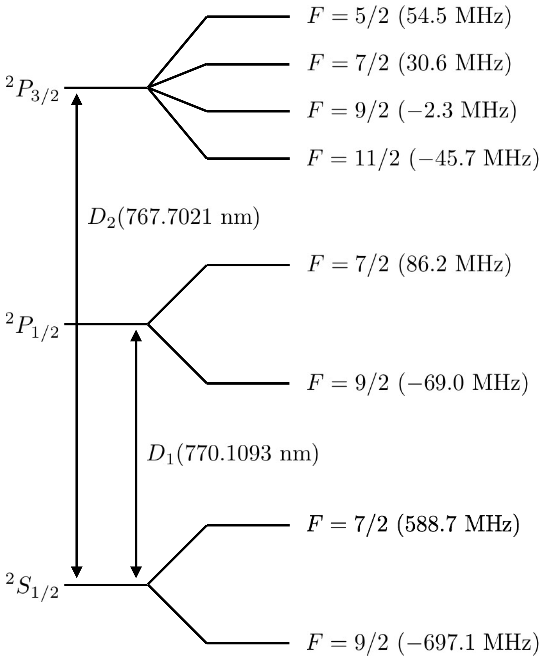

FIGURE 6.2: Schematic diagram showing the lowest hyperfine manifolds of ^{40}K in the absence of magnetic field (adapted from [167]). In the context of the experiment we focus on the S and D_2 manifold.

^{40}K is added by taking the nuclear spin into account ($I = 4$),

$$H_{\text{hfs}} = A_{\text{hfs}}\mathbf{I} \cdot \mathbf{J} + \frac{B}{\hbar}\left(\mu_B g_J m_J + \mu_N g_I m_I\right) , \tag{6.7}$$

which, upon diagonalisation in the absence of B-field, gives rise to the hyperfine structure shown in Fig. 6.2. The constants appearing in the Hamiltonian can be found in Ref. [167]. From an experimental point of view, we will look at a situation where the π polarised laser is blue detuned by 24 MHz to the transition between $F = 7/2$ in the $^2S_{1/2}$ level and $F = 9/2$ in the $^2P_{3/2}$ level and at a magnetic field around 200G. As the D_1 level is far away we do not take its effect into account. For the experimentally relevant lowest two states in the $^2S_{1/2}$ level i.e. $|F, m_F\rangle = |9/2, -9/2\rangle \equiv |\downarrow\rangle$, and $|F, m_F\rangle = |9/2, -7/2\rangle \equiv |\uparrow\rangle$, we compute the transition rates and determine the relative probabilities to return to different spin states upon de-excitation. Recalling the general scheme used for calculating decay rates in a multilevel atom summarised in the previous chapter (Sec. 5.2) we compute these different transition rates between atomic levels of ^{40}K numerically for arbitrary magnetic field strengths. Before tabulating the interesting findings, we discuss briefly the behaviour of the transition rates for limiting values of the magnetic field.

Discussion on the low field behaviour

For small magnetic fields $|F, m_F\rangle$ is the suitable choice of basis to work with. We look at the situation where the atom starts out in the lowest energy state in the S manifold i.e. at $|9/2, -9/2\rangle_S$, gets excited to the D_2 manifold and subsequently decays back to any of the allowed states in the S manifold. For a π polarised laser, the excited state is given by

$$
\begin{aligned}
|e_\pi\rangle \propto\ & \frac{\left\langle \left(\frac{11}{2}, -\frac{9}{2}\right) |Y_1^0| \left(\frac{9}{2}, -\frac{9}{2}\right) \right\rangle}{1240} \left| \frac{11}{2}, -\frac{9}{2} \right\rangle_{D_2} + \frac{\left\langle \left(\frac{9}{2}, -\frac{9}{2}\right) |Y_1^0| \left(\frac{9}{2}, -\frac{9}{2}\right) \right\rangle}{1240 + 43.4} \left| \frac{9}{2}, -\frac{9}{2} \right\rangle_{D_2} \\
=\ & \frac{\sqrt{\frac{2}{33}}}{1240} \left| \frac{11}{2}, -\frac{9}{2} \right\rangle_{D_2} + \frac{\frac{4}{3\sqrt{11}}}{1240 + 43.4} \left| \frac{9}{2}, -\frac{9}{2} \right\rangle_{D_2} .
\end{aligned}
\tag{6.8}
$$

Now $|e_\pi\rangle$ can decay to $|9/2, -9/2\rangle_S$, causing no spin flip, and also can decay to $|9/2, -7/2\rangle_S$ or $|7/2, -7/2\rangle_S$ which result in spin flips. We can compute the relative probabilities

$$
\frac{\text{probability of spin flip}}{\text{probability of no spin flip}} = \frac{\left|\left\langle \left(\frac{9}{2}, -\frac{7}{2}\right)_S |Y_1^1| e_\pi \right\rangle\right|^2 + \left|\left\langle \left(\frac{7}{2}, -\frac{7}{2}\right)_S |Y_1^1| e_\pi \right\rangle\right|^2}{\left|\left\langle \left(\frac{9}{2}, -\frac{9}{2}\right)_S |Y_1^0| e_\pi \right\rangle\right|^2} \approx \frac{1}{2} .
\tag{6.9}
$$

Discussion on strong field behaviour

In the presence of a strong magnetic field the degeneracy in the hyperfine manifold is broken and the suitable choice of basis to work with is $|J, m_J; I, m_I\rangle$. We again look at the situation where the atom starts at the lowest energy state in S manifold i.e. at $|1/2, -1/2; 4, -4\rangle_S$, is excited to the D_2 manifold and subsequently decays back to any of the allowed states in the S manifold. If the laser is π polarised then the excited state is $|3/2, -1/2; 4, -4\rangle_{D_2}$ and the ratio of transition rates of coming back to the other possible state (i.e. $|1/2, 1/2; 4, -4\rangle_S$) to that of coming back to the starting state (i.e. $|1/2, -1/2; 4, -4\rangle_S$) is basically the ratio of squares of the respective Wigner $3j$ functions (see Eq. (5.2)), and therefore,

$$\frac{\text{probability of spin flip}}{\text{probability of no spin flip}} = \left| \frac{\begin{pmatrix} \frac{3}{2} & 1 & \frac{1}{2} \\ -\frac{1}{2} & 1 & -\frac{1}{2} \end{pmatrix}}{\begin{pmatrix} \frac{3}{2} & 1 & \frac{1}{2} \\ -\frac{1}{2} & 0 & \frac{1}{2} \end{pmatrix}} \right|^2 = \frac{1}{2}\,. \tag{6.10}$$

Therefore we see for the lowest energy ground state ($|\downarrow\rangle$), changing the magnetic field does not have any significant effect on the relative spin flip rates for a π polarised laser. This result also holds for the second lowest state in the S manifold ($|\uparrow\rangle$). We check this by numerically diagonalising the Hamiltonian in Eq. (6.7) for a range of B-field and computing the relative spin flip rates. Therefore we can deduce that for both the lowest energy states in the $F = 9/2$ ground state manifold, in a spontaneous emission event, the probability to come back to the starting state is almost 2/3 and the probability to return to other spin states is almost 1/3. Investigating the nature of the flipped spin states we find that there is only one state in the $F = 7/2$ ground state manifold that the spin flip dominantly leads to for the magnetic field regime we work in. This is an expected behaviour as for these values of magnetic fields the atomic level structure is close to the Paschen-Back regime and therefore m_J and m_I are good quantum numbers. As the coupling to the nuclear spin is much smaller than the coupling to electron spin, the transition between different m_I states is suppressed. The spin flip for the $|\downarrow\rangle$ state therefore happens to the highest state in the $F = 7/2$ ground state manifold ($|1/2, 1/2; 4, -4\rangle_S$). Due to weak coupling to the nuclear spin there is only 4% chance of returning to another m_I state in the case of a spin flip. Another interesting experimental situation occurs in this case where the spin flipped state in the $F = 7/2$ ground state manifold is found to be resonantly coupled with a particular state in the $F = 7/2$ D_2 manifold which is the highest energy state in that particular manifold. The atom therefore will be quickly excited to $F = 7/2$ in the D_2 manifold. Computing the transition rates from this excited states again show a probability close to 2/3 to return to the highest state in the $F = 7/2$ ground state manifold and a probability close to 1/3 to return to the lowest energy ground state ($|\downarrow\rangle$).

All the results presented above are also applicable to the second-lowest energy state in the S manifold ($|\uparrow\rangle$). In this case also a spontaneous emission event returns the atom with probability close to 2/3 to the starting state and with probability close to 1/3 to a spin-flipped state which is the second highest state in the $F = 7/2$ in ground state manifold ($|1/2, 1/2; 4, -3\rangle_S$). There is although around 10% chance of flipping into another state due to weak coupling to nuclear spin. The spin flipped state is resonantly coupled to the second highest state in the $F = 7/2$ D_2 manifold and would be readily excited to it. The probabilities to come back to the second highest state in the $F = 7/2$ ground state manifold and to the second lowest energy ground state ($|\uparrow\rangle$) are close to 2/3 and 1/3 respectively.

These findings are summarised in Fig. 6.2. The resonant coupling between the spin flipped state and $F = 7/2$ in the D_2 manifold results in multiple photons being scattered on a very short time-scale. We define a *scattering burst* as the following sequence of photon absorptions and reemissions: the atom starts in the $F = 9/2$ ground state manifold and following absorption of a scattering laser photon decays, to the same state with probability 2/3 and to $F = 7/2$ in ground state manifold with probability 1/3. The resonant coupling causes multiple photon scattering in quick succession until all the population is back in the starting state in the $F = 9/2$ ground state manifold, ending the scattering burst. This full event of scattering can essentially be taken as a single scattering event as the timescale of the resonant scattering events are much smaller compared to the tunnelling time.

6.4.1 Band excitation for single photon emission

Along with the dephasing mechanism, a spontaneous emission event can introduce atom loss in the system via excitation to higher bands. In order to compute the atom excitation rate in a scattering burst event we first discuss a single photon process where the atomic population transfer is computed in a spontaneous emission that follows a stimulated absorption. Although in the experiment the 3D lattice is inseparable, we take them to be mutually orthogonal to numerically

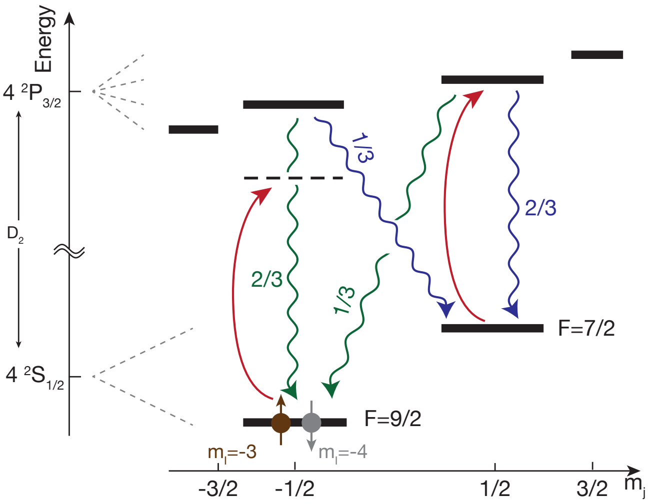

FIGURE 6.3: Schematics of the scattering burst for ^{40}K. In the presence of a π-polarised detuned scattering laser and in the Paschen-Back regime for the atomic levels, the atom in the lower lying $F = 9/2$ manifold is virtually excited (red line). This is followed by reemission (green line) back to the starting state and to the lower lying $F = 7/2$ level which is resonantly connected to the upper (D_2) lying $F = 7/2$ level. This leads to resonant multi-photon scattering (blue line) until the atom is back in the ground state manifold. Reprinted figure from H. Lüschen et. al, Phys. Rev. X, **7**, 011034, (2017) [139].

compute the Wannier functions along the three axes. These separately formed bands are then combined to approximate the tabulations of the bands in the actual lattice. This approximation becomes worse as we go to higher bands but should give a decent estimation of the atomic excitation rate as long as we consider only a few of the lower bands. Also, as the disorder lattice potential is weak compared to the primary lattice, we can neglect its presence, assuming its influence on the band structure to be very small. Using the experimental parameters reported in the previous section we calculate the band structure and Wannier functions for the lattice system. We assume that the atom in a particular lattice site in band (j_x, j_y, j_z) in the three dimensional case is represented by the Wannier wavefunction $|w_{j_x}, w_{j_y}, w_{j_z}\rangle$ around that lattice site. Here we make a simplification by using a Wannier state for a starting state where we should be using a localised function given by a superposition of several Wannier states. This might ask for some corrections but carrying out these calculations with simple

	(j_x, j_y, j_z) =(0,0,0)	(1,0,0)	(0,1,0)	(0,0,1)	(2,0,0)
(i_x, i_y, i_z) =(0,0,0)	0.823	0.103	0.023	0.023	0.016
(1,0,0)	0.103	0.582	0.003	0.003	0.229
(0,1,0)	0.023	0.003	0.772	0.000	0.000
(0,0,1)	0.023	0.003	0.000	0.772	0.000
(2,0,0)	0.016	0.229	0.000	0.000	0.406
higher	0.011	0.080	0.201	0.201	0.348

TABLE 6.1: Here we show the probability table to start in band (j_x, j_y, j_z) and coming back to band (i_x, i_y, i_z) (Eq. (6.11)) following the absorption of a photon with wave number k_ν along the x-direction and subsequent spontaneous emission in any direction uniformly. The index (0,0,0) refers to the lowest band and higher indices to the i-th (j-th) excited band along the given spatial direction.

harmonic oscillator wavefunctions does not make a drastic change in the end result. For the coupling between bands, the probability to start in band (j_x, j_y, j_z) and coming back to band (i_x, i_y, i_z) following the absorption of a photon with wave number k_ν along x-direction and subsequent spontaneous emission in any direction uniformly,

$$P_{i,j} = \sum_{\boldsymbol{r}\in\text{lattice}} \int_{k_\nu \text{ sphere}} k_\nu^2 \sin\theta d\theta d\phi \left|\left\langle w_{i_x}, w_{i_y}, w_{i_z} \right| e^{-i\boldsymbol{k}\cdot\boldsymbol{r}} e^{ik_\nu x} \left| w_{j_x}, w_{j_y}, w_{j_z} \right\rangle\right|^2 . \tag{6.11}$$

Based on the definition, for a particular j, the sum of $P_{i,j}$-s over all i values and over an infinite lattice with the starting state at the middle of the lattice should be $4\pi k_\nu^2$ (k_ν is normalised by the lattice constant in x-direction). As we make a cut-off at a certain n_{band}, we have to take care of the fact that there is a loss rate to the bands that we do not consider. We are allowed to do this as the atoms in the higher bands are not trapped. To imply this we renormalise the $P_{i,j}$ matrix by demanding that the sum of the each column is $4\pi k_\nu^2$. Following this $P_{n_{\text{band}}+1,j}$ is added by hand that takes care of transition to all the higher bands and upon division by $4\pi k_\nu^2$ we obtain $\sum_i P_{i,j} = 1$. The result of these calculations is shown in Table 6.1. The symmetry of the orthogonal lattices result in equal excitation probabilities of population transfer and as they are deeper lattices the probability values are also lower.

6.4.2 Band excitation for scattering bursts

The calculation of the population transfer probability to higher bands in the single photon process paves the way to calculate the average band excitation probabilities in a scattering burst. As explained before, here the atom in the $F = 9/2$ ground state manifold at first absorbs a photon from the scattering laser and emits a (small) n number of photons due to resonant coupling between $F = 7/2$ in ground state and D_2 manifold with $n \in [0, 1, 2, 3, ...]$ before returning to the starting state in the $F = 9/2$ ground state manifold. The band excitation probabilities therefore explicitly depends on number of resonantly emitted photons, n. We compute an average band excitation probability considering all possible values of n, properly weighed by the probability factor of scattering n resonant photons, which is given by $P(n) = (1/3).(2/3)^{n-1}$. As this geometric sequence approaches 0 quickly we see the band excitation probabilities converges only after a few photon emissions with the limiting value ($n \to \infty$) giving the average value. With this ab-initio calculation we obtain the relative probability of population transfer in excited bands in a spontaneous emission event to be around 30%, as can be seen in Fig. 6.4. This gives the ratio $\gamma_{\mathrm{dp}}/\gamma_{\mathrm{ex}} \approx 2.3$, which is used for further calculations including a potential numerical time evolution of the full master equation of the atomic density operator in the Lindblad form,

$$\begin{aligned}\dot{\rho} = -i[H_{\mathrm{AA}}, \rho] &+ \gamma_{\mathrm{dp}} \sum_i \left(n_i \rho n_i - \frac{1}{2} n_i n_i \rho - \frac{1}{2} \rho n_i n_i \right) \\ &+ \gamma_{\mathrm{ex}} \sum_{i,\sigma} \left(c_{i,\sigma} \rho c_{i,\sigma}^\dagger - \frac{1}{2} c_{i,\sigma}^\dagger c_{i,\sigma} \rho - \frac{1}{2} \rho c_{i,\sigma}^\dagger c_{i,\sigma} \right) , \end{aligned} \tag{6.12}$$

where the jump operators n_i and $c_{i,\sigma}$ introduce the two dissipative processes dephasing and atom loss by band excitation respectively. In the numerical work done for this work, however, only the dephasing mechanism could be handled in DMRG calculations using TEBD framework.

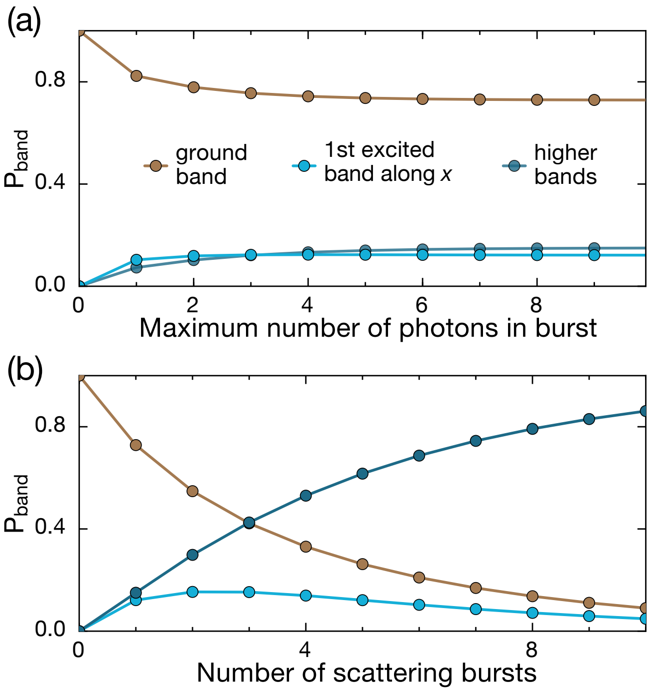

FIGURE 6.4: Band excitation probabilities in the lowest and 1st excited band, and the cumulative probabilities in all the higher bands (i.e. from 2nd excited band onwards). (a) Probabilities calculated in the faster timescale are shown here with number of resonant photons n, until steady values are reached which are the average band excitation probabilities. (b) Properly weighted band excitation probabilities as a function of number of scattering bursts, i.e. in the long timescale after the steady values are reached through the spontaneous emission events in the faster timescale. Reprinted figure from H. Lüschen et. al, Phys. Rev. X, **7**, 011034, (2017) [139].

6.5 Results

For different values of scattering rate γ with a moderate interaction value $U = 2J$ and a moderate disorder value $\Delta = 4J$ the imbalance $\mathcal{I}$ is shown in Fig. 6.5 as a function of time. In the absence of a scattering laser ($\gamma = 0$ case) the imbalance approaches a steady value at intermediate times as observed before [57] but in the long time limit goes to a thermalised value i.e. zero. This happens due to residual coupling with neighbouring 1D tubes in the experiment and due to off-resonant lattice photons present in the setup [150]. For finite γ values the relaxation of $\mathcal{I}$ is faster along with faster atom loss which is expected from our microscopic

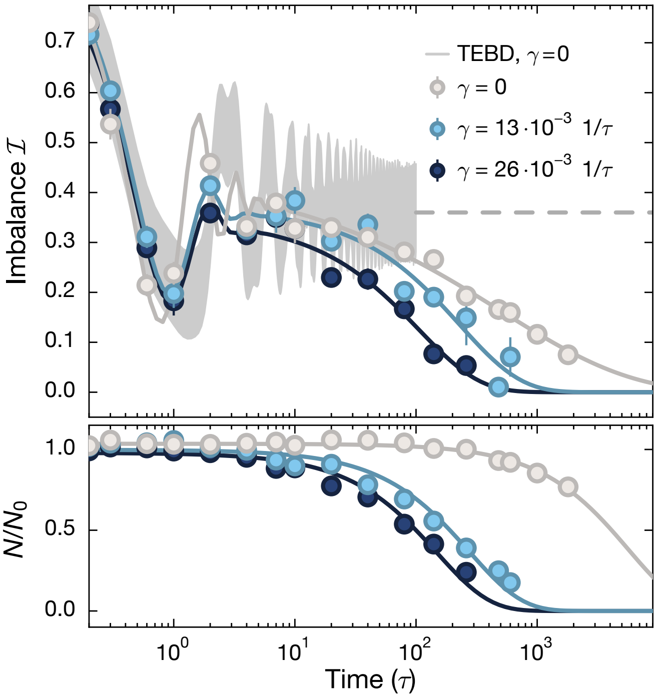

FIGURE 6.5: Imbalance $\mathcal{I}$ as a function of time in units of $\tau = \hbar/J$, in the presence of photon scattering. Upper panel: For an initial state, with fermionic atoms occupying only even sites on an optical lattice, with an additional quasirandom disorder potential with strength $\Delta = 4J$ and interaction $U = 2J$, time evolution under different scattering rates γ show faster decay of $\mathcal{I}$ for higher values of γ. The solid lines are the stretched exponential fits to the experimental data points (circles) each of which is an average over six different phase offset realisations. The grey shaded region show the TEBD calculation for no scattering (dashed line is an extrapolation of the mean stationary value) which differs from the experimental result as the numerical work does not take into account the coupling to neighbouring 1D tubes and off-resonant scattering of lattice photons present in the experiment that causes a long-time decay of $\mathcal{I}$. The lower panel shows the corresponding time evolution of the normalised atom number with simple exponentials used as fit functions. Reprinted figure from H. Lüschen et. al, Phys. Rev. X, **7**, 011034, (2017) [139].

understanding of the scattering processes discussed in the previous section. The relaxation of $\mathcal{I}$ matches the theoretical prediction of a stretched exponential decay [168, 169] of the form $e^{-(\Gamma_{\mathcal{I}} t)^{\beta}}$ with a global imbalance relaxation rate $\Gamma_{\mathcal{I}}$ and a stretching exponent β with typical fit values between 1/2 and 1. The effect of the scattering rate can be parameterised by introducing a susceptibility χ defined as $\chi = d\Gamma_{\mathcal{I}}/d\gamma$. A measure for the stability of the MBL phase in these systems

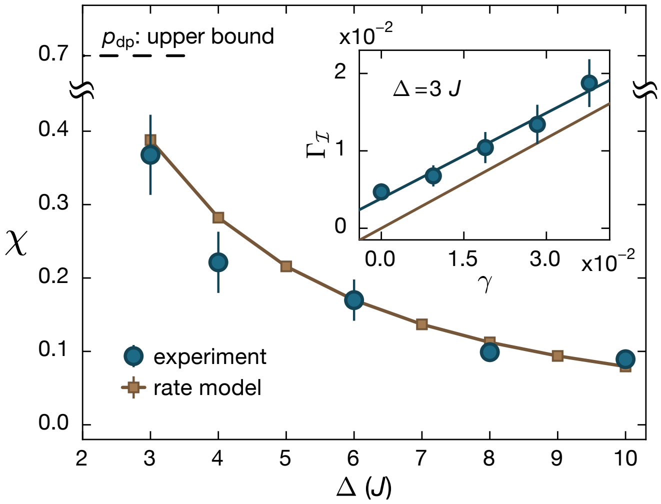

FIGURE 6.6: Susceptibility with disorder strength in the non-interacting system: The upper bound of the susceptibility given by $p_{\mathrm{dp}} = \gamma_{\mathrm{dp}}/\gamma$ is shown by the black dashed line. The experimental data (circle) is compared to the predictions of a rate model (brown line) introduced in [169]. In the inset the imbalance relaxation rate $\Gamma_{\mathcal{I}}$ is plotted with scattering rate γ. The slope that gives the susceptibility χ is similar for the experimental result and the rate model. A constant experimental background decay Γ_{bg} is the reason for the offset. Reprinted figure from H. Lüschen et. al, Phys. Rev. X, **7**, 011034, (2017) [139].

against the dissipative effects due to the photon scattering can then be given by $1/\chi$. In the following we discuss the behaviour of this susceptibility for the non-interacting and interacting system respectively.

6.5.1 Non-interacting case

In the non-interacting case we look at the localised phase that happens for $\Delta > 2J$. As shown in Fig. 6.6 the susceptibility χ significantly goes down as the disorder strength Δ increases. This can be intuitively understood by considering a single particle in a localised phase around at a particular site. For large Δ the deep localisation allows one to think of the state of the particle as a Wannier state, which upon spontaneous emission gets hardly affected. The excitations to higher bands does not in general have any effect in the non-interacting case as they are equally probable to occur at any site. The susceptibility however

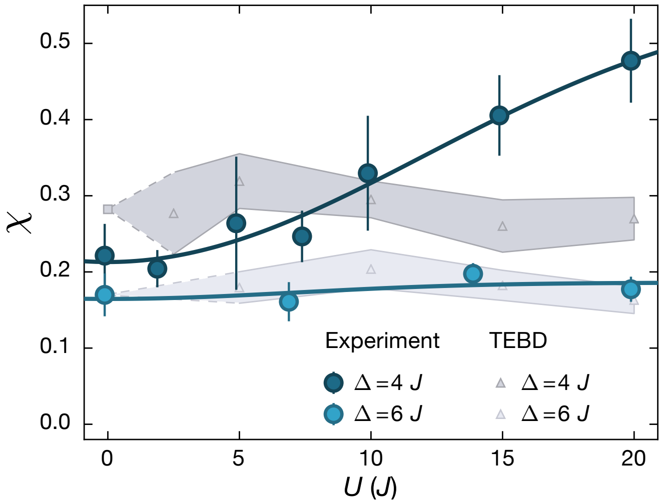

FIGURE 6.7: Susceptibilities in the interacting system for different disorder strengths. The experimental results (circles) are compared to numerical calculations using TEBD simulations that do not include particle loss (triangles). The grey shaded region indicates the statistical uncertainty of the TEBD results and the solid lines serve as guides to the eye. The squares are theoretical values for the non-interacting case calculated with the rate model [169]. The interaction has a significant effect on the susceptibility deep in the localised phase ($\Delta = 6J$) but a very weak effect as one moves close to phase transition ($\Delta = 4J$). Reprinted figure from H. Lüschen et. al, Phys. Rev. X, **7**, 011034, (2017) [139].

increases as Δ is decreased as the moderate localisation of a particle implies finite overlap with neighbouring sites which can result in shifting it away after an event of spontaneous emission. The susceptibility has thus an upper limit which would occur close to the phase transition where the localisation length diverges, implying that each dephasing event can shift the particle to an even or odd site with same probability. The decay rate of imbalance is therefore $\gamma_{\rm dp}$ and the upper limit of χ is $\gamma_{\rm dp}/\gamma$. This is experimentally not possible to check though as near the phase transition the localisation length is divergent and the imbalance is zero.

6.5.2 Interacting case

When the particles interact they are affected by a dephasing event even in the vicinity. Atom losses also affect the sites nearby. The delocalised atoms in higher bands can interact with those in the ground bands too. For these reasons the susceptibility is expected to increase in the interacting case. Moreover, without the presence of an upper bound the susceptibility might show a diverging behaviour near the MBL transition. As we see in Fig. 6.7 though, in the deep localised phase with $\Delta = 6J$, that the interaction only has a very weak effect on χ which is expected for strong localisation. As one moves towards smaller disorder values, increasing interaction has a strong influence on χ which grows rapidly. This can only be attributed to the dissipative effects introduced by atom loss due to band excitation. A sudden change of potential caused by loss of atoms that acts on the neighbouring particles is a dephasing mechanism that reduces the imbalance and therefore makes the system more susceptible as interaction increases.

6.6 Summary

In this chapter we have applied our understanding from Chapter 5 of a two-species fermionic systems undergoing dissipative dynamics due to the presence of a detuned laser that gives rise to incoherent light scattering to a recent experiment that investigates MBL in such systems. To study the effect of the controlled coupling to an environment we look at the atomic structure of the fermionic species used in the experiment. We determine the relative decay rates due to the two decoherence processes associated with a spontaneous emission event. These are dephasing due to localisation and atom loss processes due to excitations to higher bands. These findings help us to quantify the effect of the dissipative processes in the experiment and determine the susceptibility to the scattering events. The susceptibility was found out to be not sensitive to interactions in deeply localised phases but showed a steep rise with increase in interactions near the MBL transition. Potential directions for further research on the theoretical side include devising an analytical model to capture this interesting behaviour qualitatively and optimisation of the numerical techniques to study the dynamics with atom loss processes in these problems.

Chapter 7

Entanglement in two species bosonic systems

7.1 Introduction

Recent experimental advances in the field of ultracold atoms to explore the realm of many-body physics with microscopic control of Hamiltonian parameters and the environment [7–10, 17, 18] have opened the door to realise a number of low-temperature condensed matter phenomena. The presence of impurities in these systems has been studied at length and are known to give rise to quite interesting features, such as the Kondo effect [170], induced by localised magnetic impurities, or the study of high-temperature superconductivity linked with the transport of spin impurities [171–173]. Simulating such multi-species systems in an ultracold gas experiment is feasible these days, as outlined in Chapter 2. A particularly interesting type of such experiment is where the impurity system is realised by a small number of particles loaded onto the lowest Bloch band of an optical lattice and is coupled to a Bose-Einstein condensate (BEC) [41, 174, 175]. These experiments are used to achieve a range of objectives including local non-destructive probing [35], qubit cooling [36] and creating bath-mediated long-range interaction [37]. Also, the impurity particles along with the excitations created due to the coupling can demonstrate polaronic behaviour [30, 38–48] in terms of an induced effective interaction [37, 49–51] and an increase in effective mass [52–54], resulting a decrease in mobility of the impurities, as quantified by a decrease in visibility in momentum distribution. In a recent experiment in the group of Dominik Schneble (SUNY at Stony Brook) this decrease in visibility was found to exceed the expected values with ^{87}Rb BEC interacting with ^{87}Rb atoms in a different hyperfine state and loaded into an one-dimensional optical lattice [176]. To possibly explain this interesting feature one can think of the minority species acting as impurities in a two-component quantum system with the majority species system acting as a reservoir. The coupling between the two systems would generate decoherence effects for individual species which cannot be dealt in a markovian treatment as we have done in the previous chapters. The effects of the decoherence should be studied in terms of the entanglement between the two species, which could enhance the decrease in visibility as seen in the experiments. In this work we therefore focus on the ground state of coupled bosonic system and try to connect the entanglement between them arising from the interaction with the decrease in visibility in the single particle momentum distribution. To achieve this we start by studying numerically a system of two number-imbalanced species of bosons in an optical lattice setup, and then move on to the experimentally relevant system of a BEC coupled with a small number of bosons in an optical lattice. Specifically, in Sec. 7.2 we look at the effects of interaction on the ground state quasi-momentum distribution in the simplest many-body case of two particles on a lattice. In Sec 7.3 we move on to the many body case where two different species of bosonic particles are loaded on an optical lattice obeying the two species Bose-Hubbard Hamiltonian in the parameter regime that can be realised in experiments. Here we also give an outline of the different numerical techniques used to compute the ground state before discussing the results. In Sec 7.4 we look at the ground state of the experimental relevant system of one impurity boson coupled to a large BEC and subsequently look at a system of two coupled and length-imbalanced optical lattices to have an analytical insight. We summarise the results of this study in Sec 7.5.

7.2 Two particles on a 1D lattice

Here we start by analysing the simple case of two similar but distinguishable bosons on a large 1D lattice [30, 177], and quantify the changes in the ground state properties as a function of the interaction strength between the bosons. In particular we choose to look at the (quasi) momentum distribution for the following reasons. For a single boson on an infinitely long lattice the lowest energy state is a definite momentum state as the Hamiltonian describing the boson only consists of the kinetic energy. The momentum distribution in this case will be a delta function at zero quasi-momentum. This is identical to the single particle momentum distribution of two non-interacting bosons. If we go to the other limit where the interactions, as opposed to being zero, are infinitely attractive, the lowest energy state is a uniform superposition of wavefunctions with the two particles on the same site, which means the particles are completely entangled in position space. The single particle density matrix for this case will then correspond to a mixed state comprising of wavefunctions localised at each lattice site. The single particle momentum distribution therefore becomes completely flat. To analyse the behaviour for arbitrary interaction strengths we have to look at the discrete Schrödinger equation for two bosons moving on a infinitely long 1D lattice (the lattice constant is unity and $\hbar = 1$) with individual tunnelling rate J and a contact interaction U, namely,

$$\left[-J\left(\tilde{\triangle}_x + \tilde{\triangle}_y\right) + U\delta_{x,y}\right]\psi(x,y) = E\psi(x,y)\,, \tag{7.1}$$

where $\psi(x,y)$ is defined as the two-particle wavefunction with x and y being site indices. The difference operator is defined as

$$\tilde{\triangle}_x\psi(x,y) = \psi(x+1,y) + \psi(x-1,y) - 2\psi(x,y)\,. \tag{7.2}$$

We can turn this into a single particle problem by rewriting the equation in the centre of mass coordinates $R = (x+y)/2$ and the relative coordinates r defined with periodic boundary conditions such that its value can only go from $-L$ to L which are also the indices of the lattice sites. We then use an ansatz where the centre of mass moves with a constant momentum K (as there is no external potential), and a relative wavefunction $\psi_K(r)$ carries all the necessary information:

$$\psi(x,y) = \sqrt{\frac{1}{M}} e^{iKR} \psi_K(r) \,, \tag{7.3}$$

where total number of sites, $M = 2L + 1$. With a redefined tunnelling rate $J_K = 2J\cos(K/2)$ and K-mode energy E_K we now have

$$-J_K\left(\psi_K(r+1) + \psi_K(r-1)\right) + U\delta_{r,0}\psi_K(r) = \left(E_K - 4J\right)\psi_K(r) \,. \tag{7.4}$$

In the attractive case ($U < 0$) we start with a trial symmetric (about $r = 0$) wavefunction $\psi_K(r) = A_K e^{-ik|r|} + B_K e^{ik|r|}$. Plugging this in Eq. (7.4) for nonzero r yields, $\cos k = (4J - E_K)/2J_K$, absolute value of which is always bigger than 1 as the condition for a bound solution is $E_K < 0$. Therefore we take $k = iq$. Using the continuity at $r = 0$ and boundedness of the solution we get $\psi_K = A_K e^{-q|r|}$ with energy $E_K = -\sqrt{U^2 + 16J^2\cos^2 K/2} + 4J$. Now K is set to be zero since we are looking for the lowest energy state. Using normalisation condition we now obtain the following relative wavefunction for the lowest energy bound state,

$$\psi(r) = \sqrt{\frac{1 - e^{-2q}}{1 + e^{-2q} - 2e^{-q(M+1)}}} e^{-q|r|} \,, \tag{7.5}$$

where q is real and is the solution of $e^{-q} = \left(\sqrt{U^2 + 16J^2} - U\right)/4J$ and the bound state energy $E = -\sqrt{U^2 + 16J^2} + 4J$.

In the repulsive case ($U > 0$) we again start with a trial symmetric (about $r = 0$) wavefunction $\psi(r) = Ae^{-ik|r|} + Be^{ik|r|}$. The lowest energy state can be computed making use of the continuity of the wavefunction at $r = 0$ and the periodic boundary conditions. The normalised relative wavefunction is then given by,

$$\psi(r) = \frac{e^{-ik|r|} + e^{-i2kL}e^{ik|r|}}{\sqrt{2\left(M + \cos\left(2kL\right)\right) + 2\mathrm{Re}\left(\frac{e^{-i(M+1)k} - e^{-i2Mk}}{1 - e^{-i2k}}\right)}} \,, \tag{7.6}$$

where k is given by $\tan(kL+\pi/2)+(4J/U)\sin k=0$. The ground state energy $E=4J(1-\cos k)$.

From this we can look at the limiting values of the single particle von Neumann entropy $S_{\mathrm{vN}}=-\mathrm{Tr}(\rho_1\log_2\rho_1)$ where ρ_1 is the single particle reduced density matrix. For the attractive case, as $U\to-\infty$, we have $e^q\to 0$ and therefore $\psi(x,y)\to\sqrt{1/M}\delta_{x,y}$. Therefore we can show that $S_{\mathrm{vN}}\to\log_2 M$ which is expected as this is the case of a maximally entangled state. For the repulsive case as $U\to\infty$, we have $k\to\pi/2L$ and $\psi(x,y)\to\sqrt{1/M}\sin(\pi|x-y|/2L)$. In this case we have

$$\begin{aligned}S_{\mathrm{vN}}\to-\sum_{x,x'}&\left(\frac{1}{M}\sum_y\sin(k|x-y|)\sin(k|x'-y|)\right)\\&\log_2\left(\frac{1}{M}\sum_y\sin(k|x-y|)\sin(k|x'-y|)\right).\end{aligned}\tag{7.7}$$

Once we have the ground state wavefunction we can also compute the single particle quasi momentum distribution on a lattice of M sites

$$n_1(p)=\sum_{x,x',y}\frac{1}{M}e^{ip(x-x')}\psi^*(x,y)\psi(x',y)\,.\tag{7.8}$$

Naturally, in addition to finding analytical solutions, we can solve this problem numerically, with exact diagonalisation (ED) calculations (with periodic boundary conditions) for the two particle wavefunctions. The relative wavefunctions are shown in Fig. 7.1(a). The squares and triangles represent the ED results that match with the analytical solutions, which are the solid lines. We see that the peak of the bound pair solutions gets sharper as the interaction strength is increased. The single particle momentum distributions (computed using Eq. (7.8)) displayed in Fig. 7.1(b) show clearly the effect of interactions in this two particle system. As expected for the ground state (for $U<0$) with increasing interaction strength each particle is more likely to stay closer to the other and due to this constrained behaviour in the position space, single particle momentum distribution broaden. The lowering of the peak of the momentum distribution with increasing

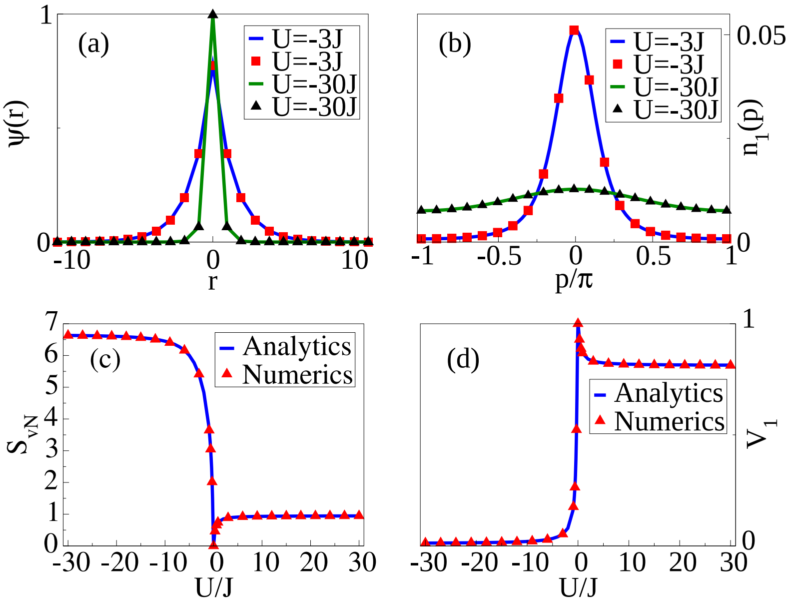

Figure 7.1: Ground state for two bosons (similar but distinguishable) on an 1D lattice which is a 101 site chain with periodic boundary conditions. (a) The relative wavefunction $\psi(r)$ for attractive interaction where r is the inter-particle separation. Here we plot the two cases where the interaction $U = -3J$ and $U = -30J$. The solid lines show the analytical results based on Eq. (7.5) and the red squares and black triangles show the calculations using exact diagonalisation. (b) The momentum distributions for $U = -3J$ and $U = -30J$, based on Eq. (7.8). Here again the solid lines show the analytical results and the red squares and black triangles show the calculations using exact diagonalisation. (c) The single particle von Neumann entropy S_{vN}, which is a measure of entanglement as a function of interaction. (d) The single particle visibility V_1, which is the height of the momentum distribution peak, as a function of interaction. For (c) and (d) the blue lines show the analytical results and the red triangles show the exact diagonalisation results.

interaction strength is the signature of the effect of the entanglement between the two particles and it is for this reason we are going to use the height of the momentum peak as a indicator or *visibility* of the effect of interaction in many body versions of this problem that we deal with in the proceeding sections. To have a direct look at the entanglement we calculate the single particle von Neumann entropy $S_{\text{vN}} = -\text{Tr}(\rho_1 \log_2 \rho_1)$ where ρ_1 is the single particle reduced density matrix. Fig. 7.1(c) shows the entanglement as a function of the interaction strength. On the attractive side ($U < 0$) the entanglement grows very sharply as a consequence of the direct pairing of the particles in position space that creates the bound state and reaches the saturation value shortly (which is $\log_2(M)$ as M is the size of the single particle Hilbert space). The entanglement in position space enforced by the repulsion between the particles although does not increase indefinitely with the interaction strength. This happens because the constraint in the position space created by the repulsive interaction is not as definitive as in the previous case. The interaction being an on-site phenomenon does not have greater effect with increasing strength as long as the particles stay away from each other by a certain number of sites. Therefore, the entanglement slowly increases and goes towards a steady asymptotic value as the repulsion is increased. The same behaviour can be seen in Fig. 7.1(d), where the single particle visibility V_1 is plotted as a function of interaction. Here we also see that the visibility falls very sharply on the attractive side as the particles become highly entangled in position space as a result of which the single particle momentum distribution becomes very flat quite fast. On the repulsive side also the slight drop of the visibility profile followed by a steady value reflects the partial entanglement of the particles in the position space caused by repulsion and the fact that increasing interaction strength cannot do much to increase the entanglement due to its on-site nature.

7.3 Many atoms on a lattice

In the next step we look at the ground state of an assembly of two different species of bosons, denoted by 1 and 2, in an optical lattice setup and study the properties in parameter regimes that are well within the reach of ongoing experiments. The nearest-neighbour tunnelling rates are J_1 and J_2 respectively. The intra-species onsite interaction strengths for species 1 and 2 are U_1 and U_2 respectively along with the presence of an inter-species interaction energy (onsite) U_{12}. Concentrating on the lowest Bloch band in the optical lattice potential we write down the two-species Bose-Hubbard Hamiltonian,

$$H_{BH} = \sum_{\sigma=1,2} \Bigg(- \sum_{<i,j>} J_\sigma b^\dagger_{\sigma,i} b_{\sigma,j} + \sum_i \frac{U_\sigma}{2} n_{\sigma,i}(n_{\sigma,i}-1) \Bigg) + \sum_i U_{12} n_{1,i} n_{2,i} \,, \quad (7.9)$$

where $b^\dagger_{\sigma,i}$ ($b_{\sigma,i}$) and $n_{\sigma,i}$ are the creation(annihilation) operator and number operator for species σ ($\sigma = 1, 2$) on the i-th site of a chain of total M sites. For our treatment of such a system we look at a number imbalanced situation where species 1 is at unity filling i.e. number of species 1 bosons, $N_1 = M$ and the species 2 is at quarter filling (unless otherwise stated) i.e. number of species 2 bosons, $N_2 = M/4$ so that it can be a representative of the minority *impurity* species whereas the species 2 particles stand for the majority reservoir species. The impurities are taken to be heavier by choosing $J_1 = J = 10J_2$ and all the other energy scales are measured in units of J. Now the ground state of such a system can be found using exact diagonalisation but only for a very small size (upto $M \approx 6$). For larger systems we use the well established numerical technique of density matrix renormalisation group (DMRG) method [70, 96, 97, 99, 100]. Before giving an account of that we take a look at a mean-field treatment using the Gutzwiller ansatz [178].

7.3.1 Mean-field treatment

Using Gutzwiller ansatz we approximate the ground state of the two species Bose-Hubbard Hamiltonian in (7.9) on a M-site chain as,

$$|\psi\rangle = \prod_{i=1}^{M} |\phi_i\rangle \, , \tag{7.10}$$

where $|\phi_i\rangle$, localised at i-th site, takes the form of a superposition of number states:

$$|\phi_i\rangle = \sum_{n_1=0\ldots N_1, n_2=0\ldots N_2} f^{(i)}_{n_1,n_2} |n_1, n_2\rangle \, . \tag{7.11}$$

Here $f^{(i)}_{n_1,n_2}$ is the amplitude associated with the i-th site having n_1 and n_2 number of species 1 and 2 bosons respectively. Imposing a normalisation condition on each $|\phi_i\rangle$ we can write $\sum_{n_1,n_2} |f^{(i)}_{n_1,n_2}|^2 = 1$. Further, H in (7.9) is replaced by a mean-field Hamiltonian H_{MF} which is just a sum of local operators:

$$H_{MF} = \sum_i \Bigg(\sum_{\sigma=1,2} \Bigg(- J_\sigma \left(b^\dagger_{\sigma,i} \Psi_{\sigma,i} + \Psi^*_{\sigma,i} b_{\sigma,i} \right) + \frac{U_\sigma}{2} n_{\sigma,i}(n_{\sigma,i} - 1) - \mu_\sigma n_{\sigma,i} \Bigg) + U_{12} n_{1,i} n_{2,i} \Bigg) , \tag{7.12}$$

where the order parameter

$$\Psi_{\sigma,i} = \sum_{j|i} \langle \phi_j | b_{\sigma,j} | \phi_j \rangle = \sum_{j|i} \sum_{n_\sigma, n_{\sigma'}} \sqrt{n_{\sigma,j}} f^{(j)*}_{(n_\sigma, n_{\sigma'})} f^{(j)}_{(n_\sigma+1, n_{\sigma'})} \tag{7.13}$$

serves as the variational parameter. Here $j|i$ denotes that the sum is over j which is a neighbouring site to i and $\sigma \neq \sigma'$. The fixed numbers of bosons of two different species are taken into account by computing the correct chemical potential values (μ_σ) for each. Thereafter the ground state is determined through a self-consistent loop initialized by the order parameters. The results of this mean-field treatment are reported along with the DMRG results in the proceeding sub-section.

7.3.2 Numerical simulation

The ground states of Eq. (7.9) computed using DMRG (except for the 6-site results which have been computed with exact diagonalisation) are compared in this sub-section with those obtained using mean-field methods earlier based on Eq. (7.12). Fig. 7.2, 7.3 and 7.4 show these comparisons. As discussed before, we use the height of the peak of the quasi-momentum distribution per particle, denoted by V_σ, for the species σ, for visibility. Similarly the von Neumann entropy S_{vN} shows the effect of entanglement between the two species. For the ED calculations (with periodic boundary condition) the lattice consists of 6 sites (M), and for the mean-field and DMRG calculations we used $M = 32$ and $M = 16$ respectively with bond dimension $D = 128$ in the later case. In all cases the number-dominant reservoir species is at unit filling ($N_1 = M$) and the impurity species is at quarter filling ($N_2 = M/4$), except for $M = 6$ where we have taken $N_2 = M/3$. In the following, for each figure showing the numerical results, we present a short discussion of the main features arising in this many-body system, followed by detailed descriptions of the plots.

In Fig. 7.2 we show the entanglement of the species 1 in terms of the von Neumann entropy S_{vN} as a function of inter-species interaction for the ED results in (a), the visibility profiles from the DMRG calculations in (b) and mean-field calculations in (d). We notice increase in entanglement and equivalently decrease in visibility as the inter-species interaction U_{12} is changed from zero to non-zero values, as was seen in the previous section for the system of two bosons on an optical lattice. A change in U_2 does not have significant effect on the general entanglement or the visibility profiles, so we fix the value to be $U_2 = 32J$. We also report the visibility V_2 of the species 2 in (c) for identical parameters, computed with DMRG calculations. The main characteristic feature that comes out of this figure is the equivalence of the messages conveyed by the entanglement plots and the visibility plots, as was seen in the two-particle case. Similar to the two-particle case, the entanglement rises as the inter-species coupling increases and correspondingly the visibility of the species 1 particles decreases. The interesting many-body effect takes over when the species 1 particles are strongly repulsive and go into a Mott insulator state. The visibility as well as entanglement stays low until the inter-species coupling is strong enough for the species 2 particles to disturb this localised state and then the particles from both species are entangled at a particular site. This causes increase in entanglement but due to the delocalisation possible for the species 1 particles, their visibility goes up as well, creating a contrast to the general trend of entanglement and visibility correspondance. In the following we discuss these behaviours in detail.

When the species 1 particles are not interacting among themselves ($U_1 = 0$) they are in an ideal superfluid state at $U_{12} = 0$ and we see a high visibility in this non entangled state in Fig. 7.2(b) (blue line). When U_{12} is turned on the visibility starts to decrease as entanglement grows between the two species. For negative U_{12} this happens due to localising effect imposed by species 2. For positive U_{12} the repulsion between the two species causes restriction in the complete delocalisation of the superfluid state and entanglement goes up but at a slower rate than that on the attractive U_{12} side. However the effect of this imposed restriction does

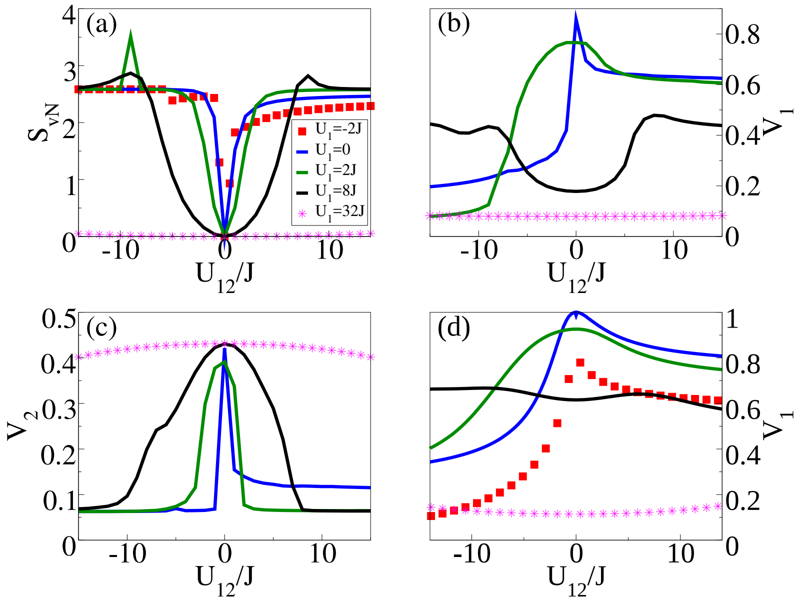

Figure 7.2: The von Neumann entropy between the two species, S_{vN} is shown in (a) extracted from ED calculations (with periodic boundary condition) for $M = 6, N_1 = M, N_2 = M/3$ and $U_2 = 32J$. The visibility V_1 of the species 1 as a function of inter-species interaction U_{12} for a lattice chain length $M = 16$ and $M = 32$ is shown in (b) and (d) respectively where $N_1 = M, N_2 = M/4$ and $U_2 = 32J$. (b) shows the results of DMRG calculations with bond dimension $D = 128$ for a range of U_1 values depicted in the legend. In (d) we also show the results carried out using mean-field calculations in a homogeneous lattice with Gutzwiller ansatz for the same values of U_1. We report the visibility V_2 of the species 2 in (c) for identical parameters as in (b), computed with DMRG calculations.

not increase arbitrarily and we expect the visibility reaching an asymptotic finite value for very large values of U_{12}.

On the repulsive side we first look at $U_1 = 2J$ in Fig. 7.2(b) (green line) where the particles of species 1 are still largely delocalised at $U_{12} = 0$ as they still are in the superfluid regime. The finite U_1 value however results in slight decrease of the visibility as it creates some constraints on the complete delocalisation that is possible at $U_1 = 0$ (blue line). As U_{12} is turned on we see similar behaviour for both the visibility and von Neumann entropy as was seen in the $U_1 = 0$ case, but now a repulsive U_{12} induces further constraints on the delocalisation resulting in further decrease of visibility. An attractive U_{12} however competes this delocalisation process due to the presence of the second species and the decrease in visibility is less than the $U_1 = 0$ case.

The interplay between the different interaction parameters give rise to a noticeable increase in the value of von Neumann entropy which happens at around the value $U_{12} = -9J$, as can be seen in Fig. 7.2(a) (green line). This happens due to drastic changes in the nature of the ground states. Around $U_{12} = -10J$ it is energetically favourable to have all the species 1 and species 2 particles at one single site. In Fig. 7.2(a), this can happen in 6 possible ways as we look at a 6 site system with periodic boundary condition. On the other side of the peak-like structure, around $U_{12} = -8J$, it is energetically favourable to have the 2 of the species 2 particles on adjacent sites, and this configuration can also achieved in 6 different ways. The von Neumann entropy is therefore indeed $\log_2 6$ on both sides of the peak. Now around the peak, which is near $U_{12} = -9J$ all the 12 configurations become important and the von Neumann entropy becomes $\log_2 12$. Carrying out Schmidt decomposition reveals that the ground state is very close to a maximally entangled states with 6 almost equal singular values for $U_{12} = -10J$ and $U_{12} = -8J$, and 12 almost equal singular values for $U_{12} = -9J$. The other singular values are suppressed by at least three orders of magnitude. Looking at the energy levels of the composite system we can also see that the lowest six levels are very close to each other at $U_{12} = -10J$ and $U_{12} = -8J$ whereas there is an avoided crossing with second lowest six levels at around $U_{12} = -9J$.

Another very interesting feature can be observed in the contrasting nature of the visibility profiles as we keep increasing U_1 from $2J$ and go to, for example, $U_1 = 8J$ in Fig. 7.2(b) where we see the visibility going through a minimum at zero inter-species interaction. As species 1 is at unit filling and goes into a deep Mott insulator regime when U_1 value is changed from $2J$ to $8J$, the physical intuition is that the particles become localised at the lattice sites. This results in a broadening of their momentum distribution that causes the dip in the height of the momentum peak. For low inter-species interaction the particles from the species 2 do not have sufficiently strong effect on them to change their position in space which can be seen in the entanglement picture also as the rise of von Neumann entropy is much slower here than the $U_1 = 2J$ case (Fig. 7.2(a)). Note that the

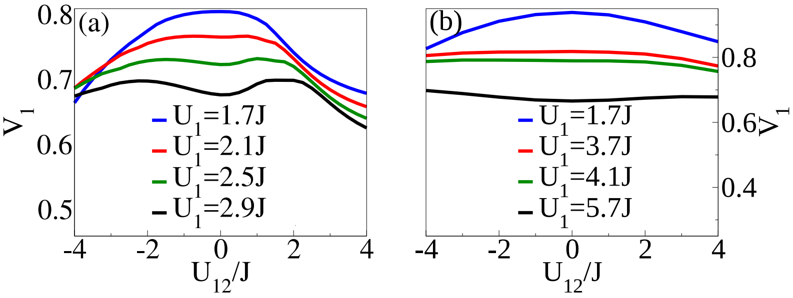

FIGURE 7.3: The visibility V_1 of the species 1 as a function of inter-species interaction U_{12} for a lattice chain length M where $N_1 = M, N_2 = M/4$ and $U_2 = 32J$. (a) shows the results of DMRG calculations with $M = 16$ and bond dimension $D = 128$. We fix U_2 and look at different U_1 values depicted in the legend which are close to a critical value where one can see a change in the behaviour of the visibility profile which changes from going through a maximum for zero inter-species interaction to a minimum. In (b) we also show the results in the same interaction parameter regimes carried out with mean-field calculations in a homogeneous lattice with $M = 32$ using Gutzwiller ansatz where the U_1 values shown in the figure which shows a different value of U_1 where the characteristic behaviour change occurs for systems with open boundary conditions used with DMRG computations.

critical value for a crossover for species 1 from superfluid regime to Mott insulator regime in 1D occurs at $U_1 = 3.37J$ which falls in between the U_1 values we are looking at here. We therefore study this region around $U_{12} = 0$ for suitable U_1 values in greater detail in the next paragraph. In mean-field treatment the phase transition occurs at $U_1 = 11.6J$ in 1D for unit filling but our argument should still hold as $U_1 = 8J$ would still favour a state with unity as site occupation number. If we look at the $U_1 = 8J$ line in Fig. 7.2(b) the subsequent local maximums on the both sides of the minimum occurring at $U_{12} = 0$ happen due the increase in U_{12} where the effect of the presence of a second species becomes stronger. As U_{12} becomes comparable to U_1, the energy input due to the presence of a species 2 particle disrupts the localised phase as the energy penalty for having a double occupation of species 1 is comparable to the energy required to put two particles from the different species on a single site. Thus the species 1 particles begin to delocalise and the visibility starts to go up. However the increasing U_{12} imposes a restriction on this delocalisation process which causes a drop in the visibility again.

For $U_1 = 32J$ the particles in species 1 are in the deep Mott insulator regime and in the range of U_{12} that we are looking at here the energy input in the system by the presence of the particles of species 2 cannot affect the Mott insulator as U_{12} is always much smaller than U_1 . Since varying the interaction strength does not entangle species 1 with the other the von Neumann entropy stays at zero. The visibility of these highly site-localised species 1 particles also stays constant at a very low value which is smaller for the mean-field treatment as we can see in Fig. 7.2(c). This is because in mean-field treatment the off-site spatial correlations in a Mott insulator are exactly zero and in a numerically exact treatment they fall exponentially with the spatial distance. Therefore when we take a Fourier transform of the spatial correlations to get to the momentum distribution, in the mean-field treatment we should get zero and slightly larger values for the DMRG results which we see in terms of the visibilities in Fig. 7.2(b).

In Fig. 7.3 we take a closer look at the transition-like feature, namely the behaviour of the visibility profile which changes from going through a maximum at zero inter-species interaction (for example, the $U_1 = 1.7J$ line in Fig. 7.3(a)) to a minimum (for example, the $U_1 = 2.9J$ line in Fig. 7.3(a)) for a certain critical U_1 value. Here we notice the transition like feature which is the characteristic of a superfluid to Mott insulator phase transition in 1D occurring at around $U_1 = 2J$ when computed using DMRG. However the same transition like behaviour occurs at double of the previous value i.e. around $U_1 = 4J$ in Fig. 7.3(b) which is a homogeneous mean-field calculation that imposes a periodic boundary conditions on a 32 site system.

Now we move on to Fig. 7.4 where we mainly look at the particles of the second species. The properties of these impurity particles should depend strongly on the many-body state of the species 1 particles and therefore should be affected by the choice of U_1 values. The visibility of species 2 as a function of U_{12} in general has a peak around $U_{12} = 0$ that dies down on both sides. This peak-like structure starts broadening as we keep increasing U_1 starting from zero. The visibility profiles are quite similar to that seen in the previous section for the system of two bosons on an optical lattice in terms of the mechanisms that create a maximum at $U_{12} = 0$ and a slower decrease for repulsive U_{12}. The value of the maximum visibility also follows similar trend as a function of U_2 and falls sharply for attractive U_2 whereas falls much slowly on the repulsive side. This particular behaviour is reported in Fig. 7.2(c). For very large and positive U_1 values however we notice some interesting features emerging that are reported in the following paragraphs and Fig. 7.4(a), (b) and (d). In Fig. 7.4(c) we report the visibility V_1 of the species 1 for identical parameters, computed with DMRG calculations. In this case as we look at the strongly interacting regime for the species 1 particles, they are deeply in a localised state and therefore show low entanglement and visibility. The species 2 particles show high visibility as their motion is not affected by the species 1 particles until the inter-species coupling is strong enough to disturb the localised state and force the particles from both species to be highly correlated in position space that results in sharp increase of entanglement and visibility of the species 1 particles due to delocalisation, accompanied by sharp decrease in visibility of the species 2 particles. Details of this mechanism is described in the following paragraphs.

As U_1 is increased to $32J$ species 1 particles are in the deep Mott insulator regime as they also have unit filling. Now for $U_2 = 0$ the impurity particles cannot sense the presence of each other and the presence of the Mott insulator for small U_{12} effectively only can create a small change in the optical lattice potential uniformly at each site. Therefore we basically expect the impurities to behave like free particles on a modified lattice and see them almost not entangled at all to species 1, causing a strong visibility that sustains on both sides of $U_{12} = 0$ as shown in Fig. 7.4(b). As U_{12} becomes large enough on the positive side after a particular point it becomes energetically favourable for the impurity particles to stay together at one single lattice site and push out the species 1 particle to the neighbouring site, thereby creating a *hole* in the Mott insulator. The impurity particles get localised in position space by the species 1 particles through this process and therefore we see a sharp rise in entanglement that results in a sudden fall in the visibility of species 2. The value of U_{12} at which this fall starts to happen depends on the number of impurity particles and expectedly we notice this value to be U_1/N_2 in Fig. 7.4. Now on the attractive side of U_{12} around the same magnitude (U_1/N_2) it also becomes energetically favourable to create a *hole*

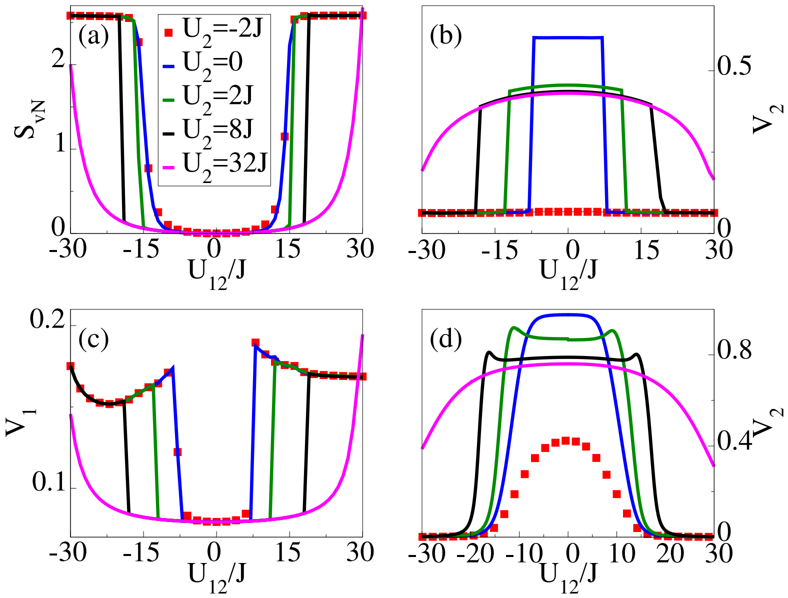

FIGURE 7.4: The von Neumann entropy between the two species, S_{vN} is shown in (a) extracted from ED calculations (with periodic boundary condition) for $M = 6, N_1 = M, N_2 = M/3$ and $U_1 = 32J$. The visibility V_2 of the species 2 as a function of inter-species interaction U_{12} for a lattice chain length $M = 16$ and $M = 32$ is shown in (b) and (d) respectively where $N_1 = M, N_2 = M/4$ and $U_1 = 32J$. (b) shows the results of DMRG calculations with bond dimension $D = 128$ for a range of U_2 values depicted in the legend. In (d) we also show the results carried out using mean-field calculations in a homogeneous lattice with Gutzwiller ansatz for the same values of U_2. We report the visibility V_1 of the species 1 in (c) for identical parameters as in (b), computed with DMRG calculations.

in the Mott insulator and to have all the impurity particles on that neighbouring site of the hole where the species 1 particle has tunnelled to. Due to this similar localisation the two species become highly entangled and the visibility V_2 again fall drastically. For an infinite lattice system (which is the case when one treats the problem in mean-field theory) this localisation process causes the visibility to completely vanish, as shown in Fig. 7.4(d). For a finite system (Fig. 7.4(b)) the visibility falls down and takes a constant value and that value decrease as we increase the system size.

Now for $U_2 = 2J$ the visibility at $U_{12} = 0$ will be smaller than the previous case as the impurity particles repulsively interact among themselves. This decrease in height of the visibility persists as we increase U_2 value but not arbitrarily as we have discussed before. For small values of U_{12} the visibility again stay unchanged and we also see the same localisation effect causing a drop in visibility at sufficiently high U_{12} as before. The magnitude of U_{12} at which the drop happens increases with increase in U_2 as the repulsion between the impurity particles also need to be overcome. We see this for $U_2 = 2J, 8J$ and $32J$ in Fig. 7.4(b).

For attractive U_2 we expect the similar plateau-like visibility profile but with much smaller value to start with (at and around $U_{12} = 0$) and we see that in Fig. 7.4(b) for $U_2 = -2J$ although the plateau-like structure is hardly visible due to such small value of the peak. The value of visibility (for all the profiles) after the drop tends to go to $1/M$ which is lower limit for the peak of a single particle momentum distribution on a lattice with M sites (one can think about two particles on a lattice with infinitely strong inter-particle potential where the single particle momentum distribution is completely flat in the ground state).

7.4 Effect of the size of the reservoir

So far we have looked at setups where the impurity particles and reservoir particles are on the same optical lattice. Now for the next step we consider the experimental situation that was the motivation for this study. We look at a single bosonic impurity atom which is confined in an one-dimensional optical lattice where it is allowed to tunnel to the neighbouring lattice site. The optical lattice setup is immersed in a much larger one-dimensional BEC. We can consider a single bosonic impurity atom with mass m_B which is confined in an one-dimensional optical lattice with M sites where it is allowed to tunnel to the neighbouring lattice site with a rate J_B. The optical lattice setup is immersed in a much larger BEC which is also restricted to one spatial dimension. The BEC without the coupling to the impurity atom can be described by the mean-field macroscopic condensate wave function $\psi(x,t)$ which obeys the Gross-Pitaevskii equation (GPE):

$$i\hbar\frac{\partial\psi}{\partial t} = \left(-\frac{\hbar^2}{2m_A}\frac{\partial^2}{\partial x^2} + g_A|\psi(x,t)|^2\right)\psi(x,t)\,, \tag{7.14}$$

where m_A is mass of an condensate atom, g_A is a positive condensate coupling constant and total number of condensate atoms $N_A = \int dx|\psi|^2$. The time independent form of the equation (7.14) enables us to compute the ground state numerically. Now if the total length of the optical lattice is negligible compared to that the BEC and the ratio of impurity-BEC coupling g_{AB} (which is also positive) and coupling within the BEC g_A is small enough we can still describe the BEC by a mean-field condensate wave function. This is also the desired description of the BEC as we would like to work in the context of non-destructive probing by the impurity system. Therefore we find the ground state solution $\phi_i(x)$ corresponding to the presence of an impurity boson located at the i-th site by numerically performing an imaginary time evolution of the GPE similar to equation (7.14) but taking into account the presence of the impurity using split-step Crank-Nicolson scheme [179]. Now we can write down the ground state as $|\psi_{GS}\rangle = \sum_{i=1}^{M} c_i|i\rangle_B|\phi_i\rangle_A$. The coefficients c_i-s can be found by using the norm preservation and minimisation of the total energy which consists of three parts, namely, the condensate energy,

$$E_A = \sum_{i=1}^{M}|c_i|^2\int dx\phi_i^*(x)\left(-\frac{\hbar^2}{2m_A}\frac{\partial^2}{\partial x^2} + g_A|\phi_i(x)|^2\right)\phi_i(x)\,, \tag{7.15}$$

energy of the impurity atom

$$E_B = -J_B\sum_{i=1}^{M}c_i^*c_j\int dx\phi_i^*(x)\phi_j(x)\,, \tag{7.16}$$

and the interaction energy

$$E_{AB} = g_{AB}\sum_{i=1}^{M}\int dx|\phi_i(x)|^2\omega_i^2(x)\,, \tag{7.17}$$

where we have used a harmonic oscillator approximation for the impurity wave function localised on the ith site at the position x_i, $\omega_i(x) = e^{-(x-x_i)^2/2a_0^2}/\pi^{1/4}\sqrt{a_0}$

with oscillator length $a_0 = (m_B\hbar^2/2V_L k_L^2)^{1/4}$. Here V_L is the lattice depth and k_L is the laser wave-number that generates the lattice. This approximation is valid for lattices deep enough so that the Lamb-Dicke parameter $k_L a_0 \ll 1$. After finding the ground state we look for the effect of changing the interaction strength g_{AB} on the visibility of the momentum distribution of the impurity atom. As the BEC is much larger than the optical lattice, for repulsive interaction the small changes in the strength does not change ground state appreciably and we do not observe the visibility to be affected. In other words the visibility of the impurity species hardly changes when we turn on the inter-species interaction from zero to a small finite value.

To estimate the effect the largeness of the BEC compared to the lattice we first look at a simplified and discrete version of this problem. We look at a system where N_A non-interacting particles can move in an optical lattice with M_A sites and only next neighbour tunnelling is allowed with a rate J_A. We also include an impurity atom that is only allowed to move in the central M_B number of sites (out of M_A). The onsite interaction energy between the two species is U_{AB}. We look for the effect of the ratio M_B/M_A on the visibility associated with the impurity for different values of U_{AB}. We first solve the case where we only have two particles moving on this lattice system, i.e. $N_A = 1$. They are also taken to be of same mass (we later discuss the effect of having heavier impurities) inducing same tunnelling rate J for both particles. We can numerically diagonalise the two-particle Hamiltonian,

$$H = -J \sum_{\sigma=A,B;<i,j>} b^\dagger_{\sigma,i} b_{\sigma,j} + \sum_i U_{AB} n_{A,i} n_{B,i} \, . \tag{7.18}$$

to find the normalised lowest energy state $|\psi\rangle = \sum_{i=1,\ldots,M_A;j=1,\ldots,M_B} c_{i,j} |i\rangle_A |j\rangle_B$. We use periodic boundary conditions on both lattice systems. The single particle density matrix for the impurity species B is

$$\langle b^\dagger_i b_j \rangle_B = \sum_{k=1,\ldots,M_A} c^*_{k,i} c_{k,j} \, , \tag{7.19}$$

from which we can build up the momentum distribution

$$n_B(q) = \frac{1}{M_B} \sum_{i,j=1,\ldots,M_B} e^{iq(i-j)} \langle b_i^\dagger b_j \rangle_B \,. \tag{7.20}$$

We look at the maximum of the momentum distribution as the visibility of the impurity species as before. As we like to infer the effect of the size differences in M_A and M_B and in particular to figure out the existence of a possible scaling factor after which the growth of M_A cease to have an impact on the visibility for different interaction, we look at the characteristic differences in visibilities V_B (for species B) for $U_{AB} = 0$ and $U_{AB} = 8J$ for increasing M_A and for different M_B values. As seen in Fig. 7.5(a), V_B increases steadily for smaller values of M_A for a given M_B and following what looks like a quite universal scaling factor $M_A/M_B = 3$ (red line in Fig. 7.5(b)) stops increasing any more and becomes same as what the visibility would be in the absence of any interaction i.e. unity. This gives us an idea that if size of the bigger lattice is at least three times the size of the impurity lattice system the effect of repulsive interaction on its visibility becomes quite negligible.

Now we explore the effect of having a heavier impurity particle in the lattice system so that its tunnelling rate J_B is smaller than J_A. In particular we would like to find out how small J_B should be compared to J_A so that we can treat the tunnelling term for the impurity particles in perturbation theory. In Fig. 7.5(b) we report the exact diagonalisation results where we plot the visibilities for the value $U_{AB} = 8J_A$, denoted by V_B, against M_A/M_B for descending values of J_B/J_A. As we can see $J_B/J_A = 10^{-3}$ is where the result matches with the perturbation theory results which are shown by black circles.

7.5 Summary

In this work, which is motivated by the discrepancy found in a recent experiment on a system of coupled bosonic impurities immersed in a BEC, we have proposed a possible reasoning behind the enhancement beyond the expected drop in observed

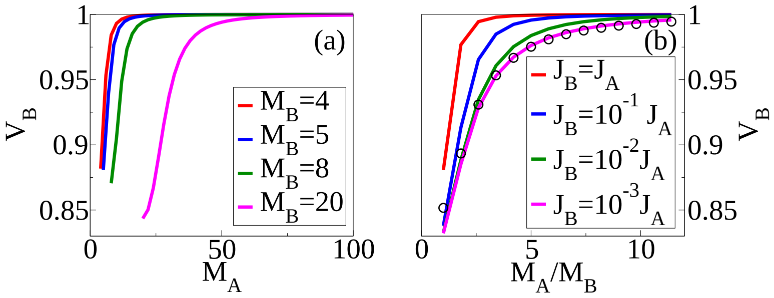

FIGURE 7.5: (a) Visibility of the impurity particle V_B for $U_{AB} = 0$ and $U_{AB} = 8J$ is shown here for different M_B values while increasing M_A. We see for $U_{AB} = 8J$, V_B increases up to a certain value of M_A/M_B following which it seems to stay unchanged and close to 1 which is its value for $U_{AB} = 0$. This scaling factor M_A/M_B is found be around 3 as shown by the red line in the right half of the figure. (b) The visibility of the impurity particle V_B for $U_{AB} = 8J_A$ is shown here for different M_A/M_B values while decreasing J_B/J_A. We see $J_B/J_A = 10^{-3}$ is where the result matches with the result obtained from calculations using the tunnelling term for the impurity particle as a perturbation, shown by the black circles.. We have taken $M_B = 5$ for this calculation. In both (a) and (b) we have used periodic boundary conditions on both lattice systems for exact diagonalisation.

visibility to be arising from the entanglement between the two systems. We have seen that indeed the visibility profiles for a two-species bosonic system show qualitatively the similar features as the inter-species entanglement profiles do as a function of the coupling strength. Looking at a simple system of just two bosons on a lattice gives us a nice analytical and exact-numerical insight for the decrease of visibility due to increase in entanglement. This feature in general is observed for a wide range of parameters when we move to a many-boson system on an optical lattice, treating the bosonic species minority in number as the impurities acted upon by the reservoir of the majority species. This is a nice result that matches our expectations.

In certain strong interaction regimes, many-body effects produce some very interesting features that can be realistically investigated in experiments. When the impurity bosons are in the strongly repulsive regime they are capable of disrupting the Mott insulator state formed by the reservoir bosons at certain coupling strength set by the relative interaction strengths. Therefore the visibility of the reservoir bosons show sudden increase for particular coupling values although the entanglement characteristically increases. Similarly when the intra-species interaction strength in the reservoir bosons is very high and a Mott insulator is formed, the impurity bosons can only affect this state for strong enough coupling values where we see sudden drop in impurity visibilities accompanied by sudden rise of entanglement correspondingly.

In the context of non-destructive probing experiments, we have also found that an impurity boson cannot alter the wavefunction of a large BEC for small coupling and hence there is no change in visibility of the impurity solely due to coupling. A numerical estimation, carried out on an optical lattice setup with two species bosons as before, of the largeness of the bath system to produce this null result gives a factor of around 3 for the relative size.

Chapter 8

Conclusion

Our main objective in this thesis was to study the dynamics of open quantum systems in the presence of sources of quantum decoherence that are highly relevant in the context of present day experiments with ultracold atoms in optical lattices. Understanding the dissipative dynamics is absolutely necessary in order to be able to control heating and to find new ways to reach lower temperatures as well as use controlled dissipation to drive the system in the desired many-body state. In Chapter 5 we have considered the experimentally relevant atomic species and developed, based on our microscopic understanding of the atoms in the optical lattice setup, a master equation for two-species fermions to model the dynamics under the dissipative effects caused by the incoherent scattering of the photons from a far-detuned laser. The findings of this work can be used to characterise heating in ongoing experiments which is extremely important for the realisation of magnetic order. In this context the suppression of spin order is indeed an encouraging factor. From the theoretical point of view this work can be extended, using our microscopic understanding of the underlying physics, to study the thermalisation while taking transfer to higher bands due to spontaneous emissions into account as this will further enrich our understanding of heating mechanisms in these experiments.

The master equation derived for the two-species fermions is then applied, in Chapter 6, to a recent experiment that looks at the stability of already established many-body localisation (MBL) with ultracold fermions in optical lattices, but with controlled dissipation due to a detuned laser dedicated to induce a higher scattering rate. Looking at the experimental atomic species we determined the relative decay rates of the two possible decohering mechanisms, namely, dephasing due to localisation and atom loss due to excitation to higher bands. The resulting dynamics in terms of quantities relevant to MBL are found to be in agreement with the theoretical predictions. The susceptibility to the scattering incidents is not appreciably affected by the interaction strength in deeply localised phase but close to the MBL transition, increasing inter-particle interactions results in a dramatic rise in susceptibility to decoherence. This work, on the theoretical side, has potential expansion direction towards an analytical design of a model to see the behaviour of the susceptibility qualitatively with both the dissipative channels as well as numerical optimisation to take into account the atom loss mechanism. Another possible direction to explore is the delocalised side of the MBL transition and to study the effect of spontaneous emission events on the imbalance decay.

In Chapter 7 we proposed an explanation for a recent experimental finding on a system of coupled bosonic impurities immersed in a BEC, in terms of a drop in observed visibility beyond the expected value. We link this enhancement to the entanglement between the two species in this coupled system which can be thought of comprising of an open system of minority species acted on by a reservoir of the majority species. Our numerical findings support this proposal by revealing similar qualitative behaviour of the entanglement and the visibility profiles. Along with these results we observe some very interesting many-body features in strongly interacting regimes that relate directly to entanglement between the two species, and would be observable in experiments. A future direction to work on would be to have better analytical support for these numerical findings, qualitatively. We also present a numerical study of these two-species systems to estimate the relative size of the reservoir that would be a minimal requirement to be unaffected by small couplings to the impurity system. This forms a basis for establishing better analytical insight of the impurity-BEC system in order to help design non-destructive probing experiments.

Bibliography

[1] J. Hubbard. Electron correlations in narrow energy bands. *Proceedings of the Royal Society of London. Series A, Mathematical and Physical Sciences*, 276(1365):238–257, 1963.

[2] D. J. Scalapino. The case for dx^2 - y^2 pairing in the cuprate superconductors. *Physics Reports*, 250(6):329 – 365, 1995.

[3] W. Hofstetter, J. I. Cirac, P. Zoller, E. Demler, and M. D. Lukin. High-temperature superfluidity of fermionic atoms in optical lattices. *Phys. Rev. Lett.*, 89:220407, 2002.

[4] J. Quintanilla and C. Hooley. The strong-correlations puzzle. *Physics World*, 22(06):32, 2009.

[5] R. P. Feynman. Simulating physics with computers. *International Journal of Theoretical Physics*, 21:467–488, 1982.

[6] I. Buluta and F. Nori. Quantum simulators. *Science*, 326(5949):108–111, 2009.

[7] J. I. Cirac and P. Zoller. Goals and opportunities in quantum simulation. *Nat. Phys.*, 8(4):264–266, 2012.

[8] I. Bloch, J. Dalibard, and S. Nascimbène. Quantum simulations with ultracold quantum gases. *Nat. Phys.*, 8(4):267–276, 2012.

[9] R. Blatt and C. F. Roos. Quantum simulations with trapped ions. *Nat. Phys.*, 8(4):277–284, 2012.

[10] A. Aspuru-Guzik and P. Walther. Photonic quantum simulators. *Nat. Phys.*, 8(4):285–291, 2012.

[11] C. J. Pethick and H. Smith. *Bose-Einstein Condensation in Dilute Gases.* Cambridge University Press, 2008.

[12] M. H. Anderson, J. R. Ensher, M. R. Matthews, C. E. Wieman, and E. A. Cornell. Observation of Bose-Einstein condensation in a dilute atomic vapor. *Science*, 269(5221):198–201, 1995.

[13] K. B. Davis, M. O. Mewes, M. R. Andrews, N. J. van Druten, D. S. Durfee, D. M. Kurn, and W. Ketterle. Bose-Einstein condensation in a gas of sodium atoms. *Phys. Rev. Lett.*, 75:3969–3973, 1995.

[14] C. C. Bradley, C. A. Sackett, J. J. Tollett, and R. G. Hulet. Evidence of Bose-Einstein condensation in an atomic gas with attractive interactions [Phys. Rev. Lett. 75, 1687 (1995)]. *Phys. Rev. Lett.*, 79:1170–1170, 1997.

[15] H. J. Metcalf and P. van der Straten. *Laser Cooling and Trapping.* Springer, 1999.

[16] W. Ketterle and N. J. van Druten. Evaporative cooling of trapped atoms. *Advances In Atomic, Molecular, and Optical Physics*, 37:181 – 236, 1996.

[17] I. Bloch and P. Zoller. Focus on cold atoms in optical lattices. *New Journal of Physics*, 8(8), 2006.

[18] I. Bloch. Quantum gases. *Science*, 319(5867):1202–1203, 2008.

[19] D. Jaksch, C. Bruder, J. I. Cirac, C. W. Gardiner, and P. Zoller. Cold bosonic atoms in optical lattices. *Phys. Rev. Lett.*, 81:3108–3111, 1998.

[20] C. Gerry and P. L. Knight. *Introductory Quantum Optics.* Cambridge University Press, 2005.

[21] R. Chin, C.and Grimm, P. Julienne, and E. Tiesinga. Feshbach resonances in ultracold gases. *Rev. Mod. Phys.*, 82:1225–1286, 2010.

[22] D. Jaksch and P. Zoller. The cold atom Hubbard toolbox. *Ann. Phys.*, 315 (1):52 – 79, 2005.

[23] M. Greiner, O. Mandel, T. Esslinger, T. W. Hansch, and I. Bloch. Quantum phase transition from a superfluid to a Mott insulator in a gas of ultracold atoms. *Nature*, 415:39–44, 2002.

[24] M. P. A. Fisher, P. B. Weichman, G. Grinstein, and D. S. Fisher. Boson localization and the superfluid-insulator transition. *Phys. Rev. B*, 40:546–570, 1989.

[25] R. Jördens, N. Strohmaier, K. Günter, H. Moritz, and T. Esslinger. A Mott insulator of fermionic atoms in an optical lattice. *Nature (London)*, 455(7210):204–207, 2008.

[26] U. Schneider, L. Hackermüller, J. P. Ronzheimer, S. Will, S. Braun, T. Best, I. Bloch, E. Demler, S. Mandt, D. Rasch, and A. Rosch. Fermionic transport and out-of-equilibrium dynamics in a homogeneous Hubbard model with ultracold atoms. *Nat. Phys.*, 8(3):213–218, 2012.

[27] K. Günter, T. Stöferle, H. Moritz, M. Köhl, and T. Esslinger. Bose-Fermi mixtures in a three-dimensional optical lattice. *Phys. Rev. Lett.*, 96:180402, 2006.

[28] M. Greiner, O. Mandel, T. W. Hansch, and I. Bloch. Collapse and revival of the matter wave field of a Bose-Einstein condensate. *Nature*, 419:51–54, 2002.

[29] S. Will, T. Best, U. Schneider, L. Hackermüller, D. Luhmann, and I. Bloch. Time-resolved observation of coherent multi-body interactions in quantum phase revivals. *Nature*, 465, 2010.

[30] K. Winkler, G. Thalhammer, F. Lang, R. Grimm, J. Hecker Denschlag, A. J. Daley, A. Kantian, H. P. Büchler, and P. Zoller. Repulsively bound atom pairs in an optical lattice. *Nature*, 441(7095):853–856, 2006.

[31] W. S. Bakr, J. I. Gillen, A. Peng, S. Folling, and M. Greiner. A quantum gas microscope for detecting single atoms in a Hubbard-regime optical lattice. *Nature*, 462:74–77, 2009.

[32] J. Simon, W. S. Bakr, R. Ma, M. E. Tai, P. M. Preiss, and M. Greiner. Quantum simulation of antiferromagnetic spin chains in an optical lattice. *Nature (London)*, 472(7343):307–312, 2011.

[33] E. Haller, J. Hudson, A. Kelly, D. A. Cotta, B. Peaudecerf, G. D. Bruce, and S. Kuhr. Single-atom imaging of fermions in a quantum-gas microscope. *Nat. Phys.*, 11:738–742, 2015.

[34] M. F. Parsons, A. Mazurenko, C. S. Chiu, G. Ji, D. Greif, and M. Greiner. Site-resolved measurement of the spin-correlation function in the Fermi-Hubbard model. *Science*, 353(6305):1253–1256, 2016.

[35] H. T. Ng and S. Bose. Single-atom-aided probe of the decoherence of a Bose-Einstein condensate. *Phys. Rev. A*, 78:023610, 2008.

[36] A. Griessner, A. J. Daley, S. R. Clark, D. Jaksch, and P. Zoller. Dark-state cooling of atoms by superfluid immersion. *Phys. Rev. Lett.*, 97:220403, 2006.

[37] A. Klein and M. Fleischhauer. Interaction of impurity atoms in Bose-Einstein condensates. *Phys. Rev. A*, 71:033605, 2005.

[38] F. Massel, A. Kantian, A. J. Daley, T. Giamarchi, and P. Trm. Dynamics of an impurity in a one-dimensional lattice. *New Journal of Physics*, 15(4): 045018, 2013.

[39] M. Bruderer, A. Klein, S. R. Clark, and D. Jaksch. Transport of strong-coupling polarons in optical lattices. *New Journal of Physics*, 10(3):033015, 2008.

[40] G. Lang and A. Firsov, Yu. Calculation of the activation probability for a jump of a small-radius polaron. *Soviet Physics JTEP*, 27(3):443, 1968.

[41] T. Fukuhara, P. Schausz, M. Endres, S. Hild, M. Cheneau, I. Bloch, and C. Gross. Microscopic observation of magnon bound states and their dynamics. *Nature (London)*, 502(7469):76–79, 2013.

[42] A. Bruderer, M.and Klein, S. R. Clark, and D. Jaksch. Polaron physics in optical lattices. *Phys. Rev. A*, 76:011605, 2007.

[43] W. Casteels, J. Tempere, and J. T. Devreese. Bipolarons and multipolarons consisting of impurity atoms in a Bose-Einstein condensate. *Phys. Rev. A*, 88:013613, 2013.

[44] A. A. Blinova, M. G. Boshier, and E. Timmermans. Two polaron flavors of the Bose-Einstein condensate impurity. *Phys. Rev. A*, 88:053610, 2013.

[45] Steffen P. Rath and R. Schmidt. Field-theoretical study of the Bose polaron. *Phys. Rev. A*, 88:053632, 2013.

[46] D. Benjamin and E. Demler. Variational polaron method for Bose-Bose mixtures. *Phys. Rev. A*, 89:033615, 2014.

[47] S. Smerat, U. Schollwöck, I. P. McCulloch, and H. Schoeller. Quasiparticles in the Kondo lattice model at partial fillings of the conduction band using the density matrix renormalization group. *Phys. Rev. B*, 79:235107, 2009.

[48] V. M. Stojanović, T. Shi, C. Bruder, and J. I. Cirac. Quantum simulation of small-polaron formation with trapped ions. *Phys. Rev. Lett.*, 109:250501, 2012.

[49] J. Bardeen, G. Baym, and D. Pines. Effective interaction of He^3 atoms in dilute solutions of He^3 in He^4 at low temperatures. *Phys. Rev.*, 156:207–221, 1967.

[50] M. J. Bijlsma, B. A. Heringa, and H. T. C. Stoof. Phonon exchange in dilute Fermi-Bose mixtures: Tailoring the Fermi-Fermi interaction. *Phys. Rev. A*, 61:053601, 2000.

[51] A. Recati, J. N. Fuchs, C. S. Peça, and W. Zwerger. Casimir forces between defects in one-dimensional quantum liquids. *Phys. Rev. A*, 72:023616, 2005.

[52] R. P. Feynman. Atomic theory of the two-fluid model of liquid Helium. *Phys. Rev.*, 94:262–277, 1954.

[53] A. Miller, D. Pines, and P. Nozières. Elementary excitations in liquid Helium. *Phys. Rev.*, 127:1452–1464, 1962.

[54] G. E. Astrakharchik and L. P. Pitaevskii. Motion of a heavy impurity through a Bose-Einstein condensate. *Phys. Rev. A*, 70:013608, 2004.

[55] T. Stöferle, H. Moritz, C. Schori, M. Köhl, and T. Esslinger. Transition from a strongly interacting 1D superfluid to a Mott insulator. *Phys. Rev. Lett.*, 92:130403, 2004.

[56] B. Paredes, A. Widera, V Murg, O. Mandel, S. Fölling, I. Cirac, G.V. Shlyapnikov, T.W. Hänsch, and I. Bloch. Tonks-Girardeau gas of ultracold atoms in an optical lattice. *Nature*, 429:277–281, 2004.

[57] M. Schreiber, S. S. Hodgman, P. Bordia, H. P. Lüschen, M. H. Fischer, R. Vosk, E. Altman, U. Schneider, and I. Bloch. Observation of many-body localization of interacting fermions in a quasirandom optical lattice. *Science*, 349(6250):842–845, 2015.

[58] S. Trotzky, P. Cheinet, S. Fölling, M. Feld, U. Schnorrberger, A. M. Rey, A. Polkovnikov, E. A. Demler, M. D. Lukin, and I. Bloch. Time-resolved observation and control of superexchange interactions with ultracold atoms in optical lattices. *Science*, 319(5861):295–299, 2008.

[59] Tilman E. Fermi-Hubbard physics with atoms in an optical lattice. *Annual Review of Condensed Matter Physics*, 1(1):129–152, 2010.

[60] Daniel Greif, Thomas Uehlinger, Gregor Jotzu, Leticia Tarruell, and Tilman Esslinger. Short-range quantum magnetism of ultracold fermions in an optical lattice. *Science*, 340(6138):1307–1310, 2013.

[61] R. A. Hart, P. M. Duarte, T. Yang, X. Liu, T. Paiva, E. Khatami, R. T. Scalettar, N. Trivedi, D. A. Huse, and R. G. Hulet. Observation of antiferromagnetic correlations in the Hubbard model with ultracold atoms. *Nature*, 519:211–214, 2015.

[62] H. Pichler, J. Schachenmayer, J. Simon, P. Zoller, and A. J. Daley. Noise- and disorder-resilient optical lattices. *Phys. Rev. A*, 86:051605, 2012.

[63] H. Pichler, J. Schachenmayer, A. J. Daley, and P. Zoller. Heating dynamics of bosonic atoms in a noisy optical lattice. *Phys. Rev. A*, 87:033606, 2013.

[64] F. Gerbier and Y. Castin. Heating rates for an atom in a far-detuned optical lattice. *Phys. Rev. A*, 82:013615, 2010.

[65] H. Pichler, A. J. Daley, and P. Zoller. Nonequilibrium dynamics of bosonic atoms in optical lattices: Decoherence of many-body states due to spontaneous emission. *Phys. Rev. A*, 82:063605, 2010.

[66] J. Schachenmayer, L. Pollet, M. Troyer, and A. J. Daley. Spontaneous emission and thermalization of cold bosons in optical lattices. *Phys. Rev. A*, 89:011601, 2014.

[67] S. R. White. Density matrix formulation for quantum renormalization groups. *Phys. Rev. Lett.*, 69:2863–2866, 1992.

[68] S. R. White. Density-matrix algorithms for quantum renormalization groups. *Phys. Rev. B*, 48:10345–10356, 1993.

[69] G. Vidal. Efficient classical simulation of slightly entangled quantum computations. *Phys. Rev. Lett.*, 91:147902, 2003.

[70] G. Vidal. Efficient simulation of one-dimensional quantum many-body systems. *Phys. Rev. Lett.*, 93:040502, 2004.

[71] H. Carmichael. *An Open Systems Approach to Quantum Optics.* Springer, Berlin, 1993.

[72] K. Mølmer, Y. Castin, and J. Dalibard. Monte Carlo wave-function method in quantum optics. *J. Opt. Soc. Am. B*, 10(3):524–538, 1993.

[73] A. J. Daley. Quantum trajectories and open many-body quantum systems. *Advances in Physics*, 63(2):77–149, 2014.

[74] C. Cohen-Tannoudji, J. Dupont-Roc, and G. Grynberg. *Photons and Atoms: Introduction to Quantum Electrodynamics.* Wiley, 1989.

[75] R. J. Glauber. Coherent and incoherent states of the radiation field. *Phys. Rev.*, 131:2766–2788, 1963.

[76] B. R. Mollow. Pure-state analysis of resonant light scattering: Radiative damping, saturation, and multiphoton effects. *Phys. Rev. A*, 12:1919–1943, 1975.

[77] Y. Castin. *Bose-Einstein condensates in atomic gases: simple theoretical results.* Lecture Notes of Les Houches Summer School, edited by R. Kaiser, C. Westbrook, and F. David. Springer-Verlag, Berlin, 2001.

[78] E. Fermi. *Ricerca Sci.*, 7:13, 1936.

[79] N. Ashcroft and N. Mermin. *Solid State Physics.* Saunders College Publishing, 1976.

[80] Gregory H. Wannier. The structure of electronic excitation levels in insulating crystals. *Phys. Rev.*, 52:191–197, 1937.

[81] W. Kohn. Analytic properties of Bloch waves and Wannier functions. *Phys. Rev.*, 115:809–821, 1959.

[82] F. H. L. Essler, H. Frahm, F. Göhmann, A. Klümper, and V. E. Korepin. *The One-Dimensional Hubbard Model.* Cambridge University Press, 2004.

[83] P. Nozières and S. Schmitt-Rink. Bose condensation in an attractive fermion gas: From weak to strong coupling superconductivity. *Journal of Low Temperature Physics*, 59:195–211, 1985.

[84] A. F. Ho, M. A. Cazalilla, and T. Giamarchi. Quantum simulation of the Hubbard model: The attractive route. *Phys. Rev. A*, 79:033620, 2009.

[85] A. Toschi, P. Barone, M. Capone, and C. Castellani. Pairing and superconductivity from weak to strong coupling in the attractive Hubbard model. *New Journal of Physics*, 7(1):7, 2005.

[86] F. Werner, O. Parcollet, A. Georges, and S. R. Hassan. Interaction-induced adiabatic cooling and antiferromagnetism of cold Fermions in optical lattices. *Phys. Rev. Lett.*, 95:056401, 2005.

[87] S. Sachdev. *Quantum Phase Transitions.* Cambridge University Press, 2011.

[88] T. D. Kühner, S. R. White, and H. Monien. One-dimensional bose-Hubbard model with nearest-neighbor interaction. *Phys. Rev. B*, 61:12474–12489, 2000.

[89] D. van Oosten, P. van der Straten, and H. T. C. Stoof. Quantum phases in an optical lattice. *Phys. Rev. A*, 63:053601, 2001.

[90] V. Weisskopf and E. Wigner. Berechnung der natürlichen linienbreite auf grund der diracschen lichttheorie. *Zeitschrift für Physik*, 63(1):54–73, 1930.

[91] J. J. Sakurai. *Advanced Quantum Mechanics.* Pearson Education, 1967.

[92] J. J. Sakurai. *Modern Quantum Mechanics.* Pearson Education, 2006.

[93] C. Gardiner and P. Zoller. *Quantum Noise.* Springer, 2010.

[94] R. H. Lehmberg. Radiation from an N-Atom System. I. General Formalism. *Phys. Rev. A*, 2:883–888, 1970.

[95] J. Dalibard and C. Cohen-Tannoudji. Atomic motion in laser light: connection between semiclassical and quantum descriptions. *Journal of Physics B: Atomic and Molecular Physics*, 18(8):1661, 1985.

[96] F. Verstraete, V. Murg, and J.I. Cirac. Matrix product states, projected entangled pair states, and variational renormalization group methods for quantum spin systems. *Advances in Physics*, 57(2):143–224, 2008.

[97] U. Schollwöck. The density-matrix renormalization group in the age of matrix product states. *Ann. Phys.*, 326(1):96–192, 2011.

[98] M. A. Cazalilla and J. B. Marston. Time-dependent density-matrix renormalization group: A systematic method for the study of quantum many-body out-of-equilibrium systems. *Phys. Rev. Lett.*, 88:256403, 2002.

[99] A. J. Daley, C. Kollath, U. Schollwöck, and G. Vidal. Time-dependent density-matrix renormalization-group using adaptive effective Hilbert spaces. *J. Stat. Mech.*, 2004(04):P04005, 2004.

[100] S. R. White and A. E. Feiguin. Real-time evolution using the density matrix renormalization group. *Phys. Rev. Lett.*, 93:076401, 2004.

[101] S. Östlund and S. Rommer. Thermodynamic limit of density matrix renormalization. *Phys. Rev. Lett.*, 75:3537–3540, 1995.

[102] J. S. Bernier, D. Poletti, and C. Kollath. Density-matrix spectra for integrable models. *Ann. Phys. (Leipzig)*, 8, 1998.

[103] F. Verstraete and J. I. Cirac. Matrix product states represent ground states faithfully. *Phys. Rev. B*, 73:094423, 2006.

[104] J. Eisert, M. Cramer, and M. B. Plenio. Colloquium: Area laws for the entanglement entropy. *Rev. Mod. Phys.*, 82:277–306, 2010.

[105] M. Suzuki. Fractal decomposition of exponential operators with applications to many-body theories and Monte Carlo simulations. *Physics Letters A*, 146(6):319 – 323, 1990.

[106] A. T. Sornborger and E. D. Stewart. Higher-order methods for simulations on quantum computers. *Phys. Rev. A*, 60:1956–1965, 1999.

[107] R. Dum, A. S. Parkins, P. Zoller, and C. W. Gardiner. Monte Carlo simulation of master equations in quantum optics for vacuum, thermal, and squeezed reservoirs. *Phys. Rev. A*, 46:4382–4396, 1992.

[108] A. J. Daley, J. M. Taylor, S. Diehl, M. Baranov, and P. Zoller. Atomic three-body loss as a dynamical three-body interaction. *Phys. Rev. Lett.*, 102:040402, 2009.

[109] P. Calabrese and J. Cardy. Entanglement and correlation functions following a local quench: a conformal field theory approach. *Journal of Statistical Mechanics: Theory and Experiment*, 2007(10):P10004, 2007.

[110] S. Sarkar, S. Langer, J. Schachenmayer, and A. J. Daley. Light scattering and dissipative dynamics of many fermionic atoms in an optical lattice. *Phys. Rev. A*, 90:023618, 2014.

[111] F. Scazza, C. Hofrichter, M. Höfer, P. C. De Groot, I. Bloch, and S. Fölling. Observation of two-orbital spin-exchange interactions with ultracold SU(N)-symmetric fermions. *Nat. Phys.*, 10:779784, 2014.

[112] X. Zhang, M. Bishof, S. L. Bromley, C. V. Kraus, M. S. Safronova, P. Zoller, A. M. Rey, and J. Ye. Spectroscopic observation of SU(N)-symmetric interactions in Sr orbital magnetism. *Science*, 345:1467–1473, 2014.

[113] R. W. Berends and L. Maleki. Hyperfine structure and isotope shifts of transitions in neutral and singly ionized Ytterbium. *J. Opt. Soc. Am. B*, 9 (3):332–338, 1992.

[114] I. Reichenbach and I. H. Deutsch. Sideband cooling while preserving coherences in the nuclear spin state in group-II-like atoms. *Phys. Rev. Lett.*, 99: 123001, 2007.

[115] C. Cohen-Tannoudji, J. Dupont-Roc, and G. Grynberg. *Atom-photon interactions: basic processes and applications*. Wiley-Interscience publication. J. Wiley, 1992.

[116] K. G. Libbrecht, R. A. Boyd, P. A. Willems, T. L. Gustavson, and D. K. Kim. Teaching physics with 670 nm diode lasers—construction of stabilized lasers and Lithium cells. *American Journal of Physics*, 63(8):729–737, 1995.

[117] M. Lewenstein, A. Sanpera, V. Ahufinger, B. Damski, A. Sen(De), and U. Sen. Ultracold atomic gases in optical lattices: mimicking condensed matter physics and beyond. *Advances in Physics*, 56(2):243–379, 2007.

[118] M.A. Cazalilla and A. M. Rey. Ultracold Fermi gases with emergent SU(N) symmetry. *Reports on Progress in Physics*, 77(12):124401, 2014.

[119] A. V. Gorshkov, M. Hermele, V. Gurarie, C. Xu, P. S. Julienne, J. Ye, P. Zoller, E. Demler, M. D. Lukin, and A. M. Rey. Two-orbital SU(N)

magnetism with ultracold alkaline-earth atoms. *Nat. Phys.*, 6(4):289–295, 2010.

[120] J. Dalibard. Collisional dynamics of ultra-cold atomic gases. *Bose-Einstein Condensation in Atomic Gases, edited by M. Inguscio, S. Stringari, and C. Wieman*, 1998.

[121] P. O. Fedichev, Yu. Kagan, G. V. Shlyapnikov, and J. T. M. Walraven. Influence of nearly resonant light on the scattering length in low-temperature atomic gases. *Phys. Rev. Lett.*, 77:2913–2916, 1996.

[122] R. H. Lehmberg. Radiation from an N-Atom System. II. Spontaneous Emission from a Pair of Atoms. *Phys. Rev. A*, 2:889–896, 1970.

[123] M. Greiner, C. A. Regal, and D. S. Jin. Emergence of a molecular Bose–Einstein condensate from a Fermi gas. *Nature (London)*, 426(6966):537–540, 2003.

[124] D. S. Petrov, C. Salomon, and G. V. Shlyapnikov. Weakly bound dimers of fermionic atoms. *Phys. Rev. Lett.*, 93:090404, 2004.

[125] Y. Takasu, K. Maki, K. Komori, T. Takano, K. Honda, M. Kumakura, T. Yabuzaki, and Y. Takahashi. Spin-singlet Bose-Einstein condensation of two-electron atoms. *Phys. Rev. Lett.*, 91:040404, 2003.

[126] D. Poletti, P. Barmettler, A. Georges, and C. Kollath. Emergence of glasslike dynamics for dissipative and strongly interacting bosons. *Phys. Rev. Lett.*, 111:195301, 2013.

[127] R. H. Dicke. Coherence in spontaneous radiation processes. *Phys. Rev.*, 93: 99–110, 1954.

[128] M. Gross and S. Haroche. Superradiance: An essay on the theory of collective spontaneous emission. *Physics Reports*, 93(5):301 – 396, 1982.

[129] A. Kolezhuk and H. Mikeska. *Lect. Not. Phys.*, 645:1, 2004.

[130] F. Meinert, M. J. Mark, E. Kirilov, K. Lauber, P. Weinmann, A. J. Daley, and H. C. Nägerl. Quantum Quench in an Atomic One-Dimensional Ising Chain. *Phys. Rev. Lett.*, 111:053003, 2013.

[131] J. Meineke, J. Brantut, D. Stadler, T. Muller, H. Moritz, and T. Esslinger. Interferometric measurement of local spin fluctuations in a quantum gas. *Nat. Phys.*, 8(6):454–458, 2012.

[132] C. L. Cleveland and R. A. Medina. Obtaining a Heisenberg Hamiltonian from the Hubbard model. *American Journal of Physics*, 44(1):44–46, 1976.

[133] L. D. Landau and E. M. Lifshitz. *Quantum Mechanics: Non-relativistic Theory.* Butterworth-Heinemann, 1977.

[134] R. B. Sidje. Expokit: A software package for computing matrix exponentials. *ACM Trans. Math. Softw.*, 24(1):130–156, 1998.

[135] D. Poletti, J. Bernier, A. Georges, and C. Kollath. Interaction-induced impeding of decoherence and anomalous diffusion. *Phys. Rev. Lett.*, 109: 045302, 2012.

[136] J. P. Ronzheimer, M. Schreiber, S. Braun, S. S. Hodgman, S. Langer, I. P. McCulloch, F. Heidrich-Meisner, I. Bloch, and U. Schneider. Expansion dynamics of interacting bosons in homogeneous lattices in one and two dimensions. *Phys. Rev. Lett.*, 110:205301, 2013.

[137] C. Weitenberg, M. Endres, J. F. Sherson, M. Cheneau, P. Schauß, T. Fukuhara, I. Bloch, and S. Kuhr. Single-spin addressing in an atomic Mott insulator. *Nature (London)*, 471(7338):319–324, 2011.

[138] D. Petrosyan, B. Schmidt, J. R. Anglin, and M. Fleischhauer. Quantum liquid of repulsively bound pairs of particles in a lattice. *Phys. Rev. A*, 76: 033606, 2007.

[139] H. P. Lüschen, P. Bordia, S. S. Hodgman, M. Schreiber, S. Sarkar, A. J. Daley, M. H. Fischer, E. Altman, I. Bloch, and U. Schneider. Signatures of many-body localization in a controlled open quantum system. *Phys. Rev. X*, 7:011034, 2017.

[140] D.M. Basko, I. L. Aleiner, and B. L. Altschuler. Metal-insulator transition in a weakly interacting many-electron system with localized single-particle states. *Ann. Phys.*, 321(1126), 2006.

[141] I. V. Gornyi, A. D. Mirlin, and D. G. Polyakov. Interacting Electrons in Disordered Wires: Anderson Localization and Low-T Transport. *Phys. Rev. Lett.*, 95:206603, 2005.

[142] J. Z. Imbrie. On many-body localization for quantum spin chains. *Journal of Statistical Physics*, 163(5):998–1048, 2016.

[143] V. Oganesyan and D. A. Huse. Localization of interacting fermions at high temperature. *Phys. Rev. B*, 75:155111, 2007.

[144] A. Pal and D. A. Huse. Many-body localization phase transition. *Phys. Rev. B*, 82:174411, 2010.

[145] R. Vosk and E. Altman. Many-body localization in one dimension as a dynamical renormalization group fixed point. *Phys. Rev. Lett.*, 110:067204, 2013.

[146] V. P. Michal, I. L. Aleiner, B. L. Altshuler, and G. V. Shlyapnikov. Finite-temperature fluidinsulator transition of strongly interacting 1D disordered bosons. *Proceedings of the National Academy of Sciences*, 113(31):E4455–E4459, 2016.

[147] R. Nandkishore and D. A. Huse. Many-body localization and thermalization in quantum statistical mechanics. *Annual Review of Condensed Matter Physics*, 6:15–38, 2015.

[148] E. Altman and R. Vosk. Universal dynamics and renormalization in many-body-localized systems. *Annual Review of Condensed Matter Physics*, 6(1): 383–409, 2015.

[149] M. Ovadia, D. Kalok, I. Tamir, S. Mitra, B. Sacp, and D. Shahar. Evidence for a finite-temperature insulator. *Scientific Reports*, 5(13503), 2015.

[150] P. Bordia, H. P. Lüschen, S. S. Hodgman, M. Schreiber, I. Bloch, and U. Schneider. Coupling identical one-dimensional many-body localized systems. *Phys. Rev. Lett.*, 116:140401, 2016.

[151] J. Smith, A. Lee, P. Richerme, B. Neyenhuis, P. W. Hess, P. Hauke, M. Heyl, A. A. Huse, and C. Monroe. Many-body localization in a quantum simulator with programmable random disorder. *Nat. Phys.*, 12:907911, 2016.

[152] J. M. Deutsch. Quantum statistical mechanics in a closed system. *Phys. Rev. A*, 43:2046–2049, 1991.

[153] M. Srednicki. Chaos and quantum thermalization. *Phys. Rev. E*, 50:888–901, 1994.

[154] M. Rigol, V. Dunjko, and M. Olshanii. Thermalization and its mechanism for generic isolated quantum systems. *Nature*, 452:854–858, 2008.

[155] P. W. Anderson. Absence of diffusion in certain random lattices. *Phys. Rev.*, 109:1492–1505, 1958.

[156] S. Iyer, V. Oganesyan, G. Refael, and D. A. Huse. Many-body localization in a quasiperiodic system. *Phys. Rev. B*, 87:134202, 2013.

[157] D. S. Wiersma, P. Bartolini, and R. Righini. Localization of light in a disordered medium. *Nature*, 390:671–673, 1997.

[158] Y. Lahini, A. Avidan, F. Pozzi, M. Sorel, R. Morandotti, D. N. Christodoulides, and Y. Silberberg. Anderson localization and nonlinearity in one-dimensional disordered photonic lattices. *Phys. Rev. Lett.*, 100: 013906, 2008.

[159] T. Schwartz, G. Bartal, S. Fishman, and M. Segev. Transport and Anderson localization in disordered two-dimensional photonic lattices. *Nature*, 446: 52–55, 2007.

[160] J. Billy, V. Josse, Z. Zuo, A. Bernard, B. Hambrecht, P. Lugan, D. Clement, L. Sanchez-Palencia, P. Bouyer, P. Bouyer, and A. Aspect. Direct observation of Anderson localization of matter waves in a controlled disorder. *Nature*, 453:891–894, 2008.

[161] S. S. Kondov, W. R. McGehee, W. Xu, and B. DeMarco. Disorder-induced localization in a strongly correlated atomic Hubbard gas. *Phys. Rev. Lett.*, 114:083002, 2015.

[162] F. Jendrzejewski, A. Bernard, P. Cheinet, V. Josse, M. Piraud, L. Pezze, L. Sanchez-Palencia, A. Aspect, and P. Bouyer. Three-dimensional localization of ultracold atoms in an optical disordered potential. *Nat. Phys.*, 8: 398–403, 2012.

[163] G. Roati, C. DErrico, L. Fallani, M. Fattori, C. Fort, M. Zaccanti, G. Modugno, M. Modugno, and M. Inguscio. Anderson localization of a non-interacting Bose-Einstein condensate. *Nature*, 453:895–898, 2008.

[164] S. Aubry and G. André. Analyticity breaking and Anderson localization in incommensurate lattices. *Ann. Israel Phys. Soc.*, 3(133), 1980.

[165] M. Albert and P. Leboeuf. Localization by bichromatic potentials versus Anderson localization. *Phys. Rev. A*, 81:013614, 2010.

[166] U. Schneider, L. Hackermüller, S. Will, T. Best, I. Bloch, T. A. Costi, R. W. Helmes, D. Rasch, and A. Rosch. Metallic and insulating phases of repulsively interacting fermions in a 3D optical lattice. *Science*, 322(5907): 1520–1525, 2008.

[167] L. Leblanc. *Exploring many-body physics with ultracold atoms.* University of Toronto, 2011.

[168] E. Levi, M. Heyl, I. Lesanovsky, and J. P. Garrahan. Robustness of many-body localization in the presence of dissipation. *Phys. Rev. Lett.*, 116: 237203, 2016.

[169] M. H Fischer, M. Maksymenko, and E. Altman. Dynamics of a many-body-localized system coupled to a bath. *Phys. Rev. Lett.*, 116:160401, 2016.

[170] J. Kondo. Resistance minimum in dilute magnetic alloys. *Progress of Theoretical Physics*, 32(1):37–49, 1964.

[171] P. A. Lee, N. Nagaosa, and X. Wen. Doping a Mott insulator: Physics of high-temperature superconductivity. *Rev. Mod. Phys.*, 78:17–85, 2006.

[172] A. S. Alexandrov and N. F. Mott. Bipolarons. *Reports on Progress in Physics*, 57(12):1197, 1994.

[173] A. S. Alexandrov, J. Ranninger, and S. Robaszkiewicz. Bipolaronic superconductivity: Thermodynamics, magnetic properties, and possibility of existence in real substances. *Phys. Rev. B*, 33:4526–4542, 1986.

[174] S. Palzer, C. Zipkes, C. Sias, and M. Köhl. Quantum transport through a Tonks-Girardeau gas. *Phys. Rev. Lett.*, 103:150601, 2009.

[175] J. Reeves, L. Krinner, M. Stewart, A. Pazmiño, and D. Schneble. Nonadiabatic diffraction of matter waves. *Phys. Rev. A*, 92:023628, 2015.

[176] B. Gadway, D. Pertot, R. Reimann, and D. Schneble. Superfluidity of interacting bosonic mixtures in optical lattices. *Phys. Rev. Lett.*, 105:045303, 2010.

[177] M. Wouters and G. Orso. Two-body problem in periodic potentials. *Phys. Rev. A*, 73:012707, 2006.

[178] D. S. Rokhsar and B. G. Kotliar. Gutzwiller projection for bosons. *Phys. Rev. B*, 44:10328–10332, 1991.

[179] P. Muruganandam and S. K. Adhikari. Fortran programs for the time-dependent GrossPitaevskii equation in a fully anisotropic trap. *Computer Physics Communications*, 180(10):1888 – 1912, 2009.